

University of Windsor

Scholarship at UWindor

Electronic Theses and Dissertations

Theses, Dissertations, and Major Papers

9-24-2019

Heart Rate Estimation During Physical Exercise Using Wrist-Type Ppg Sensors

Thiago Toledo Souza
University of Windsor

Follow this and additional works at: <https://scholar.uwindsor.ca/etd>

Recommended Citation

Souza, Thiago Toledo, "Heart Rate Estimation During Physical Exercise Using Wrist-Type Ppg Sensors" (2019). *Electronic Theses and Dissertations*. 7840.
<https://scholar.uwindsor.ca/etd/7840>

This online database contains the full-text of PhD dissertations and Masters' theses of University of Windsor students from 1954 forward. These documents are made available for personal study and research purposes only, in accordance with the Canadian Copyright Act and the Creative Commons license—CC BY-NC-ND (Attribution, Non-Commercial, No Derivative Works). Under this license, works must always be attributed to the copyright holder (original author), cannot be used for any commercial purposes, and may not be altered. Any other use would require the permission of the copyright holder. Students may inquire about withdrawing their dissertation and/or thesis from this database. For additional inquiries, please contact the repository administrator via email (scholarship@uwindsor.ca) or by telephone at 519-253-3000ext. 3208.

HEART RATE ESTIMATION DURING PHYSICAL EXERCISE USING WRIST-TYPE PPG SENSORS

by

Thiago Toledo Souza

A Thesis

Submitted to the Faculty of Graduate Studies
through the Department of Electrical and Computer Engineering
in Partial Fulfilment of the Requirements for
the Degree of Master of Applied Science at the
University of Windsor

Windsor, Ontario, Canada

© 2019 Thiago Toledo Souza

HEART RATE ESTIMATION DURING PHYSICAL EXERCISE USING WRIST-TYPE PPG SENSORS

by
Thiago Toledo Souza

APPROVED BY:

W. Kedzierski
Department of Physics

Sazzadur Chowdhury
Department of Electrical and Computer Engineering

R. Maev, Advisor
Department of Physics

B. Balasingam, Co - Advisor
Department of Electrical and Computer Engineering

September 24, 2019

Declaration of Co-Authorship / Previous Publication

Co-Authorship

I hereby declare that this thesis incorporates material that is result of joint research, as follows: Chapter 3 of this thesis was co-authored with professor Balasingam and professor Roman Maev, who provided supervision and guidance during the research and writing process. In all cases, the key ideas, primary contributions, experimental designs, data analysis, interpretation, and writing were performed by the author.

I am aware of the University of Windsor Senate Policy on Authorship and I certify that I have properly acknowledged the contribution of other researchers to my thesis, and have obtained written permission from each of the co-author(s) to include the above material(s) in my thesis.

Previous Publication

Thesis chapter	Publication title/full citation	Publication status
3	T. Souza, B. Balasingam and R. Maev, “Autonomous Heart Rate Tracking Methodology Using Kalman Filter and the EM Algorithm” International Conference on Information Fusion, Ottawa, Canada, July 2019.	In press

I certify that I have obtained a written permission from the copyright owner(s) to include the above published material(s) in my thesis. I certify that the above material describes work completed during my registration as a graduate student at the University of Windsor.

General

I declare that, to the best of my knowledge, my thesis does not infringe upon anyone's copyright nor violate any proprietary rights and that any ideas, techniques, quotations, or any other material from the work of other people included in my thesis, published or otherwise, are fully acknowledged in accordance with the standard referencing practices. Furthermore, to the extent that I have included copyrighted material that surpasses the bounds of fair dealing within the meaning of the Canada Copyright Act, I certify that I have obtained a written permission from the copyright owner(s) to include such material(s) in my thesis. I declare that this is a true copy of my thesis, including any final revisions, as approved by my thesis committee and the Graduate Studies office, and that this thesis has not been submitted for a higher degree to any other University or Institution.

Abstract

Accurate heart rate monitoring during intense physical exercise is a challenging problem due to the high levels of motion artifacts (MA) in photoplethysmography (PPG) sensors. PPG is a non-invasive optical sensor that is being used in wearable devices to measure blood flow changes using the property of light reflection and absorption, allowing the extraction of vital signals such as the heart rate (HR). However, the sensor is susceptible to MA which increases during physical activity. This occurs since the frequency range of movement and HR overlaps, difficulting correct HR estimation. For this reason, MA removal has remained an active topic under research. Several approaches have been developed in the recent past and among these, a Kalman filter (KF) based approach showed promising results for an accurate estimation and tracking using PPG sensors. However, this previous tracker was demonstrated for a particular dataset, with manually tuned parameters. Moreover, such trackers do not account for the correct method for fusing data. Such a custom approach might not perform accurately in practical scenarios, where the amount of MA and the heart rate variability (HRV) depend on numerous, unpredictable factors. Thus, an approach to automatically tune the KF based on the Expectation-Maximization (EM) algorithm, with a measurement fusion approach is developed. The applicability of such a method is demonstrated using an open-source PPG database, as well as a developed synthetic generation tool that models PPG and accelerometer (ACC) signals during pre-determined physical activities.

Acknowledgements

I would first like to gratefully acknowledge my wife Julianne who provided me through moral, sacrifice, and emotional support. I can't thank you enough for encouraging me through this experience. Also, I am deeply grateful for my parents Aldo and Loide, my sister and my in-laws for their ongoing support in my academic involvement and daily prayers to ensure my success in life. I would like to express thanks to members of the Federal Technological University of Parana in Brazil and the University of Windsor for their guidance and assistance throughout my undergraduate and graduate studies. I owe an enormous debt of gratitude to previous and current members of Tessonics and the Institute for Diagnostic Imaging Research who have overseen my growth with special gratitude to my principal advisor Dr. Roman Maev who believed in me and provided me with such an amazing opportunity to study and work with amazing professionals, Dmitry Gavrilov, for valuable insights and Sarah Beneteau who helped me in some many situations as an international student. I would also like to thank my co-advisor Dr. Balasingam for his valuable guidance and expertise. Also, to all of those who journeyed with me to complete my academic goals and provided me with the tools and wisdom to reach my full potential, thank you. I wish you all the best. Lastly, but most importantly, I dedicate this thesis to God, who has given me strength, focus, and determination to complete one more step in my professional and educational life.

Contents

Declaration of Co-Authorship / Previous Publication	iii
Abstract	vi
Acknowledgements	vii
Nomenclature	xii
List of Tables	xiv
List of Figures	xv
1 Introduction	1
1.1 Literature Search and Motivation	1
1.2 Organization of the Thesis	4
1.3 Problem Statement	6
2 Background to the Study	8
2.1 Wearable Sensor and Systems	8
2.2 Photoplethysmography	9
2.2.1 Brief History	9

2.2.2	Functionality	10
2.3	Motion Artifacts	14
2.4	Tissue Optical Characteristics	16
2.5	Sensor Location	19
2.6	Perfusion	20
2.7	Crossover Problem	21
2.8	Advantages	22
2.9	Challenges	23
2.10	Existing Research	24
3	Methodology	26
3.1	HR Estimation Methods	27
3.1.1	Dataset	27
3.1.2	Comparison Between Methods	29
3.2	Proposed Algorithm	31
3.2.1	Framework	32
3.2.2	Processing of input signals	32
3.2.3	De-noising and MA reference	33
3.2.4	Post processing and HR estimation	37
3.3	Problem Definition	39
3.4	Review of the EM Algorithm	40
3.4.1	The EM Algorithm	40
3.4.2	HR Process Model Estimation Using the EM Algorithm	42
3.4.3	Complete-Data Likelihood of Θ	43
3.4.4	Expectation	44
3.4.5	Maximization	44

3.5	Results	45
3.5.1	Computer Simulation Results	46
3.5.2	Real Data Results	46
3.6	Conclusions and Discussions	50
4	Fusion Method	56
4.1	State Vector Fusion	58
4.2	Measurement Fusion	59
4.3	Performance Analysis	60
4.4	Final Proposed Algorithm	61
5	Synthetic signals	64
5.1	Physical Activity model (PAM)	65
5.1.1	Heart Rate Pattern	67
5.2	Synthetic Signal Simulation	69
5.2.1	Synthetic PPG	70
5.2.2	Synthetic tri-axil accelerometer	71
5.2.3	EM Approach	75
5.3	PAM Evaluation	76
5.3.1	Linear Model	76
5.3.2	Exponential Model	78
5.4	Results and Discussions	79
6	Hardware Implementation	84
6.1	Hardware development	85
6.2	Algorithm Implementation	88

7	Summary, Conclusions and Future Work	93
7.1	Summary and Conclusions	93
7.1.1	Concluding Remarks	95
7.2	Future work	96
Appendix A	Table of Methods	98
Bibliography		100
Vita Auctoris		112

Nomenclature

AC Alternating Current

ACC Accelerometer

AF Atrial Fibrillation

BP Blood Pressure

BPM Beats Per Minute

CVD Cardio Vascular Disease

DC Direct Current

DFT Discrete Fourier Transform

DSP Digital Signal Processing

ECG ElectroCardioGram

EEG ElectroEncephaloGram

EM Expectation Maximization

EMG ElectroMyoGram

ENG ElectroNeuroGram

EOG ElectroOculoGram

FFT Fast Fourier Transform

GT Ground Truth

GYRO Gyroscope

HR Heart Rate

HRP Heart Rate Pattern

HRV Heart Rate Variability

HW HardWare

HWSM Harmonic Window Selection Method

KF Kalman filter

LED Light Emitting Diode

MA Motion Artifacts

PAM Physical Activity Model

PPG PhotoPlethysmoGraphy

RFID Radio Frequency IDentification

SpO2 Arterial O_2 Saturation

SVD Singular Value Decomposition

VM Vector Magnitude

List of Tables

2.1	Classification of biosignal according to associated form of energy	9
2.2	Features of PPG signal	11
2.3	Wider spacing between source-detector captures less total light, but has a higher ratio to blood-flow scatter compared to motion-related scatter.	24
3.4	Database of 23 PPG recordings from IEEE SP CUP [1]	28
3.5	Activity level performed for dataset in [1].	29
5.6	Assumptions for each activity level	67
5.7	Metrics comparison for different HR estimation methods with a linear PAM model. B = EM Batch, T = EM Trigger, PA = Proposed Algorithm.	78
5.8	Metrics comparison for different HR estimation methods with an exponential PAM model. B = EM Batch, T = EM Trigger, PA = Proposed Algorithm.	79

List of Figures

1.1	Published research under the photoplethysmography topic.	5
2.2	Typical waveform of the PPG: (a) AC component (red curve) represents the light absorption by pulsative blood volume, DC(black curve) is a slowly varying component. (b) ratio AC/DC after detrending and inversion. ECG is recorded simultaneously and appears in blue color.	12
2.3	The absorption spectrum for oxygenated and deoxygenated hemoglobin is different, allowing the sensor to estimate heart rate and blood oxygenation information of the localized tissue.	13
2.4	(a) A segment of the ECG (ground truth) and (b) corresponding PPG in time domain. (c) Periodogram representation for both cases and spurious MA peaks near the HR peak.	15
2.5	(a) A segment of the ECG (ground truth) and (b) corresponding PPG in time domain. (c) Periodogram representation for both cases and no peak detection of HR.	16
2.6	(a) A segment of the ECG (ground truth) and (b) corresponding PPG in time domain. (c) Periodogram representation for both cases and MA peak and HR peak are almost imperceptible from each other.	17

2.7	Schematic diagram of optical pathways in skin. Keratinized squamous cells (1) and large melanin aggregates (2) are responsible for absorption and scattering. The vascularized dermis (3) includes absorbers such as oxygenated and deoxygenated hemoglobin, caroten and bilirubin.	18
2.8	Comparing Heart Rate Monitoring devices (HRM), it is apparent that Apple Watch exhibits heart rate monitoring failure during “cross-overs”, where the person’ step rate and heart rate were so similar that the algorithm could not sufficiently differentiate between them; #2 this crossover event caused a faulty HR reading for more than 2 minutes, where the true HR was mistakenly report as the step rate (cadence).	21
3.9	Flowchart of 3 main stages for HR estimation.	26
3.10	Flowchart of HR estimation system. Proposed algorithm belongs to the final block (KF & EM)	32
3.11	Spectrum comparison of raw PPG signal, ACC and denoised PPG signal, after denoising stage with SVD method.	36
3.12	Detailed Kalman Filter diagram from [2].	39
3.13	Proposed approach with KF from [2] and EM.	45
3.14	Comparison of KF and the EM algorithm for state model in (3.11) with $N = 10$ iterations.	47
3.15	Comparison between estimated HR values of [2] with $\sigma_v = 4$ and $\sigma_w = 10$ and the EM algorithm – Dataset #4	48
3.16	Bland Altman plot in [2]	51
3.17	Bland Altman plot of the EM algorithm with $\sigma_v = 4$ and $\sigma_w = 10$	51
3.18	Comparison between estimated HR values of [2] with $\sigma_v = 1$ and $\sigma_w = 10$ and the EM algorithm – Dataset #4	52

3.19	Bland Altman plot in [2]	53
3.20	Bland Altman plot of the EM algorithm with $\sigma_v = 1$ and $\sigma_w = 10$	53
3.21	Comparison between estimated HR values of [2] with $\sigma_v = 1$ and $\sigma_w = 1$ and the EM algorithm – Dataset #4	54
3.22	Bland Altman plot in [2]	55
3.23	Bland Altman plot of the EM algorithm with $\sigma_v = 1$ and $\sigma_w = 1$	55
4.24	Ratio of components of covariance matrix for two sensor fused estimate and algorithm proposed in [2].	62
4.25	Flowchart of final HR estimation system.	63
4.26	Final Algorithm proposed for HR estimation.	63
5.27	Illustration of <i>PAM</i> for various running activities level and time durations.	66
5.28	Illustration of HR pattern for various running activities level and time dura- tions. For this particular case the pattern was obtained from example model as in (5.51).	69
5.29	Synthesized PPG signal for different physical activities.	71
5.30	Illustration of ACC pattern for various running activities level and time dura- tions. For this particular case the pattern was obtained from example model as in (5.51).	73
5.31	Synthesized ACC signal for different physical activities. X, Y and Z corre- sponds to signal of each individual axis and VM is the vector magnitude.	74
5.32	Synthesized PPG signal for different physical activities related to the move- ment that is being performed. There is a spectrum overlap of clean PPG signal as in Figure 5.29 and ACC signal in Figure 5.31, which difficulties the correct estimation of HR using PPG sensors.	75

5.33	EM algorithm estimates the noise variances over the period of estimation. Switching point represents the acknowledgement that a activity changed, and the EM is calculated after the movement related to the activity is decreased.	80
5.34	Illustration of <i>PAM</i> for various running activities level and time durations following the example model in (5.57).	81
5.35	Illustration of <i>PAM</i> for various running activities level and time durations following the example model in (5.60).	82
5.36	Comparison between known algorithms for HR estimation using PPG sensors with a linear PAM model.	83
5.37	Comparison between known algorithms for HR estimation using PPG sensors with a exponential PAM model.	83
6.38	Architectural layer of an ideal wearable system.	85
6.39	Hardware diagram implementation	87
6.40	Detailed client and server.	88
6.41	Hardware implemented.	88
6.42	Peak selection taking in account the difference (D) and addition (A) of the spectrum estimation. The estimated peak from (D) produces a peak that is very close to the GT value – Dataset #6.	90
6.43	Comparison between finding the highest peak in the spectrum and the pro- posed algorithm. Under intense physical activity, the algorithm still follows the GT HR value – Dataset #12.	91
6.44	PPG signal acquired on the wrist.	92
6.45	HWSM implemented in HW.	92

Chapter 1

Introduction

1.1 Literature Search and Motivation

Heart rate information is one of the most important vital signs that can be gathered from a person, along with blood pressure, temperature and respiration. It also provides intrinsic information about the state of the cardiovascular system, which resembles the quality and health of an individual's life. Moreover, it represents a useful indicator of physiological adaptation and intensity of effort [3]. For this reason, heart rate monitoring is important since it translates the process of oxygen circulation and other nutrients to the body. Thus, if the heart is not functioning properly, it will affect all other systems. This represents a direct relation with the stroke volume and the cardiac measurement at each beat.

Heart rate (HR) is defined as the number of heart pulses in a period of time, and it's usually presented in beats per minute (BPM). This corresponds to one's cardiovascular fitness or how the heart adapts to unpredictable stimuli. Usually HR is used as an indicator of sympathetic and parasympathetic nervous system activity in response to physiological

conditions [4]. So, it is necessary to track its pattern in order to determine possible arrhythmias (abnormalities), since this might indicate a heart defect or a serious heart condition that requires immediate intervention. According to a study conducted by the World Health Organization in 2017, cardiovascular diseases (CVDs) are the number one cause of death globally and almost 18 million people died from CVDs in 2016, which accounts for 31% of all global deaths [5]. These numbers represent the importance of monitoring one's cardiovascular system and why researchers keep going further to find better, faster and more reliable solutions to estimate heart rate information, whether in hospitals or more recently, in wearable devices. There have been several methods presented over the years to measure and track heart rate information. Not until the 19th century, in modern Europe, that research started to take place in order to find how the heart performs its task and how the electrical activity spreads throughout the heartbeat cycle. The movement initiated with the original electrocardiograph composed by a string galvanometer, which recorded the potential difference between extremities resulting from the heart's electrical activation [6]. Then, in the first half of the 20th century, several innovations set in motion the whole movement and fascinating sequence of discoveries that led to the well known 12 lead electrocardiogram (ECG) as we know. For many years, ECG was established as the dominant cardiac monitoring technique to identify cardiovascular problems and detect irregularities in heart rhythms [6]. Even though traditional cardiac monitoring through ECG has developed exponentially over the years, in order to commit to continuous requirements of their users, notably, accuracy, and user comfort, these techniques, up until now, have not provided user flexibility, portability, and convenience [7]. In each step of this unending development, physicians involved the ECG as being an essential clinical instrument, even though it had recognized deficiencies. This concept pushed researchers to improve the technology allowing for optimization and improvements for better, faster and affordable non-invasive instruments.

As mentioned before, ECG was the first and most accepted method throughout the entire medical community. However, other methods such as radial pulse, applanation tonometry, and cardio-phonography are also used for HR monitoring, but they all have in common limitations such as the restricting movement of the user, capacity to be worn just in a few periods of time, wiring and price. Usually, these instruments need several attachments and connections in order to accurately provide heart rate information from someone's health, which also refrains the movement and comfort of the user. Since this intermittent measurement usually is the common method, it provides only a periodic overview of the cardiovascular system's state, which cannot be considered truly accurate. More importantly, maintenance and high cost are drawbacks of these methods, since usually, each method demands assistance and space to be able to be used correctly.

Due to all of those facts, photoplethysmography (PPG) seemed to be an alternative, providing low cost through a simple optical-based technique for monitoring blood flow. PPG comprises then, a novel technique to estimate heart rate. It's an optical and non-invasive method used to detect volume changes in blood vessels [8]. It measures HR based on the changes in light absorption in the tissue in a specific color spectrum range, usually red/green and infra-red wavelength. Light travels through biological tissues and is absorbed with different amplitudes by different substances, including pigments in the skin, blood vessels, muscles, and bones. However, most changes in blood flow occur mainly in the arteries and arterioles. Consequently, arteries that contain more blood during the systolic phase (ventricles contract) than the diastolic phase (ventricles relax) provide better heart rate flow, which in theory produces better signal acquisition from the PPG sensors. They optically detect the change in the blood flow volume between these movements, in the microvascular tissue which appears after filtering, in HR information. This method provides a fast, reliable and cost-effective solution if compared to the usual method of ECG.

Thus, PPG became popular in the past years representing a non-invasive, cost-effective, and lightweight method for HR estimation. Researchers have been studying and implementing better algorithms in order to retrieve reliable information with PPGs, although motion artifacts (MA) , scattering of light and some other drawbacks are presented as common difficulties to be solved.

It is very difficult to obtain the PPG signal without motion artifact, which can be caused by several reasons, such as movement, the gap between the sensor and the skin, environmental noise and reflection/backscattering of the light [9]. Thus, this new method opened a broad field for research and market acquisition. Major companies in the industry of wearable devices have been investing in this sector, and significant research has been done in order to provide better filtering of these MA, smarter and more accurate devices and of course, commercialization.

1.2 Organization of the Thesis

Photoplethysmography became a very popular topic among the scientific and medical communities in the past years, and several fitness/health companies have been investing in this area. According to an international research firm, smartwatches and fitness trackers will be one of the most invested and bright spots over the next years, jumping to almost 200 million units shipped in 2022 [10]. Also, as it can be seen in Figure 1.1, the number of publications regarding PPG for heart rate estimation also increased over time. This also enforces that several methods and algorithms have been implemented for PPGs sensors.

As mentioned before, PPGs are influenced negatively primarily by MA and extensive research has been developed in this area. Reduction of MA is very difficult because their

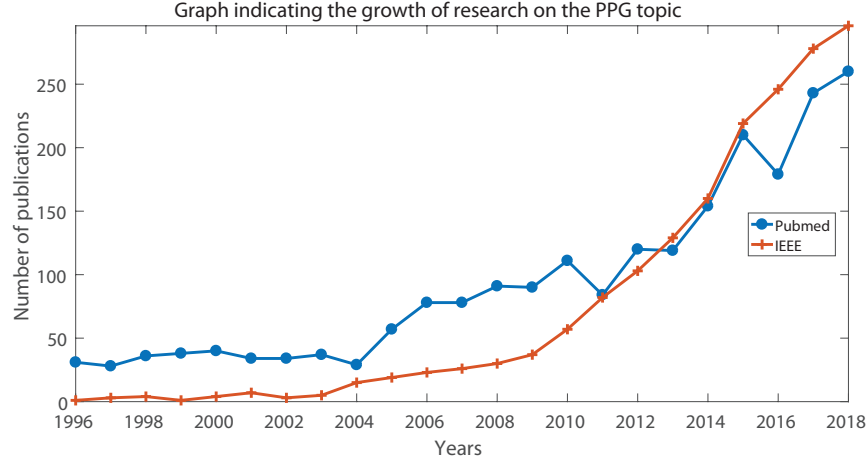


Figure 1.1: Published research under the photoplethysmography topic.

Source: [10] and [11].

major frequency components overlap with the reliable frequency (HR) from the sensor. Several methods have been developed from filtering techniques to machine learning, but usually, they lack a system capable of estimating the state for each heartbeat and fall behind when compared to more robust but also complex algorithms. Since common filtering methods have a fixed frequency range, researchers in the last decade, have proposed two methods to reduce MA from PPG signals. First, is a non-motion reference method, which extracts information from the distorted signal based on the idea that the pulse signal is a major component in the measurement signal, in addition, that the frequency (HR) slowly changes if compared with MA [12–17]. The second category is a motion reference method that uses a reference to body sensors. [18, 19]. It utilizes active noise cancellation requiring a filter optimization algorithm. Laguerre, Least mean Square (LS), Recursive Least mean Square (RLS), Principal Component Analysis (PCA) are a few of the methods proposed, usually the cancellation is made for simple motions, such as vertical and horizontal movements, for finger or forehead sensor acquisition. The first method is not suitable for wearable devices

since it's time-consuming and requires a significantly large amount of data, in order to extract the features of the signal. The second, since it's based on the fact of slow movements, it's unsuitable for daily usage, which requires more complex algorithms to decrease MA for more complex motions, such as running and cycling, for example.

Thus, there is a need to combine complex yet feasible algorithms for wearable devices to accurately estimate HR measurements during physical exercise. This thesis focuses on this statement and is divided into six chapters. The first Chapter introduces the overall composition of the project and the motivation behind the development of the HR estimation method. Chapter 2 focuses on the background study of photoplethysmography sensors and their use, advantages, and challenges with HR estimation. Next, Chapter 3 presents several methods for HR estimation using PPG sensors, as well as the proposed method algorithm and its framework. Chapter 4 explores the different fusing methods available and analyzes the best method for fusing several sensors for a reliable HR estimation. As a result, Chapter 5 provides a synthetic data simulation tool for evaluation of available HR estimation methods, allowing a faster evaluation and generation of signals during physical exercise for wearable devices. Chapter 6 explores the design requirements and processes of the hardware implementation. Lastly, Chapter 7 summarizes the conclusion and future scope of the project.

1.3 Problem Statement

Heart rate estimation becomes a very complex task while in movement, since spectrum of the desired signal (PPG) may overlap with the spectrum related to the movement. This costs in accuracy in wearable devices. Moreover, parameters related to the user physiology are usually not accounted for, which causes algorithms to be tuned for specific datasets

instead of allowing HR estimation of patients that have other more complex cardiovascular problems, such as Atrial Fibrillation (AF) and Blood Pressure (BP) for example. This thesis focuses on an optimal algorithm to reduce MA from PPGs sensors during physical exercise also accounting for user parameters that interfere with a correct HR estimation. In addition, a synthetic PPG signal generation tool is formulated which allows comparison of published HR algorithms to be evaluated independently of exercise duration.

Chapter 2

Background to the Study

The field of electronics have been by far, investing the most to the field of medicine. New medical devices are constantly developed and better techniques are discovered with this outgoing investment. This, in turn, reflects on advances in clinical and self-monitoring systems, providing accurate and reliable methods for living a healthier life. These devices are based on the available medical knowledge combined with technologies available in the electronics field [20]. This increasing demand is driving production and integration for portable devices, stimulating the creation of more reliable, faster, affordable and smaller technologies and methods.

2.1 Wearable Sensor and Systems

Wearable health monitoring technologies have attracted considerable consumer interest over the past years, representing a new emerging field to health monitoring, from hospitals and clinical facilities to fitness/tracking applications. They could be described as an unobtrusive, autonomous, and ubiquitous system that supports continuous, multiparameter monitoring and treatment, and telemetric abilities [21,22]. These devices, usually come integrated with

a wide range of sensors, capable of measuring physiological and environmental conditions. Such sensors can be characterized in two categories: Biosensors, which are used to monitor a clinical process, allowing measurement of biopotentials and other physical parameters, and peripheral sensors, responsible for sensing environmental conditions, enhancing the awareness of the system [20]. Biosignals then can be generated by several forms of energy, allowing their division between six important groups, as it can be seen in Table 2.1 below.

Form of energy	Parameters	Example of biosignals
Electrical	Voltage, current, resistance, capacitance, inductance, etc.	ECG, EEG, EMG, EOG, ENG
Mechanical	Displacement, velocity, acceleration, force, pressure, flow, etc.	Blood pressure, pulse wave, velocity
Thermal	Temperature, heat flow, conduction	Body core temperature, skin temperature
Radiant	Visible light, infra-red waves, etc.	SpO_2 , photoplethysmography
Magnetic	Magnetic flux, field strength, etc.	Magnetoencephalography, flow meters
Chemical	Chemical composition, pH, etc.	Glucose, cholesterol

Table 2.1: Classification of biosignal according to associated form of energy

Source: [20]

2.2 Photoplethysmography

2.2.1 Brief History

The term “*plethysmograph*” derived from the Greek, and is composed by two words: “*plethysmos*” which means increase, enlarge, and “*graphos*” from graphein, which is the word for writing. Meaning an instrument to obtain tracings showing volume changes of parts of the body. Originally, this is related to volume variations due to blood circulation with the body

part of interest [23]. But it was just in 1938 when Hertzman introduced the term to describe a transcutaneous technique, which would allow registration of blood flow volume changes in a non-invasive procedure [8]. The principle relies on the observation that the light transmitted through the living tissue, acquire a change in time of the heartbeat frequency [8].

2.2.2 Functionality

As mentioned before, PPG is a non-invasive and low-cost sensor to continuously monitor blood volume changes inside capillary vessels using the property of light reflection and absorption, producing usable biomedical information such as HR, oxygen saturation and measure respiratory rates [24, 25]. The signal consists of two major components: a steady DC component and a pulsatile AC component [26]. The DC part corresponds to the light absorption by non-pulsatile blood, skin, bone and other tissues, while the AC component represents the light absorption by pulsatile blood volume changes between the systolic and diastolic phases of the cardiac cycle [27, 28]. As seen in Figure 2.2, the AC component translates the interaction between the blood volume changes with the sensor. It varies with time and has a frequency of about 1 Hz and slowly varies its baseline (DC component). The AC component is provided by the cardiac synchronous variation in the blood, which happens because of the heartbeats. This component depicts changes in blood volume, which represents the systolic and diastolic phases [29]. Features such as rise time, amplitude and shape can predict vascular changes in the blood flow [29]. Also, it is possible to see two unique phases: a rising edge of the pulse, which is also called anacrotic (systole), and falling edge, called catacrotic, which represents diastole. Additionally, a dicrotic notch is usually visible at the catacrotic phase. These features are explained in Table 2.2.

The other component is shaped by respiration, sympathetic nervous system activity, and

PPG feature	Description
Systolic Amplitude	Reflects AC variation in blood volume around the measurement site
Pulse Area	Total area under the PPG curve. Interval between two systolic peaks
Peak to Peak Interval	Interval between two systolic peaks
Large Artery Stiffness Index	The time interval between the systolic and diastolic peaks

Table 2.2: Features of PPG signal

Source: [7]

thermoregulation [7]. While the AC component has clinical importance due their synchrony with the cardiac cycle, the DC component also provide valuable information, such as hyperaemic or hypoaemic states, temperature changes, sympathetic outflow, venous volume fluctuations, and other regulatory mechanisms [30].

The sensor monitor changes in the light intensity, via transmission or reflection. Transmission mode provides a relatively good signal since both sensors, LED and photodiode are across each other, providing a better signal reflectance between them. However, the sensor must be located on the body at a site where transmitted light can be readily detected, such as fingertip, nasal septum or earlobe, for example. This becomes a disadvantage to this mode, since, for daily activities, this might represent interference to movements and reliable acquisition of the signal. Reflectance mode, on the other hand, eliminates this problem, since both sensors are side-by-side, allowing more mobility during data acquisitions. However, MA and pressure perturbances may corrupt the PPG signal and limit the measurement accuracy of physiological parameters [28].

The relation between light and biological tissue may involve scattering, absorption and/or reflection of the signal. For this reason, studies were conducted in order to determine the relation, characteristics, and penetration of the light in human skin. It was discovered that

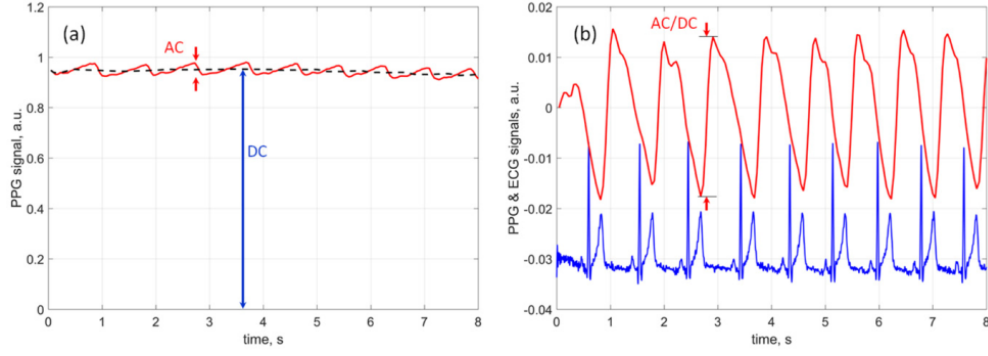


Figure 2.2: Typical waveform of the PPG: (a) AC component (red curve) represents the light absorption by pulsative blood volume, DC (black curve) is a slowly varying component. (b) ratio AC/DC after detrending and inversion. ECG is recorded simultaneously and appears in blue color.

Source: [31]

within the visible color spectrum the dominant absorption peak is found to be in the blue region, followed by the green-yellow spectrum (between 500 and 600nm) corresponding to the red blood cells [9]. Moreover, other studies defend that working on the green range of the spectrum, provides better readability of the sensor, since the green light is absorbed entirely by the body, also providing a good correlation between oxyhemoglobin (oxygenated blood) and deoxyhemoglobin (blood without oxygen present) [32]. This in fact, translates into a greater change in the reflected green light, resulting in a better signal to noise ratio of the signal, providing measurements that are more accurate [25, 28, 33, 34]. Thus, the green wavelength is typically used in reflectance mode, for the measurement of superficial blood flow, while infra-red is usually used in transmission mode PPG sensors, in order to measure blood flow in deeper tissues [28]. As previously mentioned, in Figure 2.3 there is a representation about the spectrum range against absorption for oxygenated and deoxygenated hemoglobin, and it's possible to see that realization of oxygen absorption is higher at the green spectrum range found out by [25, 32, 35, 36].

Even though there is a wide color range of LEDs, which allows different light absorption

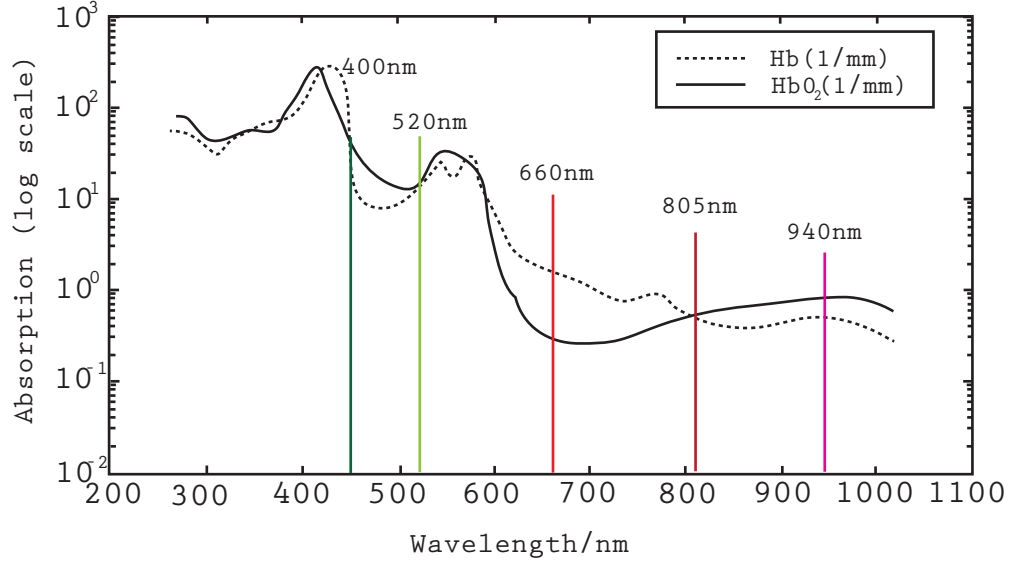


Figure 2.3: The absorption spectrum for oxygenated and deoxygenated hemoglobin is different, allowing the sensor to estimate heart rate and blood oxygenation information of the localized tissue.

Source: [36]

by the tissue, the green LED is considered the most commonly used. This is merely because green light waves penetrate superficially into the tissue, producing the strongest plethysmographic signal for light reflectance measurement and detect pulse rate with a higher degree of precision [34]. As pointed by Maeda et al, 2010, a study was conducted in healthy subjects, which were subjected to different ambient temperatures. Their research investigated that green wavelength PPG sensors, produced a higher correlation with R-R interval (which indicates the heart beat-to-beat interval) of an electrocardiogram, compared with infrared waves, as it is usually also accepted for PPG sensing. Results then, suggested that reflected green light PPG has an advantage over reflected infrared PPG sensors, even more with the temperature variation. Other studies, defend the same concept of light absorption and that detection of pulse rate has a higher degree of precision with a green light for photoplethysmography sensors [25, 28, 35, 37].

2.3 Motion Artifacts

In addition to light wavelengths, previous research identified other side-effects that influence negatively the signal acquisition by PPG sensors. These side-effects are broadly called motion artifacts (MA). This comes mainly from the fact that signal acquisition is decreased and unreliable data information is acquired due to motion and/or environmental noise. It is because of MA that PPG has not yet been widely accepted as a sensor for mobile and health care applications. According to Chong et al. (2014), there are three distinct sources of MA that compromise readability of PPG sensor's acquisition: environmental, physiological and experimental artifacts, which can be attributed to electromagnetic and power interference around the body; cross-talk pickup of other physiological signals and instrumental noise [24]. Other disruptions may be caused by, but not exclusive to a measurement site, contact force, artifacts of mechanical movement, subject posture and breathing, ambient temperature, skin characteristics and blood perfusion [9, 38].

Tissue modifications can alter inner tissues, made voluntary or involuntary by muscles' movements and/or dilatation of other tissues. The light that is received back from the sensor, may be modified by these movements, generating noise, corrupting the correct signal. Individuals anatomy, differences in organ sizes and amount of fluids retained by tissues result in variation of light propagation in the inner layer [7]. Another factor that modifies the signal is the displacement of the sensor relatively with the skin. This, in fact, is caused primarily because the system is sensitive to motion, and the electrode-skin impedance changes over movement too. For wrist-type PPG sensors, during intense hand movement, the gap between the wrist's skin and the sensor changes, and as a result, the measured intensity of the PPG varies with it. This variation is often correlated with the frequency in which the hand moves [39]. As be seen in Figure 2.4, PPG signal is corrupted by MA due to movement and physical displacement between the sensor and skin, during intense physical movement, such

as running, for example.

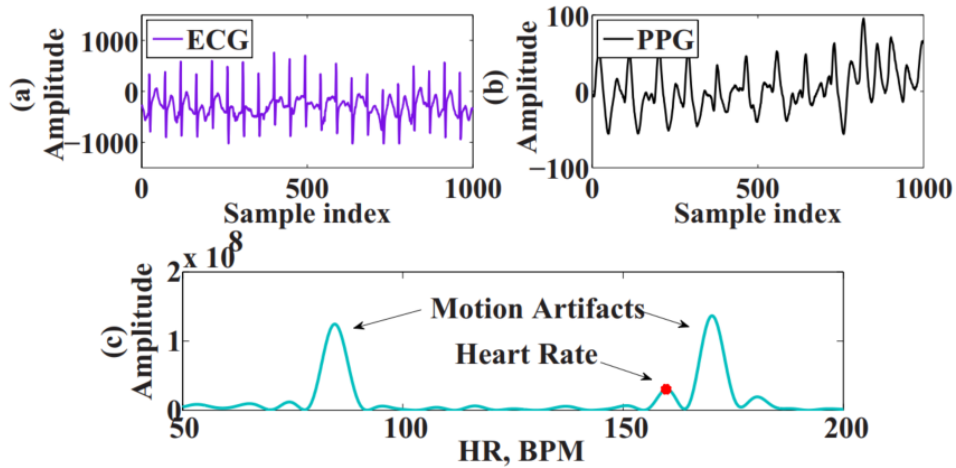


Figure 2.4: (a) A segment of the ECG (ground truth) and (b) corresponding PPG in time domain. (c) Periodogram representation for both cases and spurious MA peaks near the HR peak.

Source: [39]

It might even happen that when the sensor gets so separated from the skin that the original peak corresponding to the HR might be totally absent from the spectrum [39]. Figure 2.5 shows this case.

Sometimes, the frequency of the movement and the HR frequency might get close that the HR peak becomes imperceptible for a given resolution on the periodogram, as in Figure 2.6.

In summary, MA represents a very complex and difficult disadvantage on the use of PPG sensors, however, when tackled with good algorithms to suppress and or/separate its effects, these sensors become a reliable, cost-effective and user-friendly application for health monitoring devices. Another method that has been universally accepted, is the use of complementary sensors, such as accelerometers (ACC) and gyroscopes (GYRO) to mimic the noise presented in the motion, and through the application of filters and other methods, decrease/reject artifacts presented on the data and improve heart rate, and other factors,

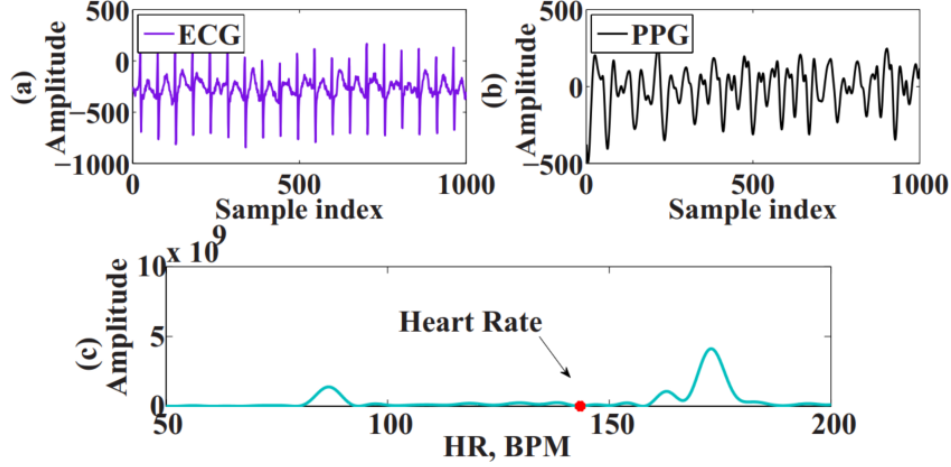


Figure 2.5: (a) A segment of the ECG (ground truth) and (b) corresponding PPG in time domain. (c) Periodogram representation for both cases and no peak detection of HR.

Source: [39]

for example.

2.4 Tissue Optical Characteristics

Methods for determining the optical parameters of tissue can be divided into two large groups: direct and indirect. Direct methods are based on fundamental concepts such as the Beer-Lambert Law, the single scattering phase function for thin samples, or the effects of light penetration in tissues [40]. These methods are advantageous in the way that they are simple analytical expressions for algorithms and reconstruction of data processing. Their disadvantage, on the other hand, is that they are based on experimental conditions which are grounded in a model implying some sort of hardness in the method approach. Indirect models are based on obtaining the solution of the inverse scattering problem using a theoretical model of light propagation. These, on the contrary, are very complex models and time-consuming for algorithm composition. For this reason, direct methods are commonly found in literature and provide a reasonable application for PPG sensors. Optical scattering is the

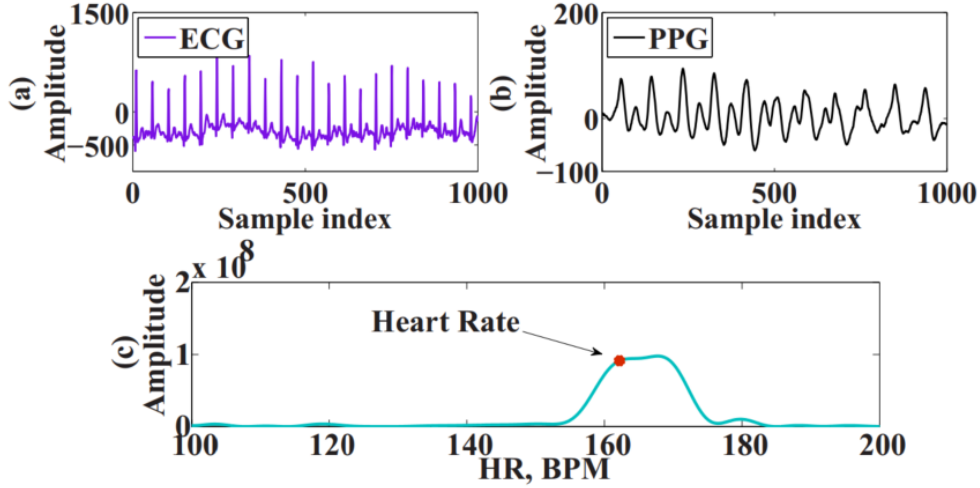


Figure 2.6: (a) A segment of the ECG (ground truth) and (b) corresponding PPG in time domain. (c) Periodogram representation for both cases and MA peak and HR peak are almost imperceptible from each other.

Source: [39]

main disadvantage of PPG sensors, as explained in previous sections. It can be described as either a scattering of particles that have a refractive index different from the surrounding medium, or as scattering by a medium with a continuous but fluctuating refractive index [41]. Medium, in this case is the skin, more concentrated in the outer skin, within dermis and subcutaneous layer, which would contain blood vessels for precise heart rate estimation using PPG sensors. As shown in Figure 2.7, modelling the skin is a very complex and cumbersome method, as there are several variables to be accounted for, such as blood flow, reflectance of the light in different absorption coefficient layers, scattering of the light and temperature, to name a few.

Another constraint is how the light is absorbed for different skin tones. Even though humans have a broad range of skin tones, the intensity and wavelength light that is captured by the PPG sensor depends on the skin tone of the person wearing a wearable device. That is, different skin tones absorb light differently, thus being characterized by a different

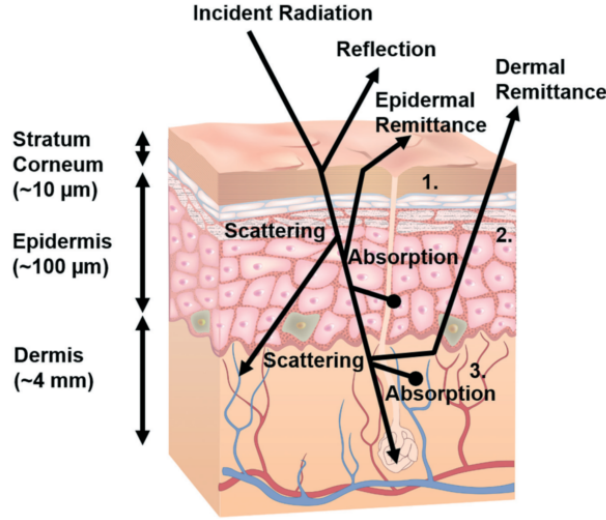


Figure 2.7: Schematic diagram of optical pathways in skin. Keratinized squamous cells (1) and large melanin aggregates (2) are responsible for absorption and scattering. The vascularized dermis (3) includes absorbers such as oxygenated and deoxygenated hemoglobin, caroten and bilirubin.

Source: [42]

absorption spectrogram [38]. There is even a scale proposed by Fitzpatrick in order to categorize as a numerical classification of skin tones and their response to ultra-violet light. In the wavelength range of 350-1200nm, which is the spectral range where PPG sensors work, melanin is the major absorber of radiation in the epidermis, especially at shorter wavelengths [43]. Dermal scattering, therefore, portrays an important topic in determining the depth of the radiation of different wavelengths that penetrate the dermis [44].

Not only skin tone but also pigments can influence negatively with PPG sensoring. Apple watch users' who have tattoos on the wrist, encountered some problems using the device to measure heart rate. This happens because the ink present on tattoos can interfere with an accurate reading as they may block the light from penetrating the skin [45].

2.5 Sensor Location

Anatomical measurement sites influence how optical HR sensors interpret biosignals. Since the sensor has direct contact with the skin, light reflected and/or absorbed also varies with the sensor location. Usually, sensors are placed in the finger (transmissive method), but also in the hand, forehead, ankle, arm, chest, wrist and ear, but mostly in these last 3 regions. According to Tamura et al. 2010, flow to the skin of trunk, arms, and legs was almost equal and showed much less flow compared with palmar and plantar surfaces and the skin of the face and head [46]. Moreover, they found out that the peripheral pulse characteristics vary across individuals and since peripheral areas have a larger vascular bed, amplitude and variation in perfusion volume are greater at these peripheral sites. Nevertheless, since green light is less sensitive to differences in perfusion, it is less sensitive in different anatomical regions.

Even though there are several locations where PPG sensors could be used and depending on those, the signal acquisition may differ significantly, comfort and mobility are prerequisites to choose a PPG sensor location for wearables. Since wearables have attracted serious attention from both the research community and industry, these state-of-the-art technologies still struggle with size, portability and battery consumption. Due to these facts, the end-user is constantly looking for comfort, better experience, and reliability. Thus, the best solution for wearable health monitoring is to integrate as many functionalities and sensing applications into one single device, enhancing user experience and convenience [47]. One of the best locations for wearables is the wrist, compared to other sites, such as chest, forehead, and ears, even though these might provide a slightly better signal-to-noise ratio than sensors on the wrist, they become a challenging and cumbersome monitoring device solution when it comes to the user accessibility and comfort. Now, in terms of technical challenges, the wrist

is not appropriate to locate such sensors, mainly because of motion artifacts and size limitation. In modalities that require strong motion, PPG signals may get mixed up with motion frequencies, resulting in doubtful information. In addition, hand movements also may cause physical displacement of the device with the skin, altering the light reflected/absorbed by the sensor, introduce noise on the readings and/or change skin impedance, which as mentioned before, contributes negatively for good quality signal acquisition. Device dimensions, also reveal a negative impact while using PPG sensors located on the wrist, since they need to be small and lightweight as possible, so the user feels comfortable when using in a long period of time [20].

2.6 Perfusion

Perfusion is the process of a body delivering blood to a capillary bed in tissue for tissue oxygenation and cellular metabolism. For different skin tone, the level of perfusion varies between individuals. Problems such as obesity, diabetes, heart conditions and arterial diseases lower, even more, these levels. Body extremities retain lower perfusion, which can reveal challenges for health monitoring systems, since signal-to-noise ratio may drastically decrease, once lower perfusion correlates with lower blood flow signals. Depending on the population set that is using a wearable device, for example, elderly people, which tend to have lower perfusion, it tends to impact negatively with the accuracy of these devices. Also, the pulsatile flow at peripheric sites is most vulnerable when there is a diversion of blood flow to more vital organs due to temperature drop [48].

2.7 Crossover Problem

Continuous repetition or similar motion is also considered a major problem for wearable devices. This happens because the cadence or step rate of the movement, may overlap or crossover with the incoming optical data, presenting unreliable information. This is usually seen with an activity that involves repetitive movement, such as jogging and running since the step rates measured during these actions fall within the same general range as that of heartbeats (140-180 beats/steps per minute) [38]. In Figure 2.8, when the heart rate and step rate crossover each other, many wearables tends to lock on to step rate and present that measurement as heart rate, which may not be the case since the heart rate might change drastically after the crossover.

Comparing Optical Wrist HRMs for Apple Watch vs. PerformTek
During a High-Intensity-Interval Treadmill Run

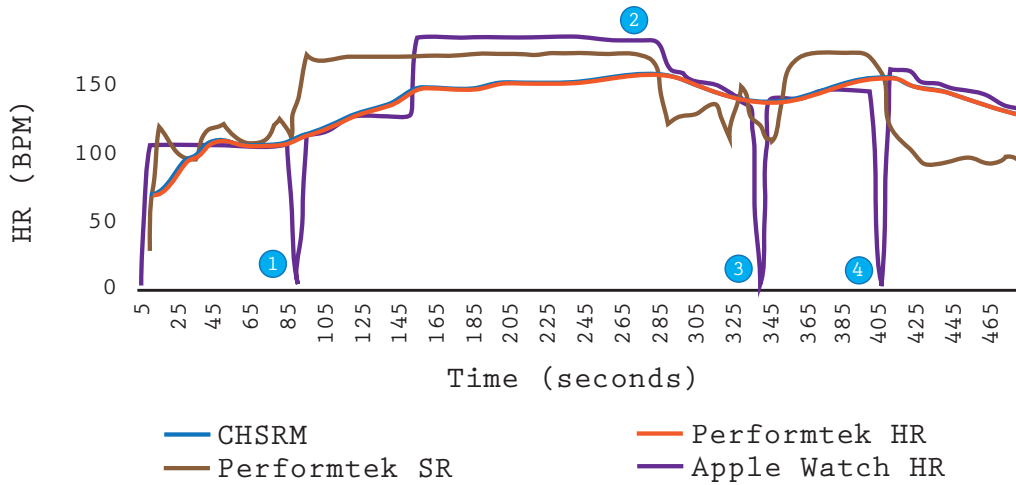


Figure 2.8: Comparing Heart Rate Monitoring devices (HRM), it is apparent that Apple Watch exhibits heart rate monitoring failure during “cross-overs”, where the person’s step rate and heart rate were so similar that the algorithm could not sufficiently differentiate between them; #2 this crossover event caused a faulty HR reading for more than 2 minutes, where the true HR was mistakenly report as the step rate (cadence).

Source: [38]

2.8 Advantages

Heart rate monitoring (HRM) techniques that rely on photoplethysmography sensors present several advantages over traditional ECG based systems. Size and portability is a unique characteristic for PPG sensors. As explained before, HRM through PPG requires the need of a single sensor to be placed on the skin, in contrast with ECG which uses at least three channel electrodes that require attachment in different parts of the body, for a reliable data acquisition (a “12-lead” ECG is usually used). This requirement greatly restricts patients mobility. In addition, PPG sensors can be placed in the extremities, allowing other parts of the body to be independent of the readings, permitting flexibility of motion and if they are placed at specifically easy accessible anatomical positions, signals can also be collected with higher quality [7]. PPG sensors do not require a galvanic connection between patient and base-unit, allowing a safer environment to higher isolation voltages. Even though it is possible to perform ‘non-contact’ electrocardiography [49,50], the method is subjected to environmental noise and motion artifacts, limiting the use to potential applications. Another advantage is the easy and fast acquisition of data. PPG sensor devices are not time-consuming, compared to ECG, which require electrodes adherence in different body parts, hydrogel application on electrodes (in order to maintain hydrated and good connectivity with the skin) and time to set up the necessary equipment for an ECG procedure.

In addition, the baseline advantage of monitoring HR as a non-invasive method added to the performance of a “non-contact” application, PPG sensors can be integrated into wearable devices, enhancing comfort and user experience, allowing high data reliability for health monitoring devices.

2.9 Challenges

One of the limiting factors for PPG acceptance comes from its own mode of operation. Each mode, transmission, and reflectance should be well study before implementation. In transmission mode, the light source and detector are separated by the tissue, but too much pressure can slow down and interfere with peripheral blood flow, causing reduction of venous oscillations [7]. The waveform obtained by PPG differs depending on the pressure contact with the tissue. Ideally, the best PPG signal can be obtained under conditions of transmural pressure, defined as the pressure across the wall of the blood vessel. However, PPG under excessive pressure can lead to low AC signal amplitude and distorted waveforms [9]. On the other hand, for reflectance mode, the light sources and light detector are placed on the same surface, therefore can be placed within one patch. This contributes to MA being sourced to both sensors, besides having the light scattered in every direction.

Size influences on the hardware level as well. As shown in Table 2.3, as the detector moves closer to the emitter, it decreases the signal-to-noise-ratio, since there is a higher percentage of critical light into the detectors, causing the light to not interact with the tissue. When the spacing between the detector and emitter increases, it captures less total light into the detector, but allows more light to interact with blood flow, providing a cleaner signal to the device [51].

Also, most heart rate monitoring devices support PPG and other sensors, such as accelerometers. The integration of this multi-platform is not simple, and implicates challenges due to size limitation, power consumption and transfer bandwidth [47]. Integration of several components, power management for life endurance, are considered big challenges in today's electronic history. In order to improve these, novel system architecture and better estimation of battery cycle and expenditure may be required. Lastly, motion artifacts as

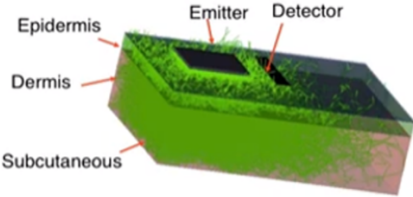
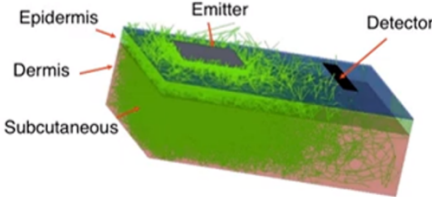
Close (2 mm) source-detector spacing	Wide (4 mm) source-detector spacing
	

Table 2.3: Wider spacing between source-detector captures less total light, but has a higher ratio to blood-flow scatter compared to motion-related scatter.

Source: [38]

mentioned before, are considered the biggest challenge for PPG sensors. In practical systems, MA in PPGs is more severe if compared to MA in ECG devices. ECG requires a strong and fixed electrode-skin contact, while PPG sensors rely on the optical reflection signal that is reflected/transmitted from the tissue. More recently, MA in PPGs has become an interesting topic among researchers and in the wearable industry. Several methods have been discussed and implemented, but there is still a need to accurately estimate HR information, even though there are severe MA presented.

2.10 Existing Research

Extensive research has been developed related to PPG sensing. As previously shown, motion artifacts influence on this sensor readings, motivating more and better methods/algorithms in order to extract reliable information of heart rate, oxygen saturation and blood pressure, among other biosignals. Various approaches to mitigate MA reduction have been proposed. Some of them are related to sensor attachment [52] and localization [25]; even though this

approach enhances expectation for better signal acquisition, it doesn't provide a significant reduction of MA. Others are more concerned in the classification of the PPG signal for medical applications based on machine learning approaches [53, 54], although reported accuracy is currently similar to other processing methods. On the other hand, most proposed methods in literature usually model MA with motion sensors, such as accelerometers (ACC) and/or gyroscopes (GYRO). These sensors can be used as reference signals for adaptive filtering, for example [14]. Some other adaptive algorithms such as Adaptive Least Mean Square (LMS) [55], or Normalized Least Mean Square adaptive noise canceler (NLMS) have already been proposed [56] to solve this problem. Other methods for attenuating MA in PPG have been implemented such as blind source separation through Principal Component Analysis (PCA) [57], or Independent Component Analysis (ICA) [58] and Singular Spectrum Analysis [24]. Others, rely on techniques such as Singular Value Decomposition (SVD) [59], Kalman Filtering (KF) [2], particle filtering [60], Wiener filter [61], etc. As for frequency-based methods, wavelet noise reduction [14] and power spectral analysis [2, 62] are also implemented. As can be seen, MA is a problem that needs to be addressed properly for accurate HR estimation through the use of photoplethysmography sensors.

Chapter 3

Methodology

Photoplethysmography sensors provide a novel and accurate way for estimating HR information as an unobtrusive system on wearable devices. However, as explained in section 2.3, HR information may become unreliable due to MA, resulting in wrong measurements. This, on the other hand, allows research development and implementation of better, faster and more accurate methods for HR estimation using PPG sensors. Research has been done in this area, and common sense is already set regarding the block sedimentation for accurate HR estimation. The majority of well known published methods follow this procedure, which comprises basically of 3 main stages as shown in Figure 3.9.

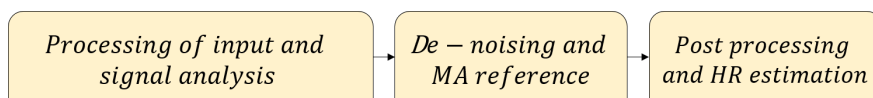


Figure 3.9: Flowchart of 3 main stages for HR estimation.

Figure 3.9 represents the common framework found in the literature. The first stage comprises retrieving sensor available information, such as ACC, GYRO, and PPG sensors,

filtering out the bound frequency ranges and preparation for the oncoming stage. Denoising and MA reference translates into receiving filtered sensor information and combination/subtraction of specific features in order to prepare for estimation. In the final stage, the signals have already been cleansed and MA artifact reduction has been applied; this stage deals with final HR estimation, prediction and smoothing of the HR measurement.

3.1 HR Estimation Methods

There is a wide range of HR estimation methods, some focusing on accuracy and others in performance. This happens since different methods may present accurate results, but demand very complex calculations, costing, on the other hand, in algorithm performance and implementation. Moreover, usually datasets follow several restrictions, and it becomes very difficult to produce an evaluation between different methods and replication of results. Even though this is the case here, the dataset publicly available in [1] still manages to provide a vast spectrum range of PPG signals while patients perform several physical activities.

3.1.1 Dataset

The trace library employed for trials provides a comprehensive set of test cases. It comprehends datasets for 23 individuals divided as follows: The database that includes 13 traces are subjects aged from 18 to 35 years old, recorded while running, and 10 other traces from eight subjects during arm rehabilitation exercises and boxing. All males are healthy, and the female subject has abnormal heart rhythm and BP. The test set up is composed by data of two green LED PPG sensors at 515 nm, a tri-axial ACC, all data being collected from a wrist-type PPG wearable device. True heart rate is also available by ECG trace acquired from electrodes placed on the chest. Usually, each dataset lasts about 300 seconds, which

turns out producing around 40,000 samples of data. All signals are sampled at a frequency of $f_s = 125$ Hz and estimations are taken every 8 seconds of data, with an overlap of consecutive windows of 6 seconds. HR estimation is done every $T_s = 2$ s, corresponding to a report rate of 0.5 Hz.

Table 3.4: Database of 23 PPG recordings from IEEE SP CUP [1]

Rec	Subject ID	Activity Type	Age/Weight/Height	Sex	Healthy?
1	1	T1	18-35y/-/-	M	Y
2	2	T1		M	Y
3	3	T1		M	Y
4	4	T1		M	Y
5	5	T1		M	Y
6	6	T1		M	Y
7	7	T1		M	Y
8	8	T1		M	Y
9	9	T1		M	Y
10	10	T1		M	Y
11	11	T1		M	Y
12	12	T1		M	Y
13	13	T2	20y/64kg/162cm	M	Y
14	14	T2	29y/70kg/169cm	M	Y
15	15	T2	21y/77kg/188cm	M	Y
16	15	T3	21y/77kg/188cm	M	Y
17	16	T3	19y/54kg/174cm	M	Y
18	13	T3	20y/64kg/162cm	M	Y
19	17	T3	20y/57kg/174cm	M	Y
20	18	T2	19y/70kg/180cm	M	Y
21	18	T3	19y/70kg/180cm	M	Y
22	19	T3	21y/73kg/180cm	M	Y
23	20	T2	58y/70kg/156cm	F	N**

T1 = walking/running on a treadmill. T2 = rehabilitation arm exercises. T3 = intensive arm movements (boxing) ** Abnormal heart rhythm and blood pressure were noted.

The details of the database are given in Table 3.4. Three main activities were performed. Type 01 involved activities of walking or running on a treadmill. The subjects were asked to purposely use the hand with the wrist band to perform usual activities as dressing, pushing

buttons on the treadmill, etc. The activity followed the pattern shown in Table 3.5.

Table 3.5: Activity level performed for dataset in [1].

Activity Type	Resting	Walking	Running	Walking	Running	Resting
Data 01	-	8km/h	15km/h	8km/h	15km/h	-
Data 02	-	6km/h	12km/h	6km/h	12km/h	-
Duration	30s	60s	60s	60s	60s	30s

Activity type 02 included various forearm and upper arm exercises, which are common in rehabilitation (e.g. shake hands, stretch, push, running, jump and push-ups). Type 03 activity consisted of intense forearm and upper arm movements (e.g. boxing).

3.1.2 Comparison Between Methods

State of the art methods such as [1] have recently been proposed to estimate HR from PPG signals where scenarios of MA are very strong [25]. The method was based on signal decomposition, sparsity-based high-resolution spectrum estimation and peak tracking detection reporting average absolute error of 2.34 beats per minute (BPM) on 12 PPG recordings. This method was enhanced in [63] where spectra of PPG and ACC signals were jointly estimated using common sparsity constraint to reduce error. The database of 23 PPG recordings of people running or performing intense physical activity is available publicly for algorithm evaluation. The rules and evaluations presented in the database allow comparison between different methods. Since the published database, several HR estimation algorithms have already been implemented and tested [2, 16, 24, 25, 56, 61, 68] and others have been compared in Appendix A.

In [12], PPG signal extraction is done by spectrum estimation using the Lasso method, even though reporting reasonable HR estimation, the method required several tuned parameters for a smoothed measurement. In [14] MA cancellation is performed by Singular

Value Decomposition (SVD), even though it presents reliable results due to the robustness of the decomposition technique, it demands high performance of the device for algorithm implementation. In [15] the method is performed by organizing estimated HR frequency peaks over spectrum estimation, the method is efficient in computational time and memory storage, however, it depends entirely on peak selection threshold values. This may present as a fast algorithm implementation, but might underperform in other datasets. In [16], even though Fast Fourier Transform (FFT) might underperform when compared to Short-time Fourier Transform, the use of moving average filters add a memory to the system, which can contribute negatively for real-time applications. Although they report improvements in performance, available methods are usually accompanied by the increased number of free parameters, which may indicate a sign of overfitting given the size of data available in the dataset. Moreover, although the whole database of 23 recordings is available since 2015, several recent methods still prefer to report results on the ‘easier’ part of the dataset. In [61] the approach to HR estimation is based on Wiener filtering and phase vocoder, not relying on a set of heuristic rules and thresholds values if compared to previous methods. This method requires a few parameters to be tuned and provides a reasonable HR estimation for the available dataset. However, when analyzed to other datasets or with the proposed simulation tool, this algorithm performs poorly when compared to more sophisticated methods. In addition, even though studies reported improvement of HR estimation, there is a trade-off between precision and performance [2]. It is reported in [1] that in order to estimate HR for the first 12 recordings [1] takes several hours, [63] takes around 5 minutes, [39] takes 200s and [14] takes several hours for HR estimation. In [2] MA reduction is based on the degree of decorrelation between the accelerometer and the PPG signal. However, parameter estimation is assumed as constant, variances of noise and measurement in published Kalman algorithms for HR estimation are set values, assuming that parameters should be the same

independently of user physiology. This assumption, even though it may work for limited recordings, it won't precisely estimate for different datasets.

3.2 Proposed Algorithm

In this study, novel parameter estimation is presented based on the Expectation Maximization (EM) algorithm and Kalman filter (KF). Kalman filter represents the optimal solution for tracking, assuming that estimated parameters are known. Since user physiology varies, it becomes difficult to estimate the variance of noise presented for each individual. Thus, through the EM algorithm, it's possible to estimate these parameters independently of the user rather than assuming predetermined values. This in fact, produces a better parameter estimation, which reflects in a more accurate estimation of HR measurement. In addition, a novel simulation tool is developed for evaluation of known HR estimation methods. This tool allows comparison of different methods independently of the signal duration. Thus, the ability to produce synthesized data, provides the researcher an easier way for algorithm evaluation. In Chapter 4 the simulation tool is demonstrated and known HR estimation methods are compared.

The flowchart of the HR estimation system is shown in Figure 3.10. Accelerometer and photoplethysmography signals are filtered and segmented following the same procedure as in [2]. Through SVD method, segmented signals are used to find a subset of filtered PPG signals that contain all useful information to estimate HR. Frequency analysis is performed in these denoised signals allowing estimation of HR measurement by locating the largest spectral peak in the reconstructed signal spectrum as in [2]. These raw HR measurements (z_{ppg1} and z_{ppg2}) are passed through a KF allowing a smoother HR estimation, while the EM algorithm iteratively updates KF parameters, based on the data received, producing a

more accurate HR measurement. This developed system is described in detail in Section 3.2. Section 3.3 briefly explains the HR model and its parameters. Section 3.2 gives a brief overview of the EM algorithm and provides the proposed solution for estimating autonomous HR information using the EM algorithm and in Section 3.5 and 3.5.2 metrics and performance of the proposed approach are demonstrated for both simulated and real data.

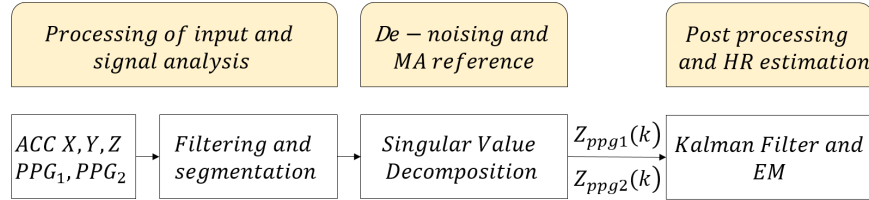


Figure 3.10: Flowchart of HR estimation system. Proposed algorithm belongs to the final block (KF & EM)

3.2.1 Framework

As explained at the beginning of Chapter 3, the problem with HR estimation through the use of PPG sensors demands a very complex algorithm and a structured process for reliable HR estimation. Thus, it's possible to divide the problem of reliable HR estimation using photoplethysmography sensors into the following stages: processing of input signals, such as PPGs and sensors such as accelerometers and/or gyroscopes for filtering and segmentation; de-noising and MA reference for correct cardiac cycle analysis and post-processing for tracking and predictive HR estimates. This main stage procedure is explained below:

3.2.2 Processing of input signals

First, both PPG and ACC signals are filtered to remove out-of-bound frequencies and smooth of the signal. This is performed by using a 4th order Butterworth filter with a bandwidth of

0.67-3.67 Hz. This represents the possible range of HR measurements that an individual can experience while in physical activity and comprehends the boundaries of minimum and maximum HR values an individual can respond (40BPM - 220BPM). Secondly, segmentation is applied since the sampling frequency $f_s = 125\text{Hz}$ and the observation window T_w is analyzed within 8 s of data, which represents $N = 1000$ sample points. The HR is then estimated at every $T_e = 2$ s since the windows have an overlap of 75% (i.e 6 s) as in [1]. Thus, the HR value is estimated every 2 s, corresponding to a reporting rate of 0.5 Hz.

3.2.3 De-noising and MA reference

The recorded signal can be filtered and cleansed by SVD selecting all useful information from the PPG sensor. That means, the noise reference signal is generated from decomposed data of the acceleration signals and the degree of decorrelation with PPG signals, as done in [2]. In every 8-second window of data T_w , SVD is applied to maintain all useful information preserved in the matrix, while the interference caused by MA is reduced. The criterion for principal signal component selection is based on the degree of decorrelation with the ACC signals. As pointed out in [2], the process is done for each batch of data, allowing to reconstruct denoised versions of both PPG signals. Now, reference signals for adaptive filtering are generated by decomposing the three-axis acceleration signal into singular components. The PPG signals are filtered using all singular acceleration signal components successively by SVD. For each data segment $ppg_1(nTs)$ or $ppg_2(nTs)$ of length N , obtained from either of the two PPG sensors, and for each triaxial accelerometer output, respectively, $\mathbf{a}_x(nTs)$, $\mathbf{a}_y(nTs)$ and $\mathbf{a}_z(nTs)$, trajectory matrices are formed: \mathbf{D}_{ppg_1} , \mathbf{D}_{ppg_2} and \mathbf{D}_{a_x} , \mathbf{D}_{a_y} and \mathbf{D}_{a_z} . For a PPG sensor output $ppg(nTs)$, vectors $\bar{\mathbf{s}}(j)$ are defined as:

$$\bar{\mathbf{s}}(j) = [\mathbf{s}(jTs)\mathbf{s}((j+1)Ts)\dots\mathbf{s}((j+L-1)Ts)]^T \quad (3.1)$$

with $L \leq N$. The corresponding vectors $\bar{\mathbf{d}}_s(j)$ are obtained by subtraction of the mean $\boldsymbol{\mu}_s(j)$ from each element of $\mathbf{s}(j)$.

$$\boldsymbol{\mu}_s(j) = \frac{1}{L} \sum_{i=1}^L \mathbf{s}[(j+1)T_s] \quad (3.2)$$

$$\bar{\mathbf{d}}_s(j) = \bar{\mathbf{s}}(j) - \boldsymbol{\mu}_s(j) \quad (3.3)$$

The trajectory matrix \mathbf{D}_s is then

$$\mathbf{D}_s = [\bar{\mathbf{d}}_s(1) \bar{\mathbf{d}}_s(2) \dots \bar{\mathbf{d}}_s(J)] \quad (3.4)$$

with $1 \leq j \leq J = N - L + 1$. In the same manner, \mathbf{D}_a is formed with accelerometer output samples arranged in vectors $\bar{\mathbf{a}}(j)$. Singular value decompositon returns for any of the trajectory matrices the following:

$$\mathbf{D} = \mathbf{U} \boldsymbol{\Sigma} \mathbf{V}^T \quad (3.5)$$

where $\mathbf{U} = [\bar{\mathbf{u}}(1) \bar{\mathbf{u}}(2) \dots \bar{\mathbf{u}}(J)]$ and contains the left singular vectors of \mathbf{D} , matrix \mathbf{V} is formed by the right singular vectors and $\boldsymbol{\Sigma}$ is the diagonal matrix of singular values, in decreasing order. The subspace applied to $\mathbf{s}(nT_s)$ is done with the purpose of finding an index subset $J_{PPG} \subset \{1, \dots, J\}$ allowing that all useful information from the PPG sensor output is preserved in the matrix as:

$$\mathbf{D}_{PPG} = \sum_{j \in J_{PPG}} \bar{\mathbf{u}}_s(j) \cdot \boldsymbol{\Sigma}_s(j, j) \cdot \bar{\mathbf{v}}_s(j)^T \quad (3.6)$$

while the interference of the motion artifacts, modeled by the accelerometer signals, are minimized. Now, the proposed criterion for principal component selection is based on the degree of decorrelation with the accelerometer signals. This means that by considering the left eigen vector matrices \mathbf{U}_s and \mathbf{U}_a , whose columns are direction vectors for the principal components of $\mathbf{s}(nT_s)$ and $\mathbf{a}(nT_s)$, respectively. PPG components of $\mathbf{s}(nT_s)$ are minimal along the principal acceleration component. Accordingly, for each accelerometer axis, the principal component can be associated as:

$$\mathbf{C}_{s,a}(i) = \max_{1 \leq j \leq J} \mathbf{u}_s^T(i) \mathbf{u}_a(j) \quad (3.7)$$

Then, the subset formation of J_{PPG} is done by selecting the principal components of $\mathbf{s}(nT_s)$ for which the sum of indices in 3.7, computed over the three accelerometer signals, is below a set threshold value τ

$$\mathbf{J}_{PPG} = \{i : C_{s,a_x}(i) + C_{s,a_y}(i) + C_{s,a_z}(i) < \tau\} \quad (3.8)$$

The threshold value used is the same as presented in [2] and it was a refined version from [64]. The process is performed at every batch of data and for both PPG channels. This allows a reconstruction of denoised version of both sensors, as seen in Figure 3.11. Figure 3.11 shows the spectrum comparison between raw PPG and ACC signals, along with PPG denoised signal, accomplished by the SVD decorrelation method. Spurious peaks that are outside the true value (REF) are minimized allowing a reconstruction of the PPG signal for correct HR estimation.

Frequency analysis is performed after the signal is cleansed by the SVD de-noising stage. The initial HR measurement is obtained by the frequency analysis of the denoised PPG signal. As in [2] HR frequency should have a minimum resolution of one BPM, which

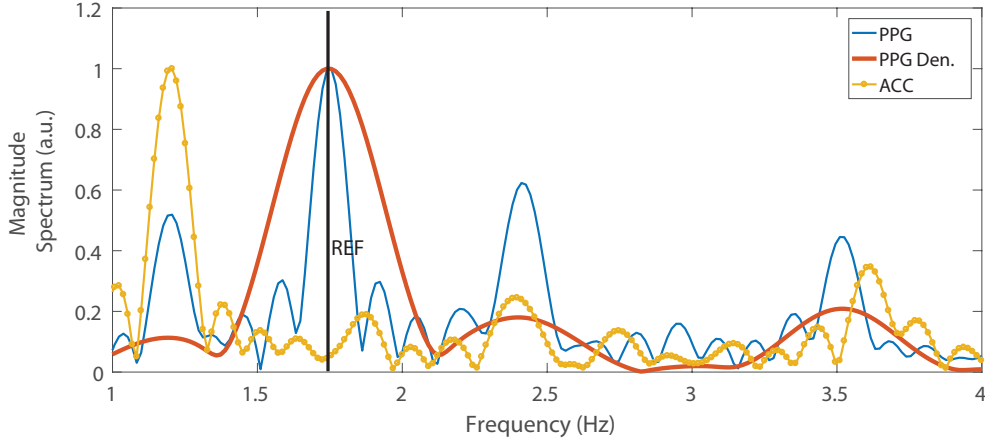


Figure 3.11: Spectrum comparison of raw PPG signal, ACC and denoised PPG signal, after denoising stage with SVD method.

indicates a need to detect a minimum frequency shift $\Delta_f < (1/60)$ Hz. This represents an enhancement of 7.5 times than the grid step obtained by a Discrete Fourier Transform (DFT) with the 8-s observation window T_w . On the other hand, extending the signal acquisition to 60-s of data is impractical. Thus, there is a trade-off between resolution and performance. By zero-padding the signal to extend the DFT to 2^{13} bins, the grid step is re-defined with frequency bins of $\simeq 15\text{mHz}$. Since the spectrum of PPG signals is parameterized of harmonic components this grid resolution would be enough to resolve them [2]. Thus, HR frequency can be estimated by finding the largest spectral peak in the reconstructed signal spectrum as:

$$peak = \arg \max_m |X(mf_{peak})| \quad (3.9)$$

where $X(mf_{peak})$ is the zero-padded DFT of the denoised signal. The frequency estimate for the k_{th} observation window T_w is calculated as $z(kT_e) = mf_{peak}(kT_e)f$. Since the signal was bound by frequency as in section 3.2.2, the set range of acceptable frequency values are in

accordance with physiological parameter limits. As explained in section 2.3, sometimes the HR estimated value may fall in the same range of the MA frequency, this would indicate that the denoised version would have eliminated both MA and PPG frequency peaks. In order to overcome this problem, the frequency estimate obtained from the analysis of denoised data is compared with the estimate of unprocessed data. The occurrence of this condition can thus be detected and accurately processed for correct frequency estimation. To conclude, this stage follows the same implementation done in [2], since the SVD method for MA reference and denoising produces a better-denoised refinement for the signal acquired by PPGs without the interference of the movement, which translates into saving the meaningful information of the signal for reliable frequency estimation.

3.2.4 Post processing and HR estimation

The HR measurements provided by the previous stage, that represents the frequency estimation by DFT are still considered raw measurements. This comes from the fact that even though the majority of signal denoising done by SVD in addition with spectrum estimation accomplished by the DFT, HR estimated frequencies still can be produced by unreliable signal input. For this reason, this final stage deals with the final estimation, filtering and smoothing of the signal, providing a considerably more accurate HR measurement. This is accomplished by the optimal Minimum Mean Square solution: Kalman filter.

According to the discrete model-based on the discrete-time random walk process as in [2]

$$x_{k+1} = Fx_k + v_k \quad (3.10)$$

where x_{k+1} is the current HR value and v_k is a zero mean white noise random process with finite variance σ_v^2 . The refined HR estimate is obtained by the KF presented in Figure 3.12,

$x_{k|k}$ denotes the KF estimate of the HR given all the measurements up to time k and $P_{k|k}$ is the variance of this estimate. The observation model for the HR tracking problem comes down to

$$z_k = Hx_k + w_k \quad (3.11)$$

where x_k is the true HR (see (3.10)) at the sampling instance k , z_k is the measured HR, v_k is the process noise that is assumed zero-mean Gaussian with s.d. σ_v , and w_k is the measurement noise that is assumed zero-mean Gaussian with s.d. σ_w . Further, σ_w can be estimated through the signal processing steps described in Section 3.2. Figure 3.12 represents the detailed block implementation of the KF used in our algorithm as in [2]. For standard KF the observation model equation follows exactly as in (3.11), however, for the implemented KF of Figure 3.12, the observation model has two measurements referenced as z_{ppg1} and z_{ppg2} .

This block diagram is essentially a fusion method of two measurements. Broadly, the fusion is performed based on innovation – the new measurement out of z_{ppg1} and z_{ppg2} that produces the less innovation is selected. That means, the Kalman Filter in [2] process these two raw estimates z_{ppg1} and z_{ppg2} , in order to obtain a single estimate of the actual HR. However, values of σ_v^2 and σ_w^2 are related to the subject, and vary significantly depending on the user. In [2], these values are “hard-wired”, assuming that they do not change for different subjects, independently of their physiology or other parameters, such as body temperature and step cadence. This assumption might work for a specific dataset, but may diverge for different users, ages and anatomy, for example. For this reason, there is a need to estimate those parameters iteratively, providing an accurate HR estimation independently of user physiology.

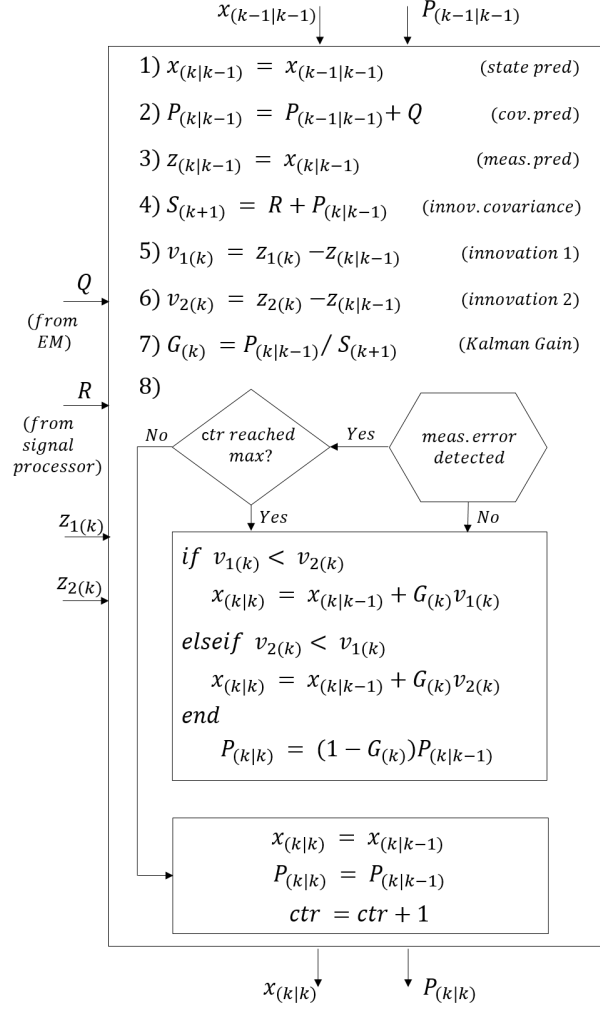


Figure 3.12: Detailed Kalman Filter diagram from [2].

3.3 Problem Definition

The KF approach to track HR, developed in [2], infers set model parameters, such as the process noise variance σ_v^2 and the measurement noise variance σ_w^2 , assuming that the noise accumulated by the PPG sensor can vary depending on physiological features, activity level, etc. Similarly, the process noise variance can vary from person to person and from one activity to another. Hence, rather than assuming predetermined values for σ_v^2 and σ_w^2 , as it

is done in [2], they are estimated. In section 3.2, we summarize the EM algorithm that is developed in, to estimate σ_v^2 and σ_w^2 of the state-space model of (3.10) and (3.11).

Now, given the instantaneous measurements z_k , the objective is to recursively estimate the x_k . The Kalman Filter gives the best estimate for x_k given that all model parameters, F, H, σ_v and σ_r are known. Unfortunately, the process model 3.11, parametrized by σ_v and σ_w , is closely related to the individual's physiology and as such not precisely known. The objective to develop an approach that concurrently estimates the process model parameters as well as x_k the desired state. The proposed approach is described in Section 3.2.

3.4 Review of the EM Algorithm

3.4.1 The EM Algorithm

In this section, we give a brief review of the Expectation Maximization (EM) algorithm [65–67]. Consider the following scenario where N observations

$$\mathcal{Z} = \{z_i\}_{i=1}^N \tag{3.12}$$

are generated from a set of parameters Θ . The likelihood of the parameter Θ given the above observations (that is assumed independently and identically distributed – iid) is given by

$$\mathcal{L}(\Theta) = p(\mathcal{Z}|\Theta) = \prod_{i=1}^N p(z_i|\Theta) \tag{3.13}$$

Now, the maximum likelihood estimation of the parameters is given by

$$\hat{\Theta}_{\text{ML}} = \arg \max_{\Theta} \mathcal{L}(\Theta) \quad (3.14)$$

The above optimization in (3.14) is sometimes intractable because of the nature of the observation model. The EM algorithm offers an approximate, iterative way to perform this optimization.

The EM algorithm starts by considering that the observed data \mathcal{Z} is *incomplete*; i.e., it assumes that there is a certain information that the observations \mathcal{Z} doesn't have; let us denote this *missing information* as \mathcal{X} . With that, the *complete data* is written as $\mathcal{Z} = (\mathcal{Z}, \mathcal{X})$. Using Bayes' theorem, the joint density function of this complete data can be written as

$$p(z|\Theta) = p(z, x|\Theta) = p(z|x, \Theta)p(x|\Theta) \quad (3.15)$$

Now, instead of writing the likelihood function as a function of Θ , such as $\mathcal{L}(\Theta)$ in (3.13), a new function is defined as follows

$$Q(\Theta, \Theta^{i-1}) = E [\log p(\mathcal{Z}, \mathcal{X}|\Theta) | \mathcal{Z}, \Theta^{i-1}] \quad (3.16)$$

where the expectation is with respect to the probability density function of \mathcal{X} ; as such, the resulting quantity $Q(\Theta, \Theta^{i-1})$ is not a function of \mathcal{X} . In summary, we introduced a variable \mathcal{X} to define the likelihood function and then removed that same variable by taking an expectation. The positive effect of this process is that the resulting $Q(\Theta, \Theta^{i-1})$ is in a form that can be easily maximized.

Similar to the likelihood function $\mathcal{L}(\Theta)$, $Q(\Theta, \Theta^{i-1})$ is dependent on Θ ; in addition, it is also dependent on Θ^{i-1} , the *initial guess* on Θ . Now, the expectation step above is formally

written as:

Expectation Step:

$$\begin{aligned} Q(\Theta, \Theta^{i-1}) &= E [\log p(\mathcal{Z}, \mathcal{X}|\Theta)|\mathcal{Z}, \Theta^{i-1}] \\ &= \int_x \log p(\mathcal{Z}, x|\Theta) f(x|\mathcal{Z}, \Theta^{i-1}) dx \end{aligned} \quad (3.17)$$

It must be noted that the probability density of x , $f(x|\mathcal{Z}, \Theta^{i-1})$, is not yet defined; how to find such a density is one of the practical aspects of EM algorithm design. In the next section, we will show how to select (and estimate) such a density using Gaussian mixture density estimation as an example. It is important to note that such selection will be different for each type of density, such as a Poisson density or Bernoulli density; and it will differ depending on the problem.

Now, the new value of Θ is obtained as:

Maximization Step:

$$\Theta^{(i)} = \arg \max_{\Theta} Q(\Theta, \Theta^{i-1}) \quad (3.18)$$

The important difference between the cost function $\mathcal{L}(\Theta)$ and $Q(\Theta, \Theta^{i-1})$ is that unlike $\mathcal{L}(\Theta)$, $Q(\Theta, \Theta^{i-1})$ can be optimized in a closed form. Starting from an initial guess for Θ^{i-1} , the EM algorithm iterates between the *Expectation Step* and the *Maximization Step* until the estimated parameters converge.

3.4.2 HR Process Model Estimation Using the EM Algorithm

Based on the discussions above, the EM approach involves

- (i) Construction of the *complete data likelihood*

- (ii) Deriving the expectation of the complete data likelihood given the observations along with prior estimates of the parameters
- (iii) Maximization of the expectation term with respect to the parameter terms.

In the next three subsections, we elaborate on these three steps.

3.4.3 Complete-Data Likelihood of Θ

The joint density of the complete data (i.e., assuming X_n is observed) is written as

$$p(\mathcal{Z}_n, \mathcal{X}_n | \Theta) = p(x_0) \prod_{k=1}^n p(x_k | x_{k-1}) \prod_{k=1}^n p(z_k | x_k) \quad (3.19)$$

where $\Theta = \{\sigma_v, \sigma_w\}$ and

$$\begin{aligned} p(x_0) &= \frac{1}{\sqrt{2\pi}\sigma_0} \exp \left\{ -\frac{(x_0 - \mu_0)^2}{2\sigma_0^2} \right\} \\ p(x_k | x_{k-1}) &= \frac{1}{\sqrt{2\pi}\sigma_v} \exp \left\{ -\frac{(x_k - \text{F}x_{k-1})^2}{2\sigma_v^2} \right\} \\ p(z_k | x_k) &= \frac{1}{\sqrt{2\pi}\sigma_w} \exp \left\{ -\frac{(z_k - x_k)^2}{2\sigma_w^2} \right\} \end{aligned} \quad (3.20)$$

Now, the complete-data likelihood of Θ can be written as

$$\begin{aligned} -\ln p(\mathcal{X}_n, \mathcal{Y}_n | \Theta) &= c + \ln \sigma_0 + \frac{(x_0 - \mu_0)^2}{2\sigma_0^2} \\ &\quad + n \ln \sigma_v + \sum_{k=1}^n \frac{(x_k - \text{F}x_{k-1})^2}{2\sigma_v^2} \\ &\quad + n \ln \sigma_w + \sum_{k=1}^n \frac{(z_k - x_k)^2}{2\sigma_w^2} \end{aligned} \quad (3.21)$$

where c is a constant.

3.4.4 Expectation

The expectation step is written as

$$\begin{aligned} Q(\boldsymbol{\Theta}, \boldsymbol{\Theta}^{i-1}) &= E \{ \ln p(\mathcal{Z}, \mathcal{X} | \boldsymbol{\Theta}) | \mathcal{Z}, \boldsymbol{\Theta}^{i-1} \} \\ &= E \{ -2 \ln p(\mathcal{X}_n, \mathcal{Y}_n | \boldsymbol{\Theta}) \} \end{aligned} \quad (3.22)$$

which can be shown to be [66, page 343]

$$\begin{aligned} Q(\boldsymbol{\Theta}, \boldsymbol{\Theta}^{i-1}) &= \ln \sigma_0^2 + \frac{1}{\sigma_0^2} ((x_{0|n} - \mu_0)^2 + P_{0|n}) \\ &\quad + n \ln \sigma_v^2 + \frac{1}{\sigma_v^2} (S_{11} - 2S_{10} + S_{00}) \\ &\quad + n \ln \sigma_w^2 + \frac{1}{\sigma_w^2} \left(\sum_{k=1}^n (z_k - x_{k|n})^2 + P_{k|n} \right) \end{aligned} \quad (3.23)$$

where

$$S_{11} = \sum_{k=1}^n (x_{k|n}^2 + P_{k|n}) \quad (3.24)$$

$$S_{10} = \sum_{k=1}^n (x_{k|n} x_{k-1|n} + P_{k|k-1}) \quad (3.25)$$

$$S_{00} = \sum_{k=1}^n (x_{k-1|n}^2 + P_{k-1|n}) \quad (3.26)$$

3.4.5 Maximization

$$\sigma_v^2 = \frac{1}{n} \left(S_{11} - \frac{S_{10}^2}{S_{00}} \right) \quad (3.27)$$

$$\sigma_w^2 = \frac{1}{n} \left(\sum_{k=1}^n (z_k - x_{k|n})^2 + P_{k|n} \right) \quad (3.28)$$

$$x_0 = x_{0|n} \quad (3.29)$$

$$\sigma_0 = P_{0|n} \quad (3.30)$$

and the initial values can be written as (3.29) and (3.30).

Figure 3.13 demonstrates the final algorithm implemented. The raw measurements are passed to the KF as in [2] but the EM algorithm iteratively processes the data and updates a new value for process noise covariance Q and measurement noise covariance R . These new values are passed to the KF for better HR estimation. This approach is significant since Q and R vary from user physiology, body temperature and step cadence, an assumption that doesn't occur in [2]. Therefore, the EM algorithm represents an innovation to the algorithm, processing and assigning updated values regardless of manual tuning for exclusive datasets.

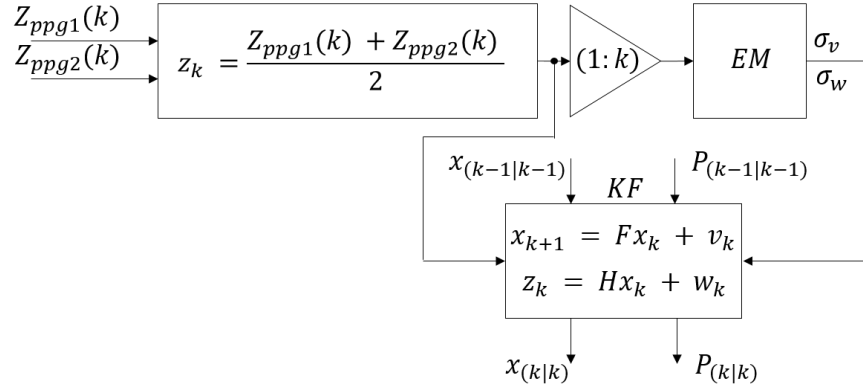


Figure 3.13: Proposed approach with KF from [2] and EM.

3.5 Results

In this section validation of the performance of the proposed method using computer simulations and publicly available data in [1] is performed. The EM algorithm works for the

estimation of parameters σ_v and σ_w for measurements using (3.11). Following the same state model presented in section 3.3 we show that the EM algorithm is capable of estimating process and measurement noise better than user assigned parameters.

3.5.1 Computer Simulation Results

First, the data is simulated for $k = 150$ samples assuming $\sigma_v = 4$ and $\sigma_w = 10$. Then, the EM algorithm summarized in section 3.2 and the simulated data z_k , $k = 1, 2, \dots, 150$, are used to estimate σ_v and σ_w . The EM algorithm used a fixed number of 10 iterations. At the end of 10 iterations, the estimated parameters are obtained as: $\sigma_v = 3.55$ and $\sigma_w = 9.55$. Figure 3.14 shows the simulated data z_k , along with the true value x_k . In addition, the KF estimated values of x_k assuming the true model parameters $\sigma_v = 4$ and $\sigma_w = 10$ are plotted on the same axis. Finally, the KF estimated values of x_k , assuming the EM estimated values of σ_v and σ_w are also plotted on the same axis for comparison.

3.5.2 Real Data Results

In this section we validate the performance of the proposed method using traces publicly available in [1] as mentioned in section 3.2.2. In [2], the algorithm performance relies on a few user tuned parameters for this specific database. Following this approach, the parameters chosen for the KF in [2] are carefully analyzed from experimental data. That means, parameters such as σ_v^2 and σ_w^2 are “hard-wired” for specific datasets, whereas in our approach, the EM algorithm is capable of estimating them.

Figure 3.15 shows the raw HR measurements z_{ppg1} and z_{ppg2} , along with the true value (reference) and comparison between the algorithm proposed by [2] and our proposed method using the EM algorithm.

The HR estimation by [2] follows the reference, while the same happens with our EM

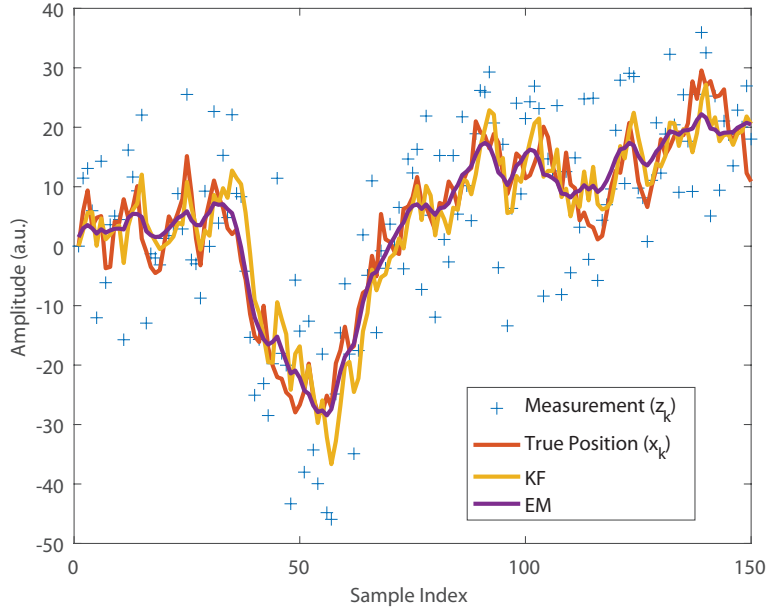


Figure 3.14: Comparison of KF and the EM algorithm for state model in (3.11) with $N = 10$ iterations.

approach. In this particular case, the EM algorithm estimates $\sigma_v = 4.37$ and $\sigma_w = 11.35$, which is very close to the parameter tuned by [2]. Now, assuming that the parameter estimation for σ_v was set incorrectly to this analyzed dataset, such as $\sigma_v = 1$. This means that for the KF performance, the zero mean white Gaussian process noise with covariance $Q = \sigma_v^2$ for a one state system as in 3.3 is set below than the previous known estimated value. This implies that, since the KF from [2] assumes a “hard-wired” value, HR estimations are inconclusive, whereas using the EM algorithm, Q and R are estimated, allowing for a better HR measurement.

Figure 3.18 shows the comparison between [2] and EM algorithm. The assumption is that parameters σ_v and σ_w were changed to $\sigma_v = 1$ and $\sigma_w = 10$. The estimation provided by [2] is dependant on these parameters, while in our algorithm, these parameters are iteratively estimated. In this case, the EM estimates $\sigma_v = 3.28$ and $\sigma_w = 12.36$.

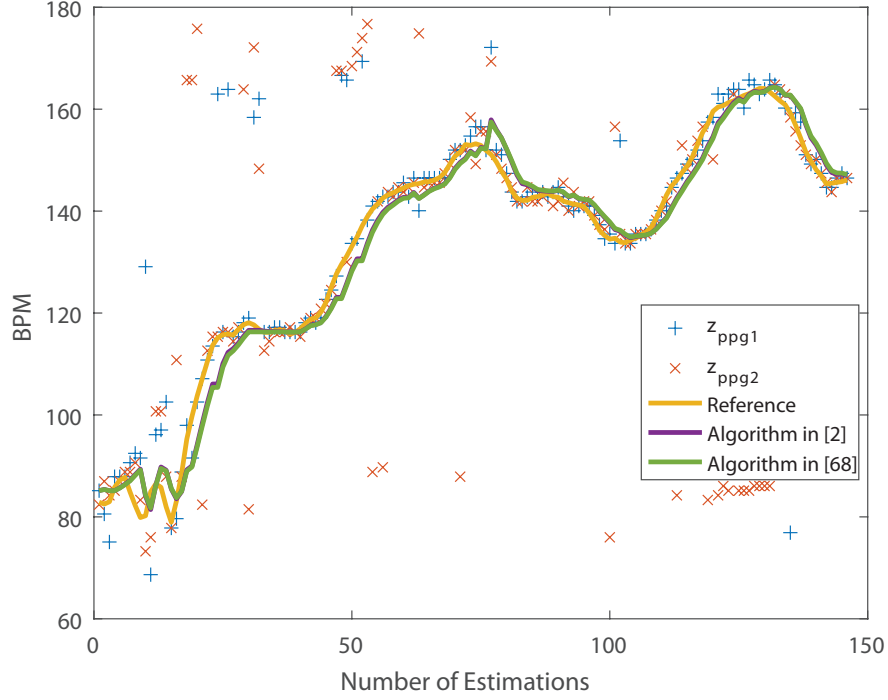


Figure 3.15: Comparison between estimated HR values of [2] with $\sigma_v = 4$ and $\sigma_w = 10$ and the EM algorithm – Dataset #4

Figure 3.21 shows another case of this dependance in [2] for fixed values of σ_v and σ_w . In this case, parameters are set to $\sigma_v = 1$ and $\sigma_w = 1$. Even though those parameters were changed, the EM algorithm still provides better estimates than [2]. In this case, the EM estimates $\sigma_v = 5.74$ and $\sigma_w = 11.34$.

As shown in Figures 3.15, 3.18 and 3.21, the EM algorithm is capable of estimating σ_v and σ_w better than “hard-wired” values as in [2] regardless from the dataset used.

Now, we compare the performance of the proposed method using well known performance metrics such as the average absolute deviation from reference values (E_1) and the average relative deviation (E_2), analyzed for three different cases of process noise Q and measurement noise R as shown in the following table. X_{meas} is denoted as the estimated BPM value and BPM_{ref} the true value of HR available for each dataset. Galli et al. are the performance

values as in [2] and EM-KF is our developed approach. Iteration number was set to $N = 3$, and σ_v estimated.

$$E_1 = \frac{1}{n} \sum_{k=1}^n |X_{meas}(k) - BPM_{ref}(k)| \quad (3.31)$$

$$E_2 = \frac{1}{n} \sum_{k=1}^n \frac{|X_{meas}(k) - BPM_{ref}(k)|}{BPM_{ref}(k)} \quad (3.32)$$

	$\sigma_v = 4, \sigma_w = 10$				$\sigma_v = 1, \sigma_w = 10$				$\sigma_v = 1, \sigma_w = 1$			
	E_1^*	E_2^*	E_1^{**}	E_2^{**}	E_1^*	E_2^*	E_1^{**}	E_2^{**}	E_1^*	E_2^*	E_1^{**}	E_2^{**}
Galli et al.	1.85	1.00	3.18	1.89	6.66	3.40	5.99	2.05	8.73	4.88	11.59	7.05
EM-KF	2.06	1.24	4.56	3.39	6.26	9.33	3.81	1.93	5.70	8.54	10.66	5.60

* represents dataset from training set and ** represents dataset from extra training set [1] .

As shown in the table above, the EM algorithm out-performs [2] when the parameter σ_v is estimated for each dataset. This happens because the physiology, activity level and other characteristics of each individual are different; through EM it is possible to estimate parameters such as σ_v and/or σ_w for an autonomous heart rate tracking providing a more accurate HR measurement. In addition, Figures 3.17 to 3.23 depicts the correlation and Bland-Altman plot of HR in the database. As in [61], the Bland-Altman plot indicates that the largest errors (points outside the limit of agreement area) occur more frequently in the high HR region, around 120 BPM. This implies that the true HR is corrupted by the movement frequency presented while under physical activity. As shown in section 2.3, the frequency of the movement and the HR frequency may overlap causing an incorrect estimation for the HR measurement.

3.6 Conclusions and Discussions

In this chapter, a methodology for HR estimation using PPG sensors is presented. As shown in chapter 2, PPG sensors can provide a reliable HR reading if MA are greatly reduced. Thus, in this chapter, a HR estimation method using PPG sensors is proposed using the optimal Kalman Filter and the EM algorithm. The Expectation and Maximization algorithm is used to estimate certain parameters that may vary from individual. This estimation represents a more refined parameter selection to the KF, which in turn, provides more accurate estimations of HR measurements. The evaluation and comparison of known algorithms such as in [2] is presented, and comparison is made with published work [68]. Even though the dataset publicly available in [1] comprises of a limited set, the EM algorithm out-performs when parameters such as σ_v and σ_w are estimated, rather than tuned. This happens because the activity level and step cadence of each individual is different, and through the EM algorithm those parameters can be estimated independently of the user physiology.

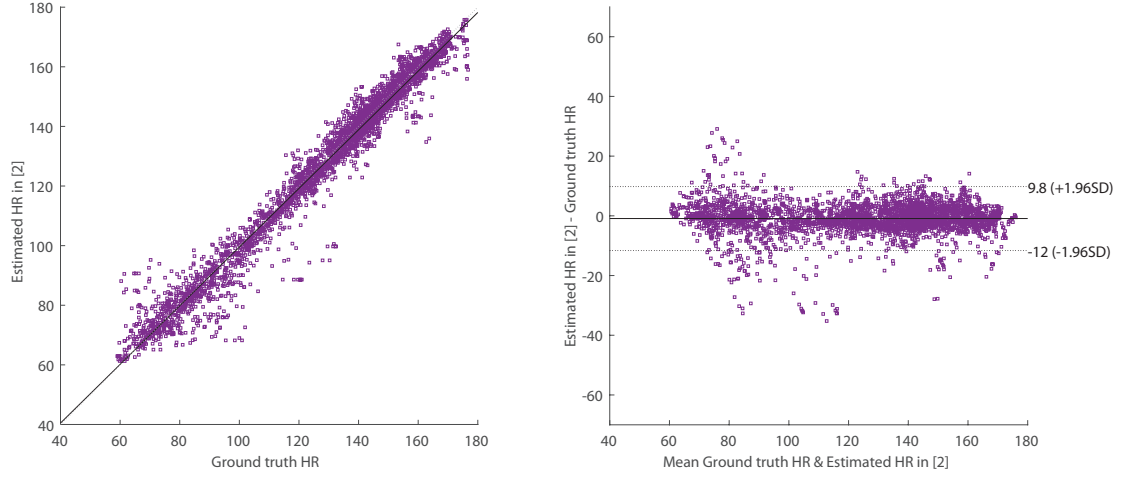


Figure 3.16: Bland Altman plot in [2]

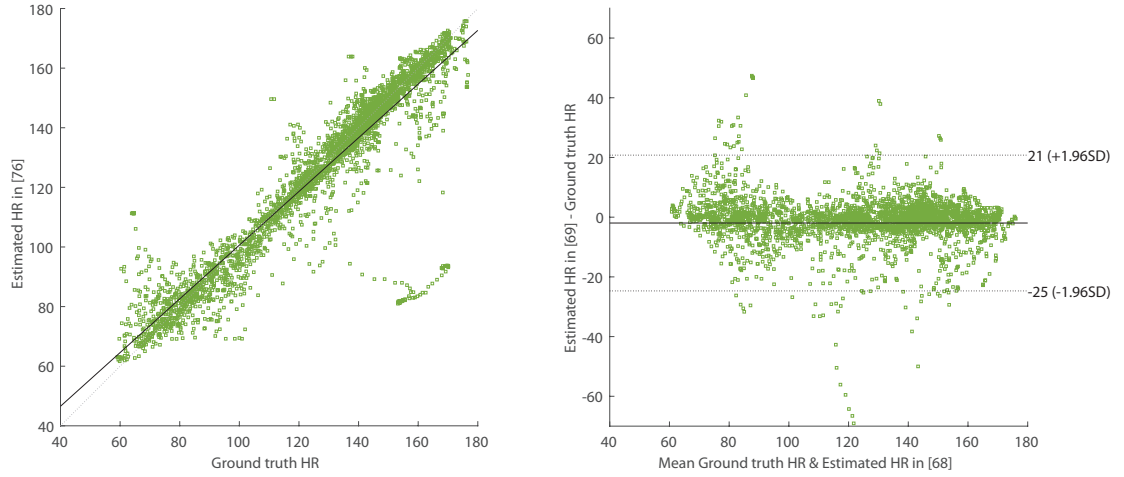


Figure 3.17: Bland Altman plot of the EM algorithm with $\sigma_v = 4$ and $\sigma_w = 10$.

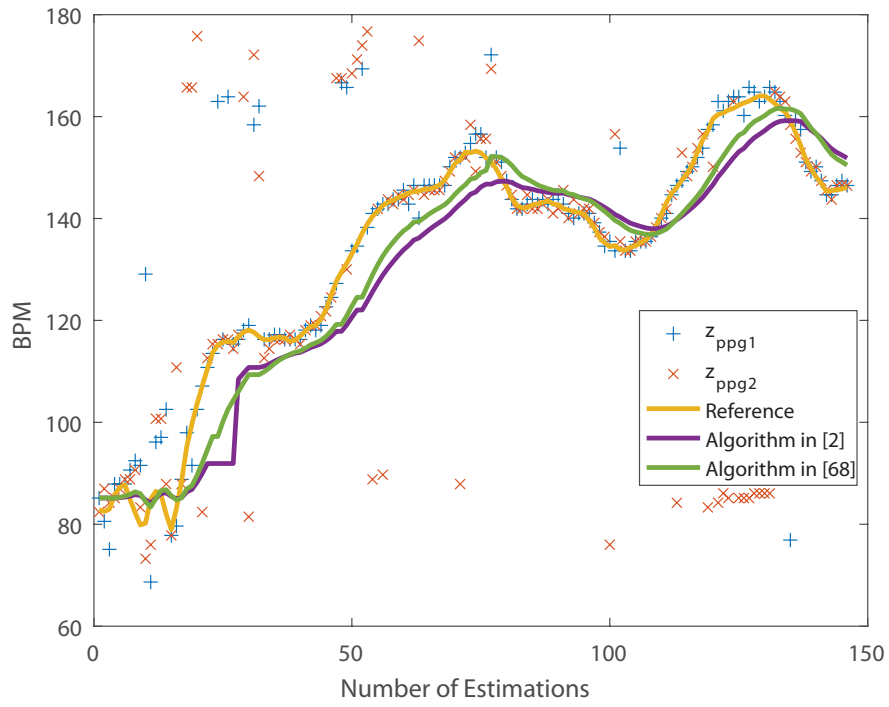


Figure 3.18: Comparison between estimated HR values of [2] with $\sigma_v = 1$ and $\sigma_w = 10$ and the EM algorithm – Dataset #4

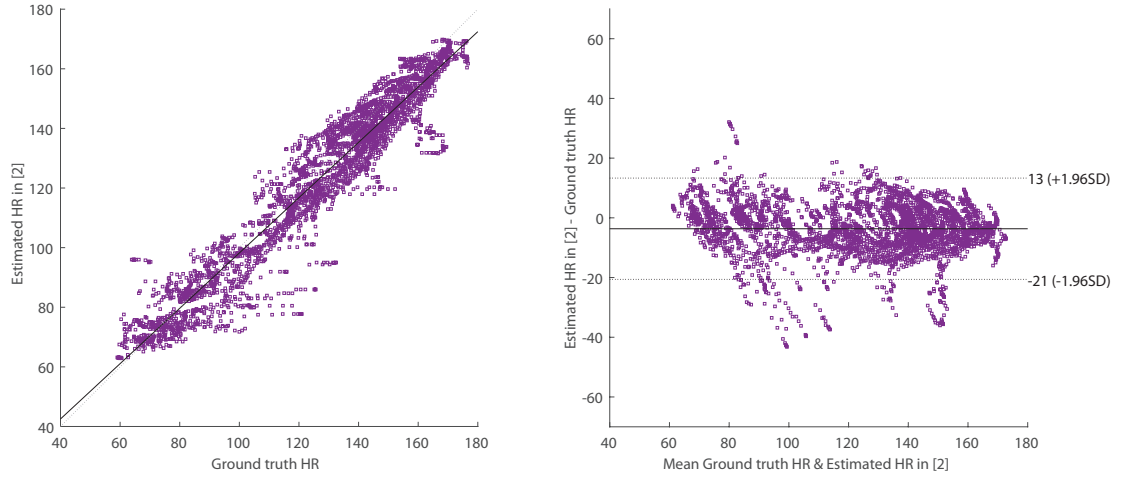


Figure 3.19: Bland Altman plot in [2]

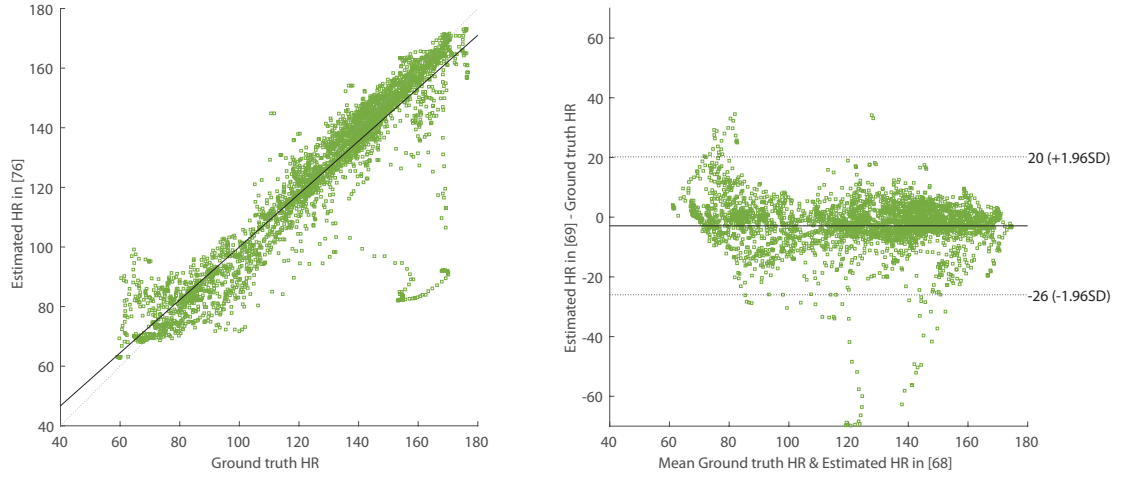


Figure 3.20: Bland Altman plot of the EM algorithm with $\sigma_v = 1$ and $\sigma_w = 10$.

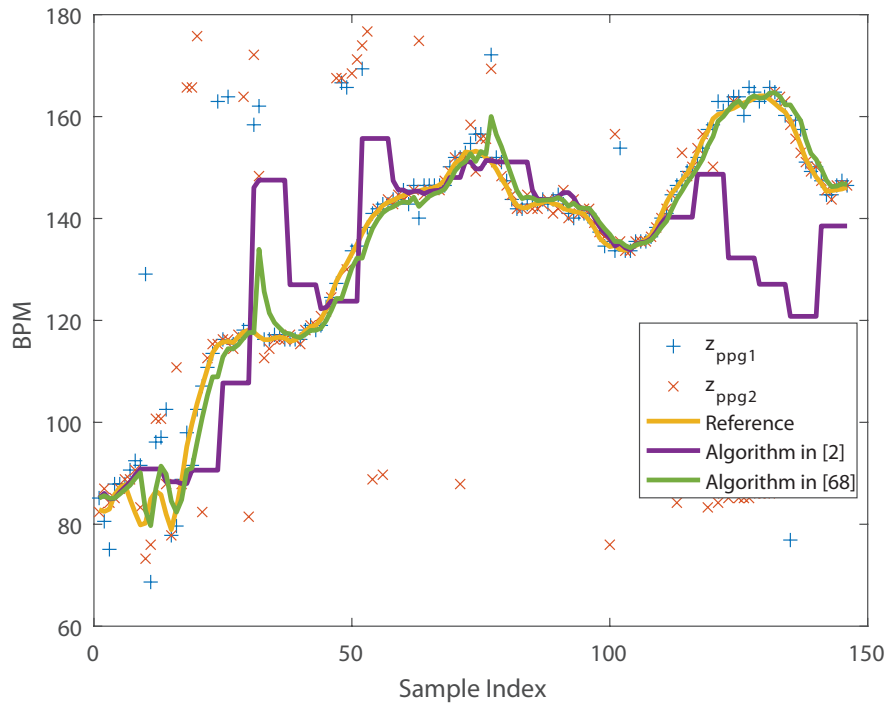


Figure 3.21: Comparison between estimated HR values of [2] with $\sigma_v = 1$ and $\sigma_w = 1$ and the EM algorithm – Dataset #4

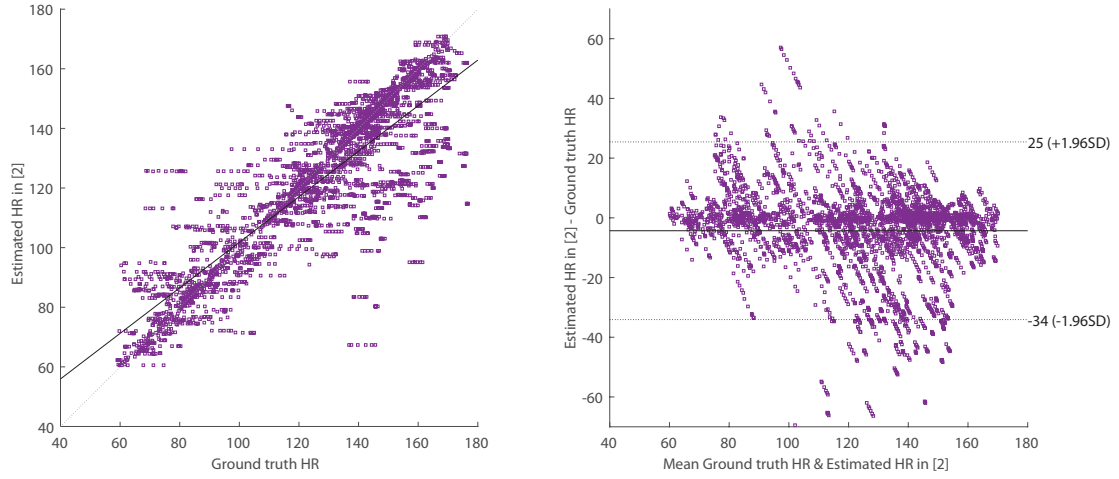


Figure 3.22: Bland Altman plot in [2]

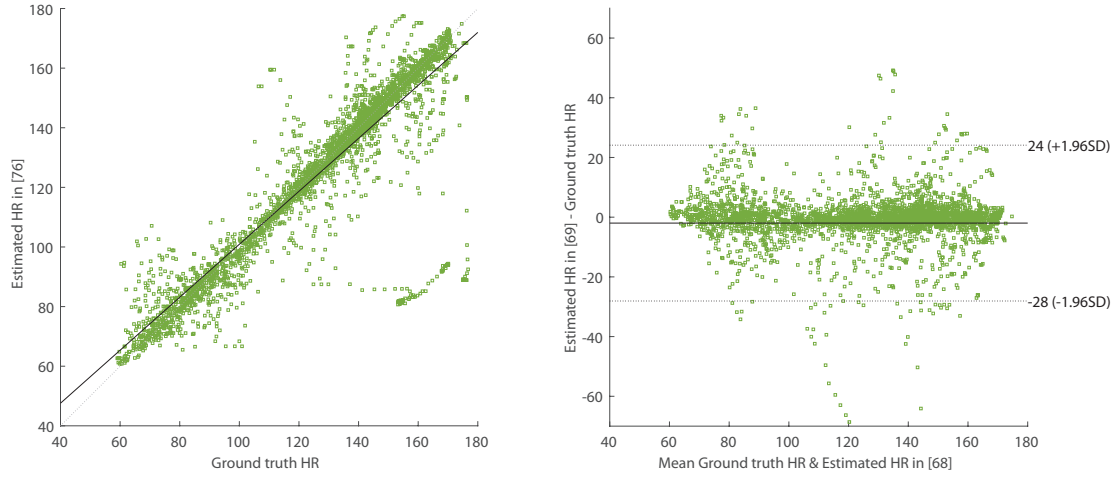


Figure 3.23: Bland Altman plot of the EM algorithm with $\sigma_v = 1$ and $\sigma_w = 1$.

Chapter 4

Fusion Method

Target tracking is a relatively common task for several applications. Most of the time, tracking a target is accomplished by using a range of sensors. The decision process on how to associate trackings belonging to the target is a correlation problem which was examined in [69,70]. “Once the targets are correlated an algorithm is needed to provide a single target track which has less uncertainty than of the individual tracks. This process is often referred to as track fusion” [71]. Thus, in the environment of 2 photoplethysmography sensors, the ability to fuse these two measurements will provide a more accurate HR estimation using the Kalman Filter.

For example, considering the following linear state space model

$$\mathbf{x}(k+1) = \mathbf{F}\mathbf{x}(k) + \mathbf{v}(k) \quad (4.33)$$

$$\mathbf{z}(k) = \mathbf{H}\mathbf{x}(k) + \mathbf{w}(k) \quad (4.34)$$

where

$$\mathbf{F} = \begin{bmatrix} 1 & \Delta T \\ 0 & 1 \end{bmatrix}, \quad \mathbf{H} = \begin{bmatrix} 1 & 0 \end{bmatrix} \quad (4.35)$$

and the process noise $\mathbf{v}(k)$ and measurement noise $\mathbf{w}(k)$ are assumed to be *Gaussian noise* zero mean (vector) and covariance matrices

$$\mathbf{Q} = E \{ \mathbf{v}(k) \mathbf{v}(k)^T \}, \quad \mathbf{R} = E \{ \mathbf{w}(k) \mathbf{w}(k)^T \} \quad (4.36)$$

Given the measurement $\mathbf{z}(k)$, the Kalman filter [72] gives the best estimate of $\mathbf{x}(k)$ as $\hat{\mathbf{x}}(k|k)$ and the associated estimation error covariance $\mathbf{P}(k|k)$.

Now, consider a case where there are two sensors instead of one. In this case, the measurement model 4.33 can be re-written as

$$\mathbf{z}_1(k) = \mathbf{H}\mathbf{x}(k) + \mathbf{w}_1(k) \quad (4.37)$$

$$\mathbf{z}_2(k) = \mathbf{H}\mathbf{x}(k) + \mathbf{w}_2(k) \quad (4.38)$$

where

$$\mathbf{R}_1 = E \{ \mathbf{w}_1(k) \mathbf{w}_1(k)^T \}, \quad \mathbf{R}_2 = E \{ \mathbf{w}_2(k) \mathbf{w}_2(k)^T \} \quad (4.39)$$

The problem is then how to effectively *fuse* the data from two sensors in order to get the best estimate of the true state $\mathbf{x}(k)$.

The above problem has been addressed in the literature and two possible fusion approaches known as *state-vector fusion* and *measurement fusion* were developed. Several other types of sensor fusion approaches are found in the literature; some of them were intuitive

approaches that might eventually cost in terms of performance. Thus, in the next section, both fusion approaches are discussed and analyzed for choosing the best fusing method for the proposed HR estimation method.

4.1 State Vector Fusion

Here, two Kalman filters [72] run in parallel and compute $\hat{\mathbf{x}}_1(k|k)$, $\mathbf{P}_1(k|k)$ and $\hat{\mathbf{x}}_2(k|k)$, $\mathbf{P}_2(k|k)$. The fusion method can be accomplished by fusing the filtered state vectors ($\hat{\mathbf{x}}_1(k|k)$ and $\hat{\mathbf{x}}_2(k|k)$) into a new estimate of the state vector [73]. The new estimate of the state vector $\hat{\mathbf{x}}(k|k)$ is given by the following fusion equation as in [71].

$$\hat{\mathbf{x}}(k|k) = \hat{\mathbf{x}}_1(k|k) + \mathbf{P}_{xz}\mathbf{P}_{zz}^{-1}(\hat{\mathbf{x}}_2(k|k) - \hat{\mathbf{x}}_1(k|k)) \quad (4.40)$$

$$\mathbf{P}_{xz} = \mathbf{P}_1(k|k) - \mathbf{P}_{12}(k|k) \quad (4.41)$$

$$\mathbf{P}_{zz} = \mathbf{P}_1(k|k) + \mathbf{P}_2(k|k) - \mathbf{P}_{12}(k|k) - \mathbf{P}_{21}(k|k) \quad (4.42)$$

Where $\hat{\mathbf{x}}_1(k|k)$ is the first filtered state vector, $\mathbf{P}_1(k|k)$ is the covariance matrix for $\hat{\mathbf{x}}_1(k|k)$, and $\mathbf{P}_{12}(k|k)$ is the cross covariance matrix between $\hat{\mathbf{x}}_1(k|k)$ and $\hat{\mathbf{x}}_2(k|k)$. The cross covariance matrix is given by the recursive equation:

$$\begin{aligned} \mathbf{P}_{12}(k|k) &= (\mathbf{I} - \mathbf{K}_1(k)\mathbf{H}_1(k))\mathbf{F}\mathbf{P}_{12}(k-1|k-1)\mathbf{F}^T \\ &\times (\mathbf{I} - \mathbf{K}_2(k)\mathbf{H}_2)^T + (\mathbf{I} - \mathbf{K}_1(k)\mathbf{H}_1)\mathbf{Q}(\mathbf{I} - \mathbf{K}_2(k)\mathbf{H}_2)^T \end{aligned} \quad (4.43)$$

where $\mathbf{K}_1(k)$ is the Kalman Filter gain matrix for sensor 1 at time k . The covariance matrix of the fused estimate is then given by:

$$\begin{aligned} \mathbf{P}(k|k) = & \mathbf{P}_1(k|k) - (\mathbf{P}_1(k|k) - \mathbf{P}_{12}(k|k))(\mathbf{P}_1(k|k) \\ & + \mathbf{P}_2(k|k) - \mathbf{P}_{12}(k|k) - \mathbf{P}_{21}(k|k))^{-1} \\ & \times (\mathbf{P}_1(k|k) - \mathbf{P}_{21}(k|k)) \end{aligned} \quad (4.44)$$

4.2 Measurement Fusion

The second approach for fusion is to use measurements from both sensors and then track those measurements to obtain an estimate of the state vector [71]. The measurement noise is independent for both sensors and the equation for fusing both measurements can be accomplished in recursive form by:

$$\bar{\mathbf{z}}(k) = \mathbf{z}_1(k) + \mathbf{R}_1(k)(\mathbf{R}_1(k) + \mathbf{R}_2(k))^{-1}(\mathbf{z}_2(k) - \mathbf{z}_1(k)) \quad (4.45)$$

where $\mathbf{R}_1(k)$ is the covariance matrix of the measurement vector $\mathbf{z}_1(k)$. The filtered measurement has a covariance matrix given by:

$$\bar{\mathbf{R}}(k) = [(\mathbf{R}_1(k))^{-1} + (\mathbf{R}_2(k))^{-1}]^{-1} \quad (4.46)$$

These filtered measurements can be tracked to obtain the estimate of the state vector $\hat{\mathbf{x}}(k|k)$.

4.3 Performance Analysis

To illustrate the improvement achieved using the measurement fusion over the state vector fusion method, an example is performed as in [71].

$$\mathbf{x}(k+1) = \begin{bmatrix} 1 & 1 \\ 0 & 1 \end{bmatrix} x(k) + \begin{bmatrix} 0.5 \\ 1 \end{bmatrix} v(k) \quad (4.47)$$

with sampling time $T = 1$ and noise variance q . The measurement equation of the two sensors is

$$\mathbf{z}(k) = \begin{bmatrix} 1 & 0 \end{bmatrix} x(k) + v(k) \quad (4.48)$$

where the measurement noise is independent with variance $r = 1$. The steady state cross covariance matrix \mathbf{P}_{12} can be calculated by substituting the steady state gain into 4.43, letting $\mathbf{P}_{12}(k|k) = \mathbf{P}_{12}(k-1|k-1)$ and solving for the components of the cross covariance matrix as in [71]. Figure 4.24a) represents the reduction in the components of $\mathbf{P}(k|k)$ where

$$\mathbf{P}(k|k) = \begin{bmatrix} p1 & p2 \\ p2 & p3 \end{bmatrix} \quad (4.49)$$

for the two sensor fusion over the single sensor case for a range of process noise q . Now, applying a one state model such as 3.10 and comparing both fusion methods with [2]:

The method chosen by [2], as seen by the cross covariance matrix comparison in Figure 4.24b), it is not optimal for fusing both measurements of PPG sensors for estimation using the Kalman Filter. Thus, in the proposed approach, another innovation is the use of the measurement fusion method for fusing both raw PPG measurements z_{ppg_1} and z_{ppg_2} .

4.4 Final Proposed Algorithm

It was demonstrated in chapter 3 the use of the EM algorithm for estimating variance noises independently of user physiology. This method provided a better estimation of noise parameters for the Kalman filter and its application was demonstrated as well. In chapter 4 it was shown that the fusion method previously used would hamper the covariance matrix, prompting an unreliable HR estimation by the Kalman filter. Thus, it was proved that the best fusion method for tracking a target, in this case, the HR frequency, with two measurements, z_{ppg_1} and z_{ppg_2} is by using the measurement fusion approach. As such, the final HR estimation algorithm comprises these two innovations, providing a more accurate HR estimation measurement. The final flowchart and algorithm implementation is shown in Figure 4.25 and Figure 4.26.

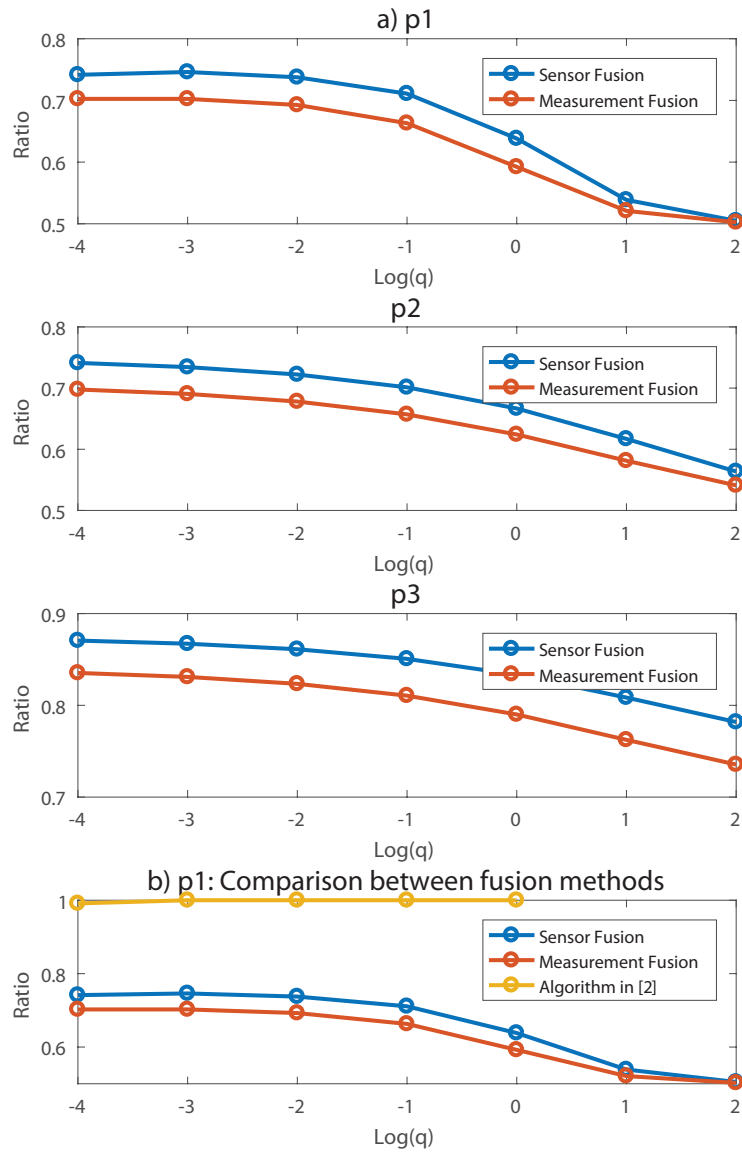


Figure 4.24: Ratio of components of covariance matrix for two sensor fused estimate and algorithm proposed in [2].

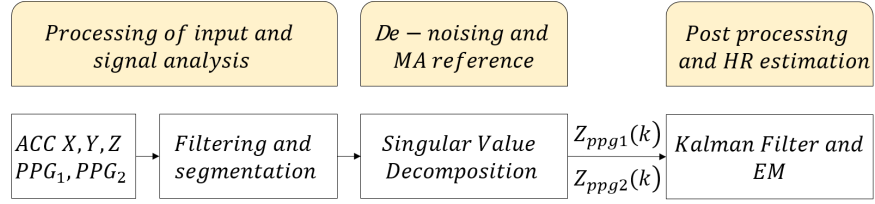


Figure 4.25: Flowchart of final HR estimation system.

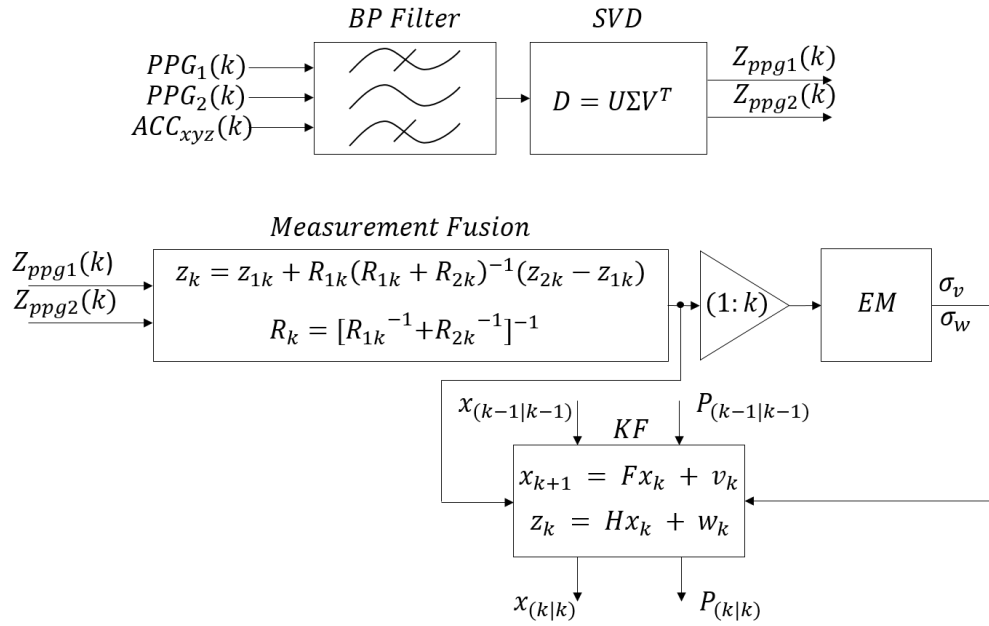


Figure 4.26: Final Algorithm proposed for HR estimation.

Chapter 5

Synthetic signals

During intense physical exercise, the cardiovascular system increases the delivery of blood and oxygen to muscles and the metabolic activity increases, which intensifies HR and volume stroke [74]. Obtaining a model that describes the cardiovascular system during such intensive exercise using photoplethysmography sensors, would improve the understanding of exercise physiology and support the extensive use of wearable devices for physical and medical applications. Understanding the HR response after or prior to exercise may be also beneficial to prevent cardiovascular mortality [75]. The core idea of this work is to be able to accurately produce synthesized signals for HR algorithm evaluation using photoplethysmography (PPG) sensors. This comes from the fact that usually, it is very difficult to have access to real data since the data is restricted to the user and/or the collector or demands proprietary hardware. Moreover, sensitivity data is bounded by copyright and justification is mandatory of its use, share, and analysis. Thus, the ability to produce synthesized data provides the researcher with an easier way for algorithm evaluation. Data comprising of PPG and accelerometers are usually captured when the user/patient is performing common physical activities, such as resting, walking, running, or even more complex activities as

boxing and arm movements. This scenario displays a complex task since there is no control over the movements and repetitions. The possibility of standardizing the physical activity for research purposes enables a deeper analysis of the signal that is being acquired. For this reason, a simulation tool is of great innovation, providing a precise simulation environment for the researcher/developer for evaluation of HR algorithm estimators with control of the activity pattern, intended for wearable devices.

5.1 Physical Activity model (PAM)

The present study focuses on activities that are common for the user while performing the repetitive activity while on a treadmill. Assuming that a resting period is included, walking, jogging and running are the most common activities performed while in this environment. Other activities may be performed for physical expenditure for example, but since they are complex movements and will demand more complex models for accurate sensoring synthesized implementation, they are disregarded in this study. According to the activity that is being performed, the user pattern is formulated as follows, and several assumptions are considered:

The model is produced by three main activities named as *resting*, *walking* and *running*. Each activity that is created is performed by a certain amount of time and each block of activity has the following parameters:

- Frequency of HR f_{HR} and noise related σ_{HR}
- Frequency related to the movement of the user f_{mov} and noise related σ_{mov}
- PPG synthesized signals ppg_1 and ppg_2
- Tri-dimensional accelerometer synthesized signals acc_x , acc_y , acc_z

- Speed of the treadmill v_t

The Physical Activity Model (PAM), is produced regarding the speed and movement the user is submitted in the model. For example: At resting position, the speed v_t is assumed zero; if walking, the speed v_t is within a set speed range and at running v_t is set to a value higher than these limits. This assumption is needed since the model is bounded by the speed of v_t being used in the running activity. Also, the speed pattern is a step function, that is, after a block of activity is finished, the speed is set to the value of the next block.

The Physical Activity Model PAM is characterized by:

$$PAM = ([Activity\ Level, Time\ Duration]) \quad (5.50)$$

Figure 5.27 illustrates a case where the pattern is set to various running activities level and time durations, where: $rt = resting$, $w = walking$ and $ru = running$.

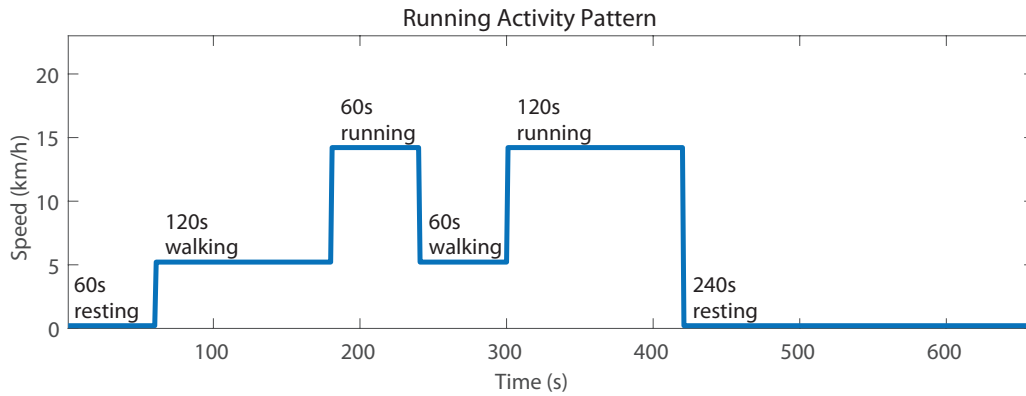


Figure 5.27: Illustration of PAM for various running activities level and time durations.

For example, the implementation of the example model (5.51) can be described by the user starting the activity at a resting position for a duration of 60 seconds, then changing to the walking activity for 120 seconds and so on. As shown in Figure 5.27, the speed v_t

assigns the model related to the activity that is being performed. Also, the speed of v_t is taken as constant for each block of activity.

$$PAM = ([rt, 60], [w, 120], [ru, 60], [w, 60], [ru, 120], [rt, 240]) \quad (5.51)$$

Moreover, assumptions are taken for a better model representation. Maximum and/or minimum values for HR, f_{HR} , σ_{HR} , f_{mov} , σ_{mov} and τ are assumed as parameters that depend on the physical activity. Thus, assumptions are assigned for each activity model for correct simulation.

The assumptions are presented in Table 5.6.

Parameters	Resting	Walking	Running
HR (BPM)	72	108	156
f_{HR} (Hz)	1.2	1.8	2.6
σ_{HR} (Hz)	0.2	2.0	3.0
$f_{mov_{max}}$ (Hz)	1.0	2.3	2.8
σ_{mov} (Hz)	$\simeq 0$	2.0	3.0
τ	5	5	5

Table 5.6: Assumptions for each activity level

5.1.1 Heart Rate Pattern

Following the same idea of the *PAM* model, the synthesized HR pattern (*HRP*) is formed. However, the pattern is accomplished via an exponential approach as in [74]. Several HR models are available in the literature, varying from linear to nonlinear models. The proposed model follows a novel representation of charging and discharging effect, such as a capacitor. Since HR has a slow recovery time, the exponential response seems to be a reasonable response curve to this model. A time constant (τ) related to the rate of charging and

discharging such as in the capacitor is also used. This approach allows the modeling of HR with an exponential perspective resembling the models exposed by [74]. This configuration provides a varying curve of HR frequencies that can be simulated in the HR model. Since the HR frequency changes during physical activity, the HR model frequency will as well, providing a more realistic response to the simulation. Thus, the HR model has the characteristic curve response of the capacitor voltage while charging and discharging. This is set and accomplished by the next activity level change. By increasing the activity level, the HR response is modeled as a positive exponential curve as the effect of the charging phase of a capacitor. On the other hand, when the activity level decreases, the HR response is modeled as a decreasing exponential curve, as the effect of the discharging phase of a capacitor. The HR model is characterized by

$$HR_k = HR_{k-1} + \Delta f_{HR} - \Delta f_{HR} e^{-m/\tau} + \sigma_{HR}, \quad (5.52)$$

$$m = \{0, \dots, n - 1\}$$

where:

HR_k is the current HR,

HR_{k-1} is the previous HR,

$\Delta f_{HR} = f_{HR_k} - f_{HR_{k-1}}$ is the difference of current HR frequency and previous HR frequency,

n is the time span related to the duration of the activity,

τ is the time constant that characterizes the rate of charging and discharging when the activity level changes,

σ_{HR} corresponds to the noise according to the activity level.

The exponential feature of the *HRP* provides a range of HR frequencies that vary over time. These frequencies are then calculated by dividing the value of HR to obtain the cardiac

frequency measured in beats per minute (BPM). Also, the noise σ_{HR} is added as a form of compensation for the Heart Rate Variability (HRV) for the synthesized signal.

Figure 5.28 provides an example of the *HRP* model. For the example model (5.51), the HR changes according to the activity of movement that is being performed. Also, the HR value is modeled as an exponential curve, providing a more realistic response for HR recovery that depends on the physical activity. The parameter τ can vary for different activity changes, providing a faster or slower HR recovery rate for the simulated signal.

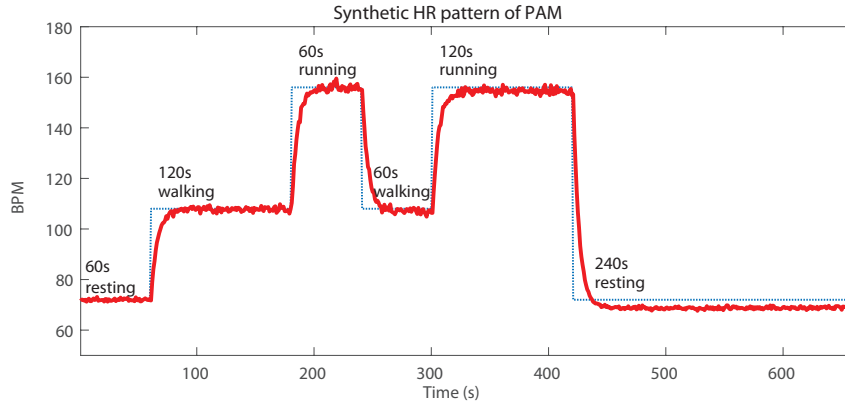


Figure 5.28: Illustration of HR pattern for various running activities level and time durations. For this particular case the pattern was obtained from example model as in (5.51).

5.2 Synthetic Signal Simulation

In this section, simulated signals are decomposed in their principal characteristics allowing a very accurate resemblance to their real world response. Here synthesized signals and key features extraction for simulation of photoplethysmographic sensors, a tri-axial accelerometer and a heart rate response driven by the user activity is detailed.

5.2.1 Synthetic PPG

The PPG signal then was modeled as in [76]. A periodic signal having a fundamental frequency f_{HR} that corresponds to the HR beat frequency, together with second and third harmonic components. The amplitudes of the fundamental and its harmonics are given by A, B, and C respectively. Also, the phase difference is presented between its components, given by θ_2 and θ_3 , while the initial phase is given by θ_1 . The set of parameters, together with its DC component characterized by D, can be used to describe the signal:

$$\begin{aligned}
 PPG(n) = & A \cos(2\pi f_{HR}n + \theta_1) \\
 & + B \cos(4\pi f_{HR}n + \theta_2 + 2\theta_1) \\
 & + C \cos(6\pi f_{HR}n + \theta_3 + 3\theta_1) + D + v(n)
 \end{aligned} \tag{5.53}$$

where:

A, B and C are amplitudes of fundamental and harmonics,

f_{HR} is the current HR frequency,

θ_1 , θ_2 and θ_3 are the phase difference between the fundamental and harmonic components,

D is the DC value of the PPG signal,

($n_i \leq n < N$) and $v(n)$ represents white Gaussian noise,

N is the number of observed samples and n_i represents the last iterative value of the previous cosine sequence; this is done in order to maintain a smooth pattern for the the signal once the frequency related to movement is changed.

Figure 5.29 represents both time domain and frequency domain characteristics of the synthetic PPG signal. On the left side, the synthetic PPG signal resembles the characteristic PPG wave with both two phases implemented. Also, the dicrotic notch can be seen for different physical activities. On the right side, the periodogram of each signal for each

physical activity is shown. The main frequency of each plot confirms the assumptions made in Table 5.6. The signal is considered “clean” since the movement interference is not being exploited at this moment. The movement that will be modeled as the accelerometer signal, will be explained in Section 5.2.2.

In addition, in order to account for different activity pace levels, a *random walk* function (RW) is implemented in the PPG pattern signal.

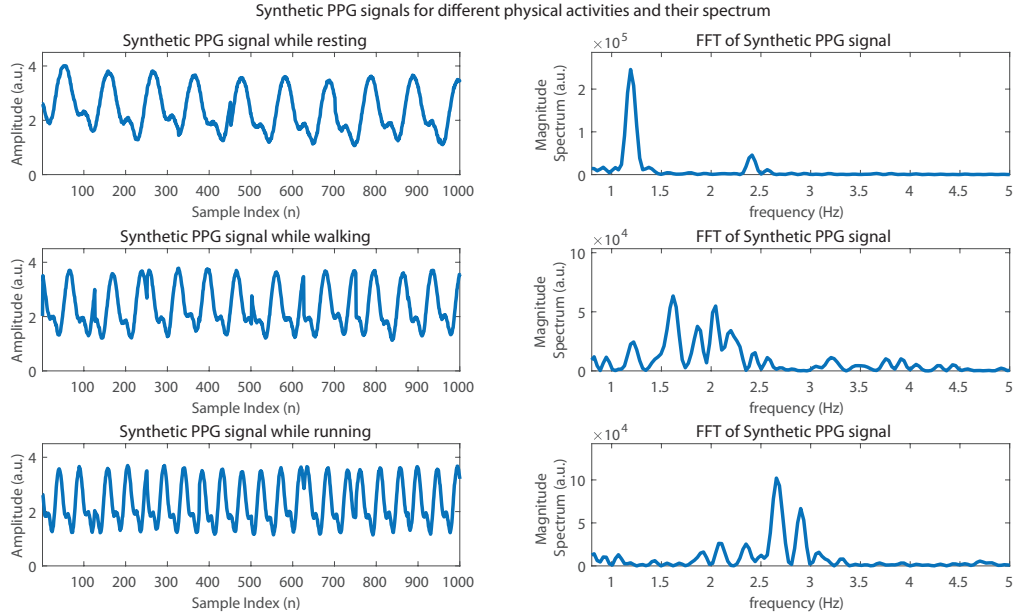


Figure 5.29: Synthesized PPG signal for different physical activities.

5.2.2 Synthetic tri-axil accelerometer

Accelerometers are sensors that detect a force that is directed in the opposite direction from the acceleration vector. This force is called Inertial Force, that means, accelerometers measure acceleration indirectly through a force that is applied to one of its planes [77]. For simplicity and assumption of movement, the accelerometer signal will be simulated, following the same principle as the PPG waveform, with a specific constrain that when there is no

movement, the frequency of movement is almost null, providing a constant signal while the user is in the resting position. Also, the assumption here is that the accelerometer is being used in a wearable device, with its z component normal to the wrist, assigning a value of $-1g$ (gravitational force), being x and y coordinates a constant value of $0g$. While these are the constraints due to rest, once in movement, the accelerometer signal simulates a specific frequency related to movement (which was assigned based on real data) for each individual axis as well a phase difference that occurs between each axis while in movement.

The frequency related to the movement is assigned following the same idea as in the model in (5.52). Here, the maximum movement frequency $f_{mov_{max}}$ is taking for limiting the exponential frequency curve for the movement pattern. The movement pattern can then be formulated as:

$$\begin{aligned} f_{mov_k} &= f_{mov_{k-1}} + \Delta f_{mov} - \Delta f_{mov} e^{-m/\tau} + \sigma_{mov}, \\ m &= \{0, \dots, n-1\} \end{aligned} \tag{5.54}$$

where:

f_{mov_k} is the current movement frequency,

$f_{mov_{k-1}}$ is the previous movement frequency,

$\Delta f_{mov} = f_{acc_k} - f_{acc_{k-1}}$ is the difference of current ACC frequency and previous ACC frequency,

n is the time span related to the duration of the activity,

τ is the time constant that characterizes the rate of charging and discharging when the activity level changes,

σ_{mov} corresponds to the noise according to the activity level.

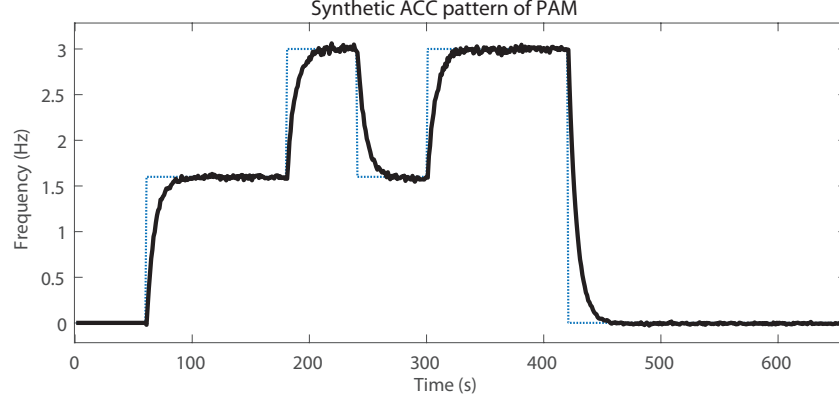


Figure 5.30: Illustration of ACC pattern for various running activities level and time durations. For this particular case the pattern was obtained from example model as in (5.51).

With the movement pattern implementantion, the movement frequency is passed on to the ACC model, in order to create a tri-axial accelerometer signal corresponding to the moment frequency. The ACC signal can be formulated as:

$$\begin{aligned}
 Acc_{axis} = & A_{axis} \cos(2\pi f_{axis} n + \theta_{axis}) \\
 & + a_{axis} v(n) + \frac{A_{axis}}{h} \cos(4\pi f_{axis} n + \theta_{axis})
 \end{aligned} \tag{5.55}$$

where: A_{axis} is the amplitude for each axis,

f_{axis} is the current accelerometer frequency related to the activity,

θ_{axis} is the phase difference between adjacent axis,

a_{axis} is the amplitude of noise related to the activity,

($n \leq n < f_s$), $v(n)$ represents white Gaussian noise.

Figure 5.31 represents both time domain and frequency domain characteristics of the synthetic ACC signal. On the left side, the synthetic ACC signal resembles the characteristic response of a tri-axial accelerometer. Components x , y , z and its vector magnitude (VM) are

presented and $VM = \sqrt[2]{x^2 + y^2 + z^2}$. On the right side, the periodogram of each signal for each physical activity is shown. The main frequency of each plot confirms the assumptions made in Table 5.6. The movement is modeled by the accelerometer data and the combination of signals is represented by VM. This vector is taken and added to the PPG signal data in order to fuse the activity related to movement and with the synthesized PPG signal. The final PPG signal can be expressed as the noiseless PPG signal added to the VM in the frequency domain:

$$PPG_{synt} = PPG + VM \quad (5.56)$$

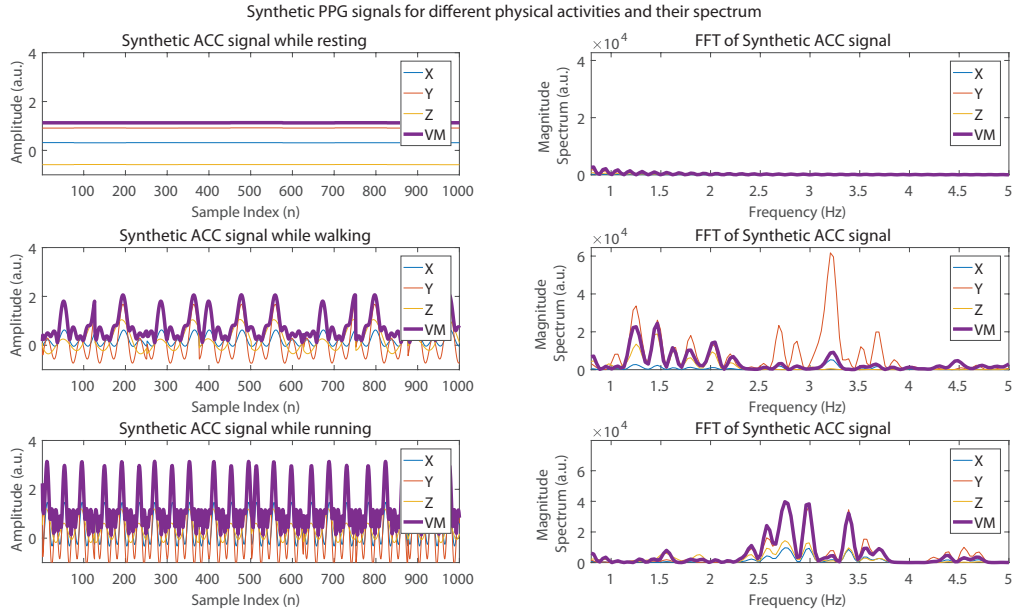


Figure 5.31: Synthesized ACC signal for different physical activities. X, Y and Z corresponds to signal of each individual axis and VM is the vector magnitude.

Figure 5.32 represents the final synthesized PPG signal, which comprehends the HR data combined with the activity of the movement. As can be seen, when the level of activity increases, the spectrum of the PPG signal overlaps the ACC signal. This happens since the

frequency of movement falls within the same range as the HR frequency. This assumption allows us to model the movement related to the activity level and the simulated HR signal providing an accurate simulator model for PPG sensors during physical activities as well an environment to simulate and evaluate HR estimation methods for wearable devices.

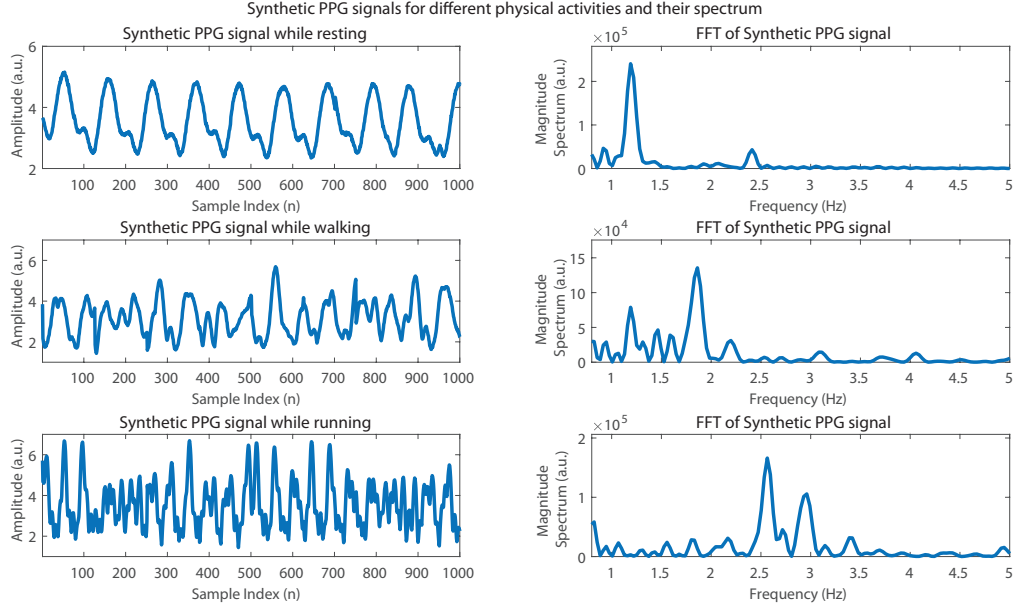


Figure 5.32: Synthesized PPG signal for different physical activities related to the movement that is being performed. There is a spectrum overlap of clean PPG signal as in Figure 5.29 and ACC signal in Figure 5.31, which difficults the correct estimation of HR using PPG sensors.

5.2.3 EM Approach

In previous work [68] the EM algorithm was used to estimate the noise variances, allowing an autonomous HR estimation independently of the user physiology. However, this estimation was performed for each individual dataset but was composed of the entire data sample. In this present work, this approach is redefined by 2 different methods: EM using batch and EM using a trigger. The previous approach [68] utilizes a batch of data for the noise variance

estimation. This means that there is a delay and memory consumption for applications “on the fly” with this method. On the other hand, this simulation tool provides control regarding the activity change. This means that it’s possible to trigger the EM algorithm when the activity change happens. This is important since once the synthesized HR steadies, the noise variances do not vary, allowing a refined EM estimation of these parameters. This, in contrast, resembles in a more accurate estimation of σ_v and σ_w by the EM algorithm, allowing a more accurate HR estimation by the present method.

5.3 PAM Evaluation

5.3.1 Linear Model

The model provides a very realistic approximation to the ensemble of PPG and ACC signals when performing various activities with the use of wearable devices. Due to this fact, the model represents an evaluation method that can be applied in different scenarios for HR optimization of known HR estimators. In this section, several well-known HR estimators are evaluated and reproduced using the proposed PAM simulation tool. First, for signal evaluation of synthesized signals for each photoplethysmography sensor and the tri-axial accelerometer, both PPG and accelerometer models are taken as linear models. That means that the frequency related to HR f_{HR} and movement f_{mov} do not follow the exponential model, but a linear model for simplicity. This indicates that both signals do not vary their assumed frequency within the activity block range. That being the case, the evaluation of 5 algorithms are presented. Assigning now a model of:

$$PAM = ([rt, 30], [w, 60], [ru, 60], [w, 60], [ru, 60], [rt, 30]) \quad (5.57)$$

the output of synthesized signals are presented in Figure 5.34. Since the frequency is linear, it's expected to have a very clean signal for both PPG and ACC signals. This implies that known algorithms for HR estimation would track the ground truth value of HR very accurately.

For model simulation comparison, the same pattern as in the publicly available database [1] is assigned. Figure 5.36 shows the comparison of known algorithms in the literature for HR estimation using PPG sensors. As seen, the ground truth is being tracked by most of algorithms, representing that while in the assumption of constant HR frequency values f_{HR} and movement f_{mov} , represented by the accelerometer signal, are well distinguished and can easily be interpreted by the algorithms for an accurate HR estimation. For algorithm evaluation, a set of performance metrics such as the average absolute deviation from reference values (E_1) and the average relative deviation (E_2) are analyzed. X_{meas} is denoted as the estimated BPM value and BPM_{ref} the ground truth value.

$$E_1 = \frac{1}{n} \sum_{k=1}^n |X_{meas}(k) - BPM_{ref}(k)| \quad (5.58)$$

$$E_2 = \frac{1}{n} \sum_{k=1}^n \frac{|X_{meas}(k) - BPM_{ref}(k)|}{BPM_{ref}(k)} \quad (5.59)$$

Figure 5.36 represents the comparison between known algorithms in the literature with the implementation of *PAM* using the linear model. As expected, since there is not much interference of HR estimation through the use of PPG signals z_{ppg1} and z_{ppg2} , the estimation is very accurate compared to the ground true value *HR GT*. Performance metrics are presented in Table 5.7.

Method	[61]	[2]	[68]	B	T	PA	[14]
E_1	12.86	11.81	10.68	4.48	4.51	2.04	35.82
E_2	22.25	19.75	19.75	11.21	11.19	5.59	26.48

Table 5.7: Metrics comparison for different HR estimation methods with a linear PAM model. B = EM Batch, T = EM Trigger, PA = Proposed Algorithm.

5.3.2 Exponential Model

Now, evaluation of proposed simulation tool using the exponential model is presented. This gives a more realistic response for HR and consequently, this makes it difficult for the algorithms to estimate accurate HR measurements using PPG sensors. Assigning now a model:

$$PAM = ([w, 60], [ru, 120], [rt, 30], [w, 120], [rt, 30], [ru, 60], [w, 120], [rt, 30]) \quad (5.60)$$

Figure 5.35 represents the simulated model for PAM following example model (5.60). The simulated HR response follows the exponential model as explained in section 5.1.1. The exponential response is modulated by the movement and its duration; since the period for resting is set in this example with 30 s duration, the exponential curve is limited to this time range. On the other side, when the activity duration increases, HR is modulated only by its own HRV. Estimation in this environment becomes very challenging comparing to PPG signal values.

Figure 5.37 shows the evaluation of known HR estimation methods using the Exponential model of PAM. Since now the model is more realistic, PPG synthetic frequency estimations do not provide a clean raw signal of z_{ppg1} and z_{ppg2} for estimation stage. These raw measurements are corrupted by severe MA and their separation using SVD is not very accurate. Moreover, the step cadence and HRV that varies with the model makes it even more difficult to estimate correct HR measurements. Even though the environment produces very noisy estimates, the proposed algorithm still converges faster and more accurate than published

algorithms. Performance metrics are presented in Table 5.8.

Method	[61]	[2]	[68]	B	T	PA
E_1	17.73	12.03	8.90	7.82	7.23	6.49
E_2	15.17	8.71	8.71	7.01	5.60	4.78

Table 5.8: Metrics comparison for different HR estimation methods with an exponential PAM model. B = EM Batch, T = EM Trigger, PA = Proposed Algorithm.

In addition, Figure 5.33 demonstrates when the EM algorithm is being triggered, and estimated for σ_v and σ_w . As can be seen, once there is a steady period of activity, both Q and R converge for a steady value. This implies that since there is not much noise in the environment, the noise variances converge. Here, it's needed to say that the triggered event happens since it's known when the activity changes. Finally, it is shown that the PAM model, independently of Linear and Exponential achieves expected simulated parameters for algorithm evaluation. As shown in Figure 5.36 using PAM Linear model, majority of published HR estimation methods can track true HR when the signal is not corrupted by MA and the simulated HR response is almost constant after physical activity transition. On the other hand, when the model is more complex, represented in Figure 5.37 with the Exponential PAM, known HR estimation methods fail to present accurate HR frequency. The proposed algorithm for HR estimation still can manage such a complex simulated environment and still produces reliable HR measurements.

5.4 Results and Discussions

The hability to generate synthetic data provides an easy comparison of published algorithms for evaluation of HR estimation methods. By using available sensors, such as PPG and ACC, it's possible to model the environment parameters for a broader range of specifications. In this case, PPG and ACC signals are modeled following the characteristics presented in real

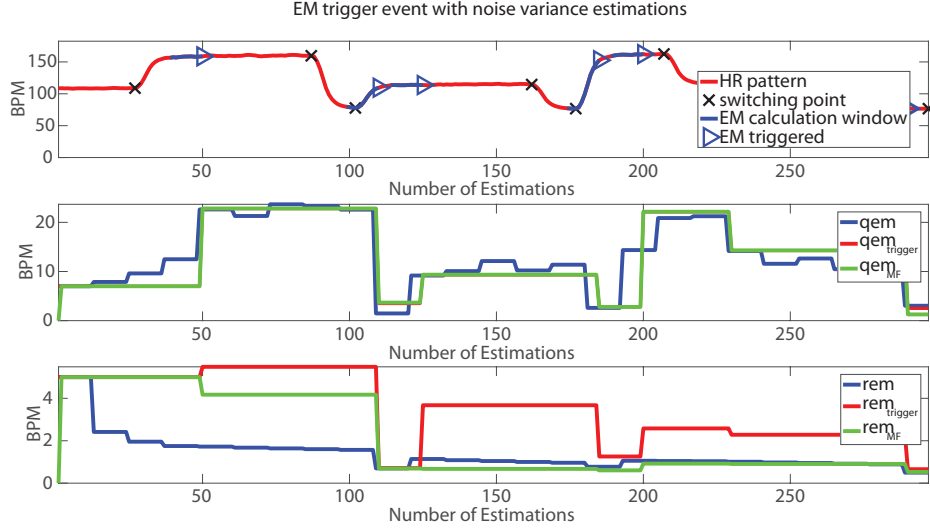


Figure 5.33: EM algorithm estimates the noise variances over the period of estimation. Switching point represents the acknowledgement that a activity changed, and the EM is calculated after the movement related to the activity is decreased.

sensors while in physical activity. This represents a simulation environment capable of producing data independently of equipment and time constraints. On the other hand, the model resembles only three physical patterns, which may not reproduce reliable synthetic signals for more complex physical activities. Model limitations such as minimum and maximum values of parameters as in Table 5.6, might differ under other situations. Another factor is that the trigger to the EM algorithm is assumed know, since it's known when the activity changed. Under a realistic case, an algorithm capable of sensing when the activity is changed should be implemented, allowing the EM algorithm to be triggered.

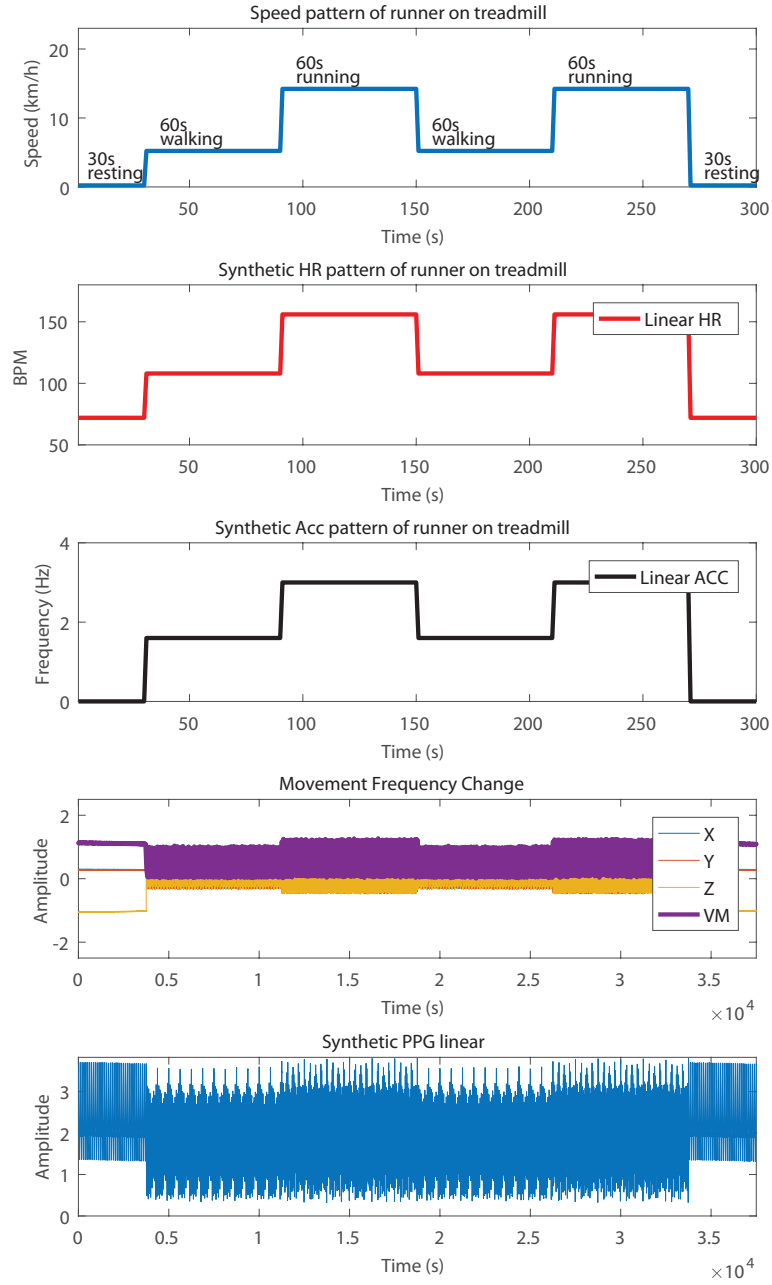


Figure 5.34: Illustration of *PAM* for various running activities level and time durations following the example model in (5.57).

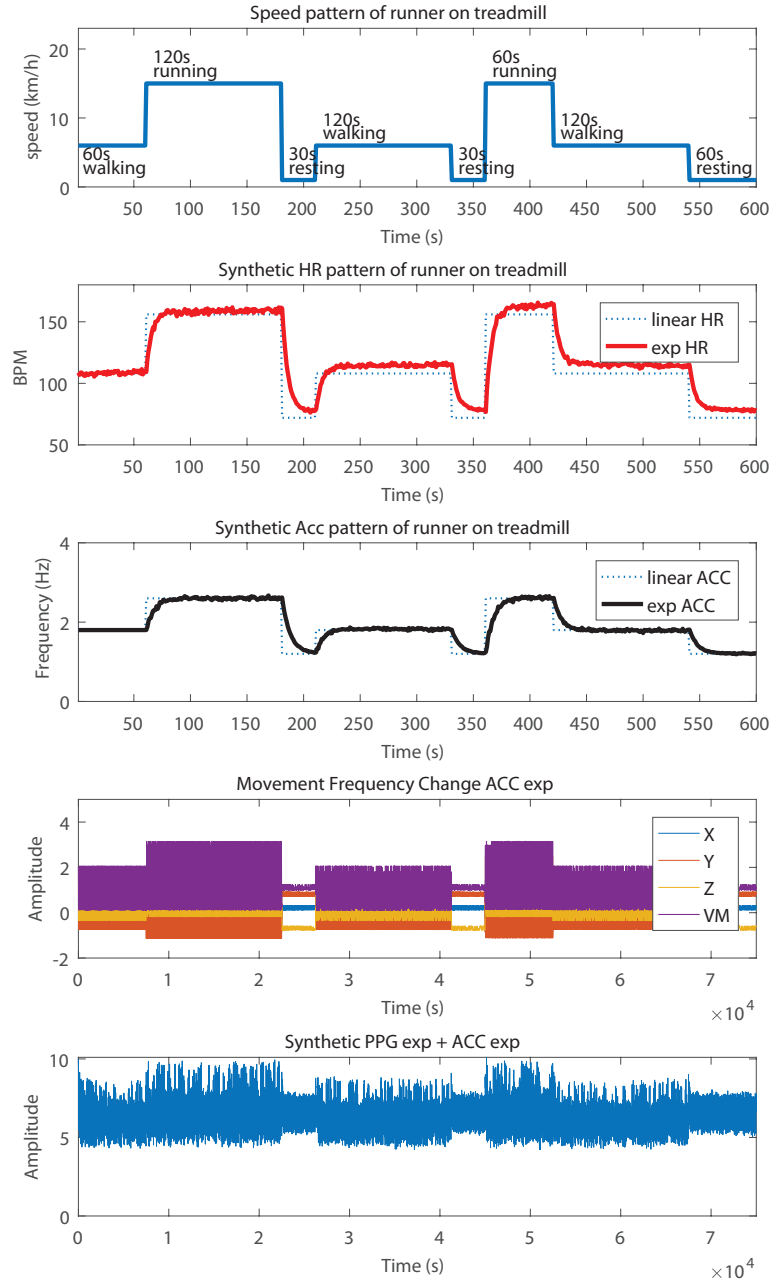


Figure 5.35: Illustration of *PAM* for various running activities level and time durations following the example model in (5.60).

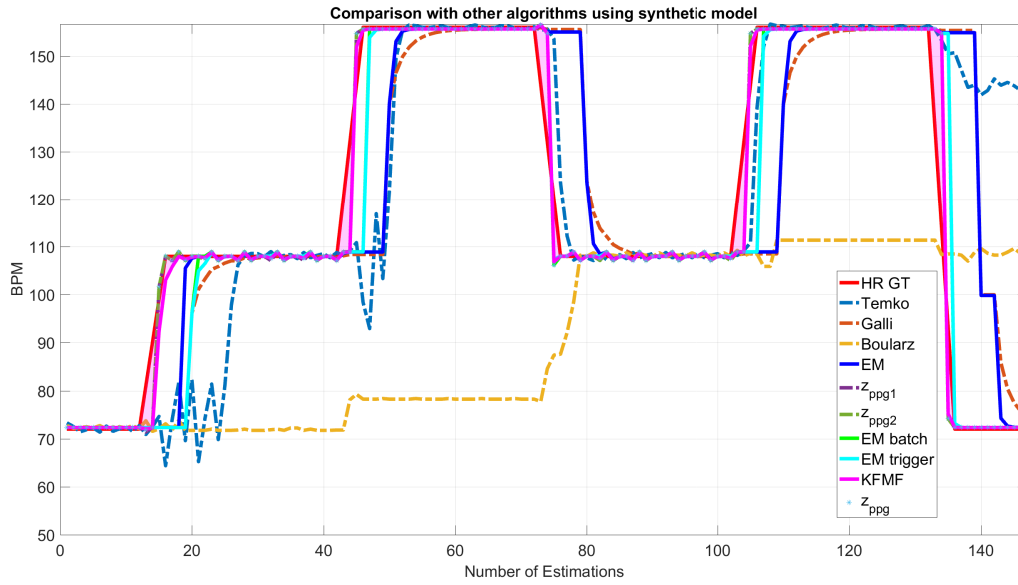


Figure 5.36: Comparison between known algorithms for HR estimation using PPG sensors with a linear PAM model.

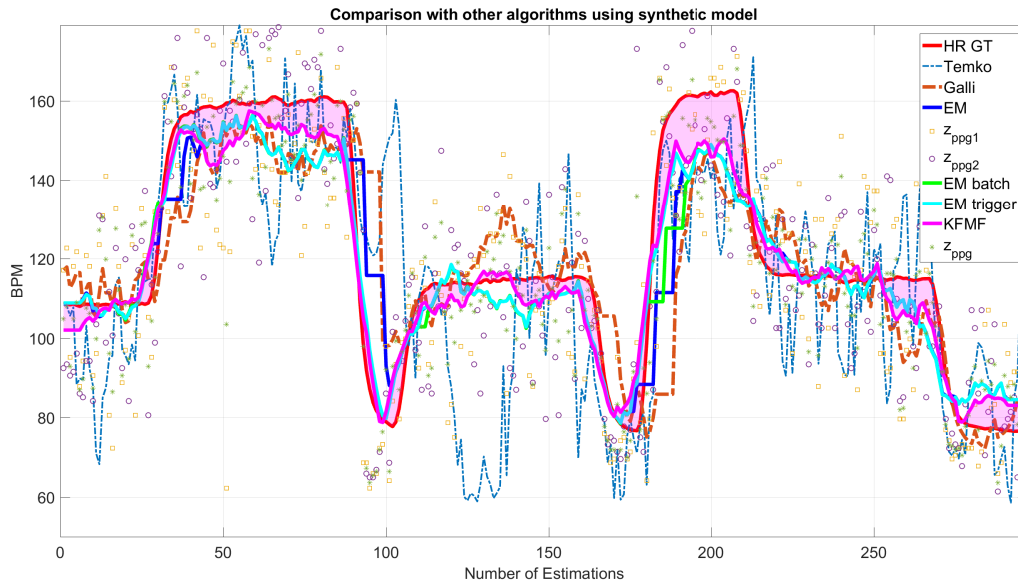


Figure 5.37: Comparison between known algorithms for HR estimation using PPG sensors with a exponential PAM model.

Chapter 6

Hardware Implementation

When designing a wearable system to be used for physiological and biomechanical monitoring, sensor localization, comfort, and portability are important features to be addressed [78]. As explained in chapter 2, determining what type of wearable device and its localization can influence entirely under signal acquisition. Also, comfort and portability display a very important demand, allowing freedom of movement and continuous monitoring. Thus, wearable systems can be often characterized by the integration of a variety of sensors for detecting physiological signs placed on the body without discomfort and continuous feedback of relevant information to the user and/or clinical professionals [20]. Thus, there are three main work areas that need to be implemented in order to design a fully wearable system. First, the system needs to be unobtrusive in order to record physiological and kinesiological data reliably. Secondly, these sensors need to be implemented in a single material, allowing a multisensory integration. Lastly, acquisition and communication structures need to be implemented, facilitating signal acquisition, enhancing mobility and continuous user monitoring [20]. Figure 6.38 depicts an architectural layer for a wearable health system.

Therefore, the hardware implementation in this work follows these mandatory design

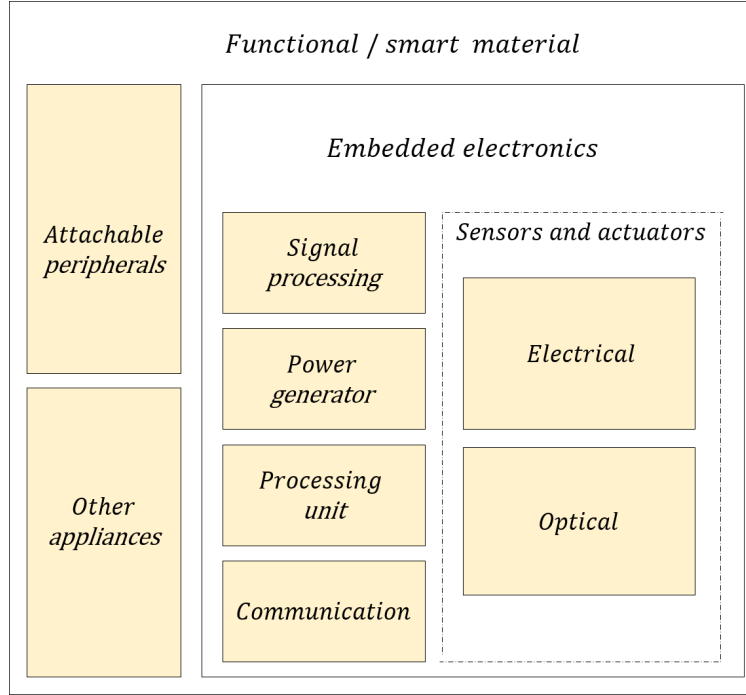


Figure 6.38: Architectural layer of an ideal wearable system.

Source: [20]

parameters. Figure 6.39 shows the proposed hardware implementation accomplished in this work. Detailed functionality will be presented in the next section 6.1.

6.1 Hardware development

The proposed HR monitoring device was analyzed for correct utilization of storage, processing, communication and data transmission. Components were chosen according to the following criteria:

- Data acquisition

For correct HR estimation and comparison with available HR estimation methods, a set of two PPG sensors were used. The MAXREFDES117# is an optical heart rate

module used for wearable devices since it contains a low power design with integrated LEDs and power supply. The board also utilizes the heart rate sensor MAX30102 and accurate level translator, providing an interface between the HR sensor and the controller board. In addition, it includes an ambient light rejection module decreasing the ambient light interference for HR signal acquisition. Communication is done with a I²C protocol, which is generally found in any microcontroller. For modulating the user movement, a tri-axial accelerometer is used. The ADXL335 features a low power consumption module with a complete 3 axis accelerometer with signal conditioned voltage outputs. It measures an acceleration full range of $\pm 3g$ and static acceleration of gravity in tilt-sensing applications.

- Data transmission

The proposed device represents a stage of an ongoing local project. This project has been developed in the Hotel Dieu Grace Healthcare Hospital in Windsor, ON and incorporates a Radio Frequency Identification (RFID) localization and tracking system capable of tracking and monitoring patients using active RFID bracelets. Since the system utilizes 433 MHz RFID tags, data transmission on the device is also set to 433 MHz. For this reason, a low cost, high-performance radio module is used. The RFM69 provides a transceiver/receiver module capable of operating over a wide frequency range including license-free ISM (Industry, Scientific and Medical) bands. In addition, it requires a low current and permits 256 modules to be connected in the same network, more than enough for medical monitoring in closed spaces. As shown in Figure 6.39, communication is performed by two radios. Radio “server” is designated to the module that comprehends the HR monitoring device. The “server” sends data to the “client” radio module, which finally outputs data to the computer using a serial protocol communication.

- Storage and Processing

Since the device comprises a fully functional HR monitoring, that depends on complex algorithm implementation and power management, it also requires a high performance microcontroller and data storage. For this reason, the ARM Cortex M0 Processor ATSAM21G18 was chosen. It demands low supply voltage of 3.3V with enough clock rate for algorithm implementation and enough memory storage.

The final device is composed as a “sandwich” of boards. This configuration allowed connection with all peripherals in a compact monitoring unit. The final hardware implementation is shown in Figure 6.40 and Figure 6.41.

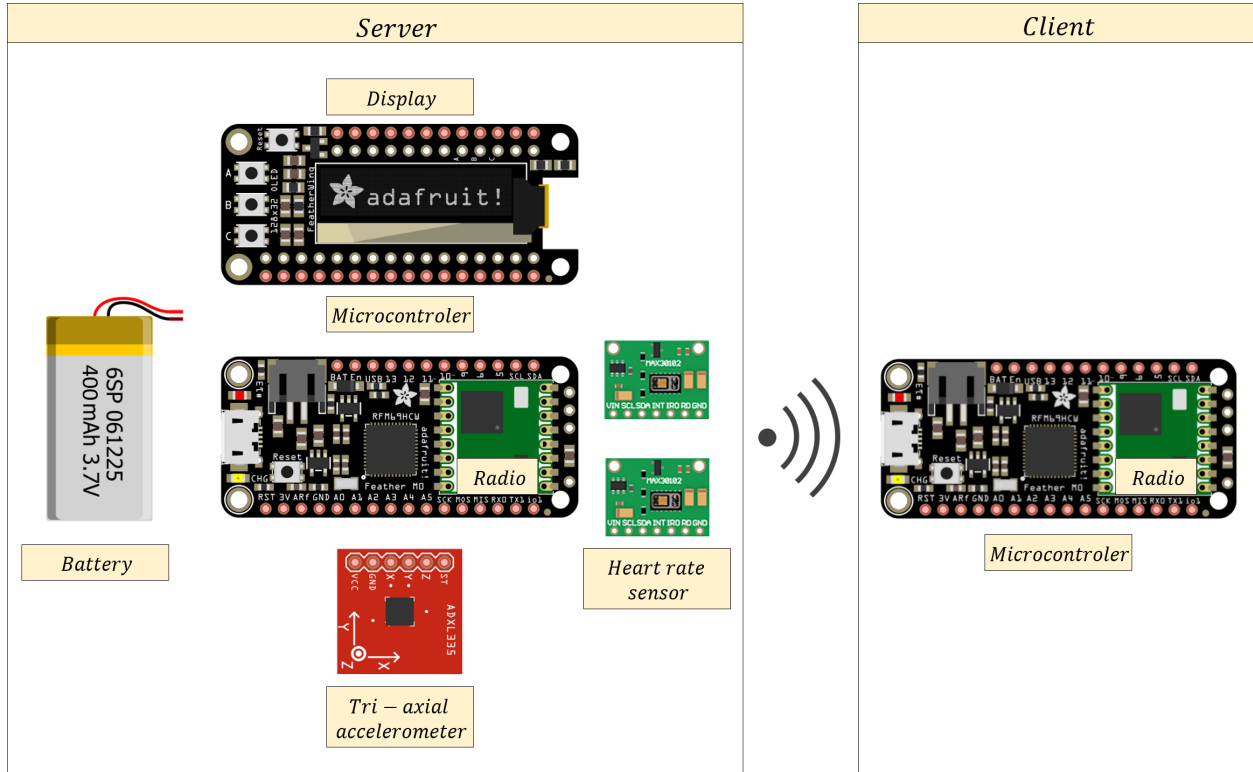


Figure 6.39: Hardware diagram implementation

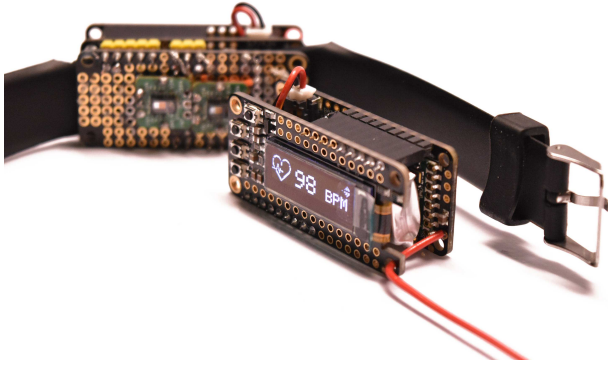


Figure 6.40: Detailed client and server.

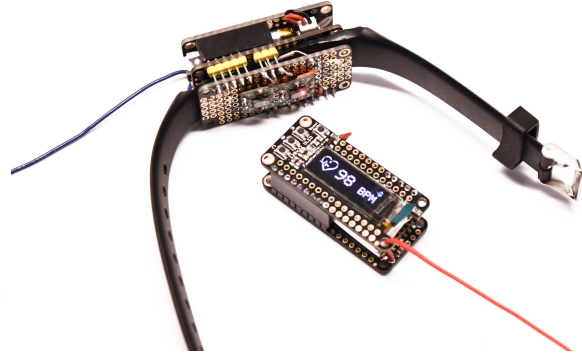


Figure 6.41: Hardware implemented.

6.2 Algorithm Implementation

As it was presented in Figure 4.26, the algorithm implementation is developed by stages. First, out of the bound frequencies are filtered using a 4th order Butterworth with bandwidth of 0.67Hz-3.67Hz. This represents the possible range of HR measurements that an individual can experience while in physical activity and comprehends the boundaries of minimum and maximum HR values an individual can respond as presented in section 3.2.2. For de-noising and MA reference, SVD should be implemented. Even though this method provides a very reliable MA reduction, it represents a complex and high performance algorithm to be embedded into a microprocessor. For matrix calculation and the inverse iteration, assuming only 100 samples, instead of 1000 samples (8-s of data), memory usage would be drastically demanding, preventing memory allocation for forthcoming stages. Thus, after the signal is cleansed by the filter, MA reduction is performed by a faster algorithm which is explained bellow. The FFT is applied in both PPGs and ACC sensors, in order to find the highest frequency peaks on the spectrum. This assumption works fairly well while there is no movement interference. But, as shown in section 2.3, once movement is present, spectrum estimation by highest peak location becomes very difficult, since the correct HR frequency

may overlap, or even disappear. For this reason, the algorithm accounts not only for the fundamental frequency, but also for its second harmonic for both PPG signals. This is done by a novel approach composed of the addition and subtraction of PPG and ACC signals. Since the subtraction represents a way of finding when movement interferes with the spectrum estimation, the addition enhances the spectrum for other specific cases. For the harmonic search, the algorithm works as follows: Assuming that the fundamental frequency is found, the algorithm searches for the highest peak in a selection window corresponding to the estimated second harmonic of the signal. This allows a finer search of the estimated harmonic, which represents a probable HR frequency when compared to the fundamental frequency. If this acknowledgement is accepted, then the estimated HR frequency is passed to the final stage. If this assumption is not accepted a flag is raised and the algorithm compares the available estimated HR frequency and the harmonic, with the available and estimated movement frequencies acquired by the VM from the tri-axial accelerometer. Next, a comparison is performed between these available estimated frequencies. If the estimated HR frequency is retrieved from the comparison and spectrum subtraction(D)/addition(A) of PPG and ACC signals, then the estimated frequency is passed on to the next stage. If not, the estimated HR frequency is compared to the previous three estimates, and if still not remains in a range of $\pm 0.34 \text{ Hz} \equiv 20\text{BPM}$ (assuming that the HR won't change drastically between estimations), then the estimated frequency is assigned to its previous probable value. Figure 6.42 shows the algorithm's selection for the fundamental and second harmonic. Once the highest peak is found, which could possibly correspond to the true HR frequency, a selection window is assigned to each second probable harmonic. In addition, Figure 6.43 represents the case when the highest peak is chosen for HR estimation. As seen, the highest peak of the PPG signals z_{ppg1} and z_{ppg2} are used to estimate the HR, in comparison with the proposed algorithm using the harmonic window selection method (HWSM). Once the movement intensifies, MA

interferes with PPG signals, overlapping both spectrums, complicating reliable HR estimation by the highest peak spectrum selection. This is resolved with the proposed method, which accounts not only for the fundamental frequency, but also its harmonic and other parameter effects under an intensive physical activity.

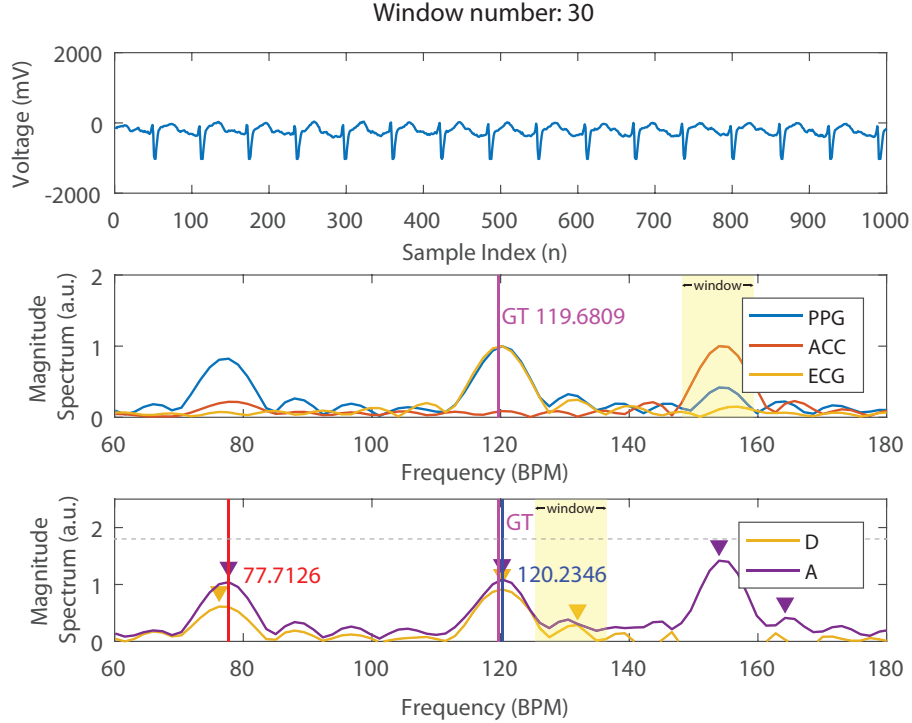


Figure 6.42: Peak selection taking in account the difference (D) and addition (A) of the spectrum estimation. The estimated peak from (D) produces a peak that is very close to the GT value – Dataset #6.

Figure 6.44 shows a PPG signal acquired on the wrist and Figure 6.45 represents the HWSM algorithm implemented in the hardware. As explained, the algorithm looks for the fundamental and the second harmonic of the PPG signal, both represented by the marks on top of the respective peaks.

Since HWSM algorithm depends on several threshold values for frequency attribution, several challenges were encountered during device implementation. PPG values had a higher

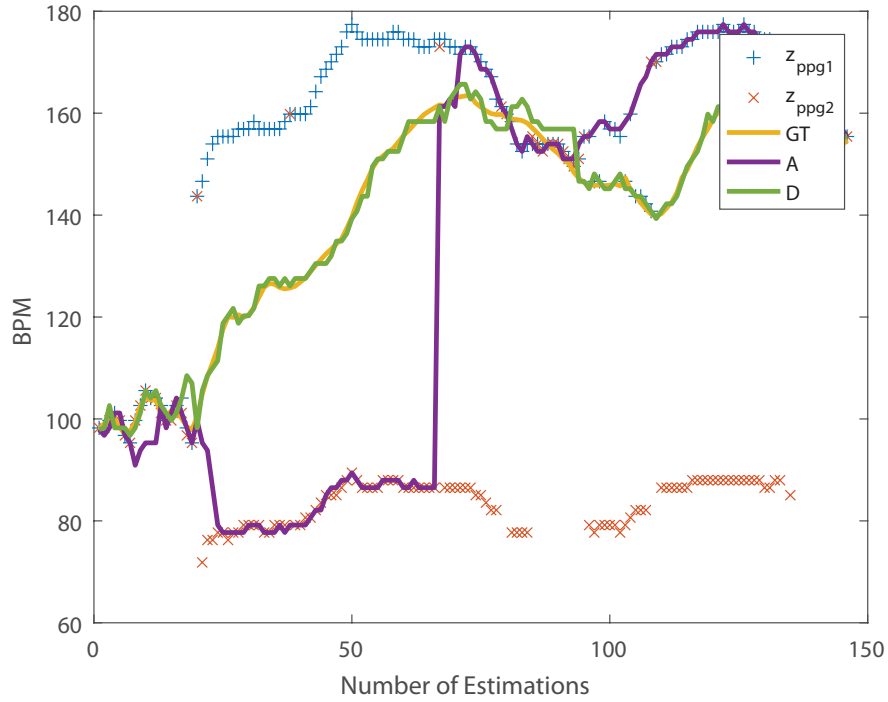


Figure 6.43: Comparison between finding the highest peak in the spectrum and the proposed algorithm. Under intense physical activity, the algorithm still follows the GT HR value – Dataset #12.

magnitude than ACC values, making it challenging their comparison before passing to the FFT. Also, for faster response, the FFT was implemented using integer values instead of float values. This change reduced considerably the frequency resolution, although increased algorithm performance. In addition, even though all developed functions were analyzed and tested in different integrated programming environments, debugging was difficult due to software constraints, such as variable visualization and pointer routines. Such observations will be considered for the final monitoring device.

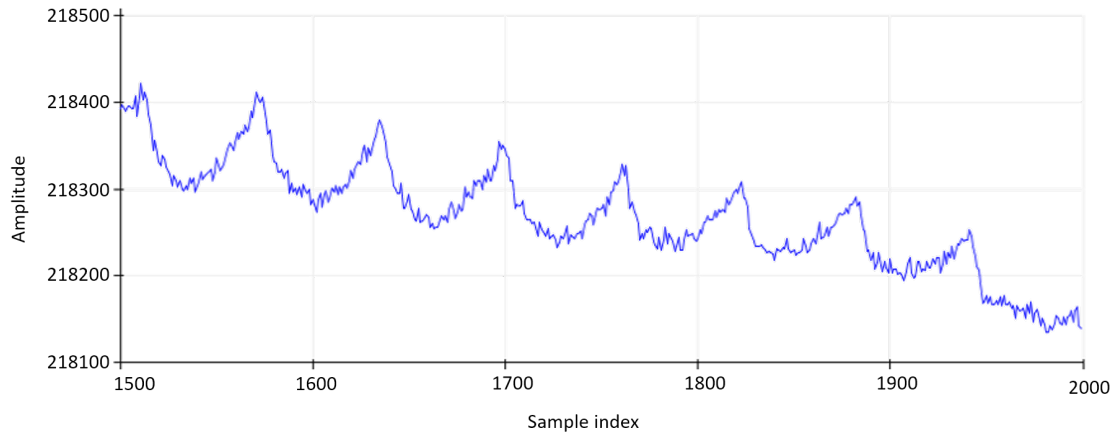


Figure 6.44: PPG signal acquired on the wrist.

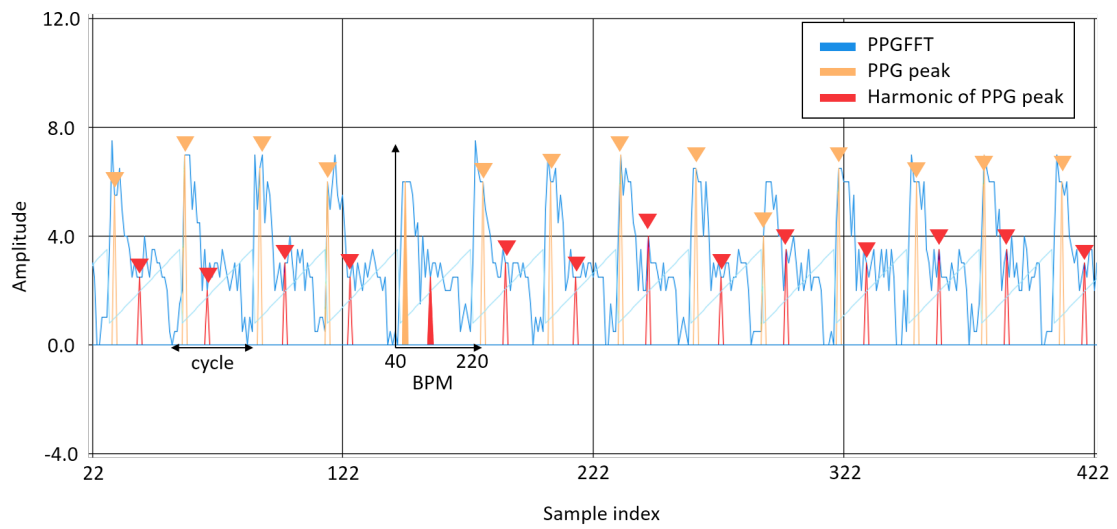


Figure 6.45: HWSM implemented in HW.

Chapter 7

Summary, Conclusions and Future Work

The research described in this thesis has revealed several important pieces of information regarding the reduction of MA using PPG sensors for HR measurement during in physical exercise. In addition to work that could potentially be carried out in the near future, including some progress with the software implementation in the prototype device, key outcomes and necessary observations are summarized next, before the conclusion and results of this work.

7.1 Summary and Conclusions

As it was explained in Chapter 2, PPG sensors are still not widely accepted as the preferred HR measurement system, mainly due to MA and other effects that influence its signal acquisition. Once movement is present, PPG signal may overlap with the frequency of the movement, resulting in signals that are complex to separate and resolve. Moreover, the movement that results from physical exercise, may cause a displacement between the skin and the

sensor, altering the way the sensor responds to blood flow, culminating with an incorrect HR measurement. For this reason, this thesis focused on ways to use PPG sensors, even though corrupted by MA for a correct HR estimation. In Chapter 3 description of the flowchart comprising the main stages for an accurate and reliable HR estimation using PPG sensors is presented. Even though there are primarily three stages, each one is carefully analyzed before implementation. For instance, filtering out the bound frequencies may distort or even disregard a range of important frequencies that might be correlated with the desired signal of the PPG and/or the ACC. Choosing the correct filter is important even for algorithm implementation, as filter coefficients differ depending on the size of the filter, which is an important factor that needs to be embedded into the wearable device. During denoising and MA reference stage, there is a broad range of techniques that can be used to minimize MA effects, but as propounded, there is always a trade-off between accuracy and performance. The proposed algorithm uses SVD as a denoising stage, which contributes to de-referencing the ACC signals from the PPG signals, while retaining the principal characteristic of the PPG signal. This in fact, enhanced the way the raw data is passed on to the next stage, since it provides better results than single spectrum subtraction as used in published algorithms. The drawback is that by using such technique, it becomes very complicated for embedding into a chip due to the complex calculations. Thus, an algorithm was developed using the EM algorithm and KF, providing better parameter estimation independent of the user's physiology. The algorithm implemented shows desirable results in simulation and in available datasets, resulting in better parameter estimation than user tuned parameters. In Chapter 4, it was shown the correct approach to fuse sensors into one single measurement, accounting for each individual signal and correspondent deviations, reducing the error in the filtered state. This process resulted in error reduction when joining both measurement sensors, as opposed to other approaches in published KF algorithms. Now, in Chapter 5 a

tool for generating synthetic PPG and ACC signals was implemented, allowing evaluation of the proposed HR algorithm and comparison with available HR estimation methods. A synthetic exponential model was developed, resembling the characteristics of both PPG and ACC signals during in physical exercise. This tool provides comparison and evaluation of available HR methods regardless of the duration and database used. The final HR estimation method was compared with other “state-of-the-art” methods and provided reliable HR measurements when equated with the ground truth. In Chapter 6 a prototype hardware was implemented, following design definitions for a wearable system; criteria such as data acquisition, transmission and processing were analyzed producing a very robust yet simple prototype. Software implementation is yet not concluded, since several problems arose from data acquisition, storage, and library management. Data is acquired from the sensors, however, once functions are called, due to the complex arithmetic calculations, output rate is decreased, which also could hamper data sent to the client. Moreover, the lack of available sensor libraries diminish accessibility to more complex fetching functionalities for each peripheral. For instance, communication between PPG sensors and the microcontroller is performed by I_2C protocol, which demands that each peripheral maintain a specific address for bus communication. Even though carried-off with other techniques, available PPG sensors do not provide access to change such parameters, complicating expansion to other PPG sensors, without using multiplexers, which would also increase the available area of circuit implementation on the prototype board.

7.1.1 Concluding Remarks

In conclusion, this thesis presented how MA interfere with reliable PPG sensors during physical exercise. Due to this fact, an algorithm was implemented using the EM algorithm and Kalman filter using a measurement fusion approach, allowing a more refine parameter

estimation, and consequently, a more accurate HR measurement. The algorithm was compared with state-of-the-art methods and presented satisfactory results. Moreover, a synthetic PPG and ACC signals generation tool was developed, allowing comparison and evaluation of published algorithms, enabling researchers to compare algorithm results with a simple but accurate model. Finally, a prototype device was designed allowing implementation of the proposed algorithm. Even though it is under development, it already displayed obstacles that need to be addressed, which will be accounted in the final device. It was shown that photoplethysmography sensors have a strong space in the market for wearable devices, but more importantly, it can become the preferred device for heart rate measurement, since it is unobtrusive, lightweight and capable of continuous monitoring, providing an accurate HR measurement, enhancing wellness and comfort to the end user.

7.2 Future work

As the intention of this research was *not* to create a marketable product, but to explore techniques to correctly estimate HR enveloped with motion, the resulting prototype design contains faults that should be addressed for a complete stand alone heart rate monitoring device. Several problems were encountered once the final algorithm was being implemented in the board such as compatibility of functions and accessibility to more complex calculations; changing the microcontroller to a Digital Signal Processing (DSP) processor would enhance performance allowing optimization to meet DSP operation needs. High performance would represent a faster communication between client and server, which would increase data traffic when more clients are added to the system. A final schematic, circuit design and fabrication, would provide a broader insight for the necessary refinements for a future HR monitoring system. In addition, deployment of such system combined with RFID tags would provide

doctors and nurses the ability to monitor patients continuously and unobtrusively, allowing detection and diagnosis of cardiovascular diseases, thereby offering greater insight into a patient's health [7].

Appendix A

Table of Methods

This table represents the comparison of studied methods for HR estimation using PPG sensors. The table depicts a range of methods and it's divided by the different methods for pre-processing, post-processing and algorithm implementation. Database used to evaluate each of the presented methods is also cited. Since there are methods that date differently, a full method comparison between methods is not possible. This is related to the database used, or if the method is accessible for results' replication.

#	Sensor	Year	Denoising	Filter BW (Hz)	Signal Segm.	GT	Noise Model.	Decomposition	Post-processing	Database	Method	Algorithm	location
[79]	PPG	2007	BP filter	0.5 to 3	N/A	N/A	Acc	Adaptive filtering	NLMS	N/A	Classif. of MA	NLMS adaptive filter	finger
[80]	PPG	2012	BP filter	1 to 3	1 sec	ECG	Acc	Threshold of acc	Smoothing filter	N/A	Spectrum estimation	Frequency analysis	wrist
[81]	PPG	2012	HL filter	0.3 to 5	10 sec	ECG	Acc	Adaptive filtering	Select highest peaks	11 subjects	Spectrum estimation	Adaptive filter LMS	finger
[12]	PPG	2015	BP filter	0.5 to 5	8 sec	ECG	Acc	Sparsity signal reconstruction	Regression	12 subjects	Spectrum estimation	Peak detection	wrist
[13]	PPG	2015	BP filter	0.5 to 30	N/A	ECG	N/A	STFT	Threshold step	10 subjects	Spectrum estimation	Peak detection and ranking	wrist
[39]	PPG	2015	BP filter	0.7 to 3.4	8 sec	ECG	Acc	Ensemble Empirical Mode	RLS filter	12 subjects	Time extraction	Adaptive filter	wrist
[14]	PPG	2016	BP filter	0.4 to 5	8 sec	ECG	Acc	SVD	Peak detection and analysis	12 subjects	Spectrum estimation	Adaptive filter	wrist
[57]	PPG	2016	BP filter	0.5 to 3	N/A	N/A	Acc	N/A	N/A	5 subjects	Spectrum estimation	Separation and peak analysis	wrist
[82]	PPG	2016	BP filter	0.4 to 5	N/A	ECG	Acc Gyro	STFT	N/A	8 subjects	Adaptive filtering	N/A	N/A
[15]	PPG	2016	BP filter	0.5 to 10	8 sec	ECG	Acc	Threshold to detect peaks	Spectrum estimation	12 subjects	Spectrum estimation	Peak detection and comparison	wrist
[83]	PPG	2016	BP filter	0.5 to 3	8 sec	ECG	Acc	Resample and periodogram	PPG peaks	23 subjects	Spectrum estimation	PSD calculation	wrist forehead
[61]	PPG	2017	BP filter	0.4 to 4	8 sec	ECG	Acc	Wiener filter	Phase vocoder	23 subjects	Spectrum estimation	Wiener filter and phase vocoder	wrist
[84]	PPG	2017	BP filter	0.4 to 3.5	8 sec	ECG	Acc	Cascaded RLS Filtering	SSA	12 subjects	Spectrum estimation	Adaptive filter	wrist
[16]	PPG	2017	Baseline filter	N/A	8 sec	ECG	N/A	Spectral peak tracking	Cyclic mov. avg	12 subjects	SSA	Peak detection and comparison	wrist
[85]	PPG	2018	BP filter	0.5 to 12	7 sec	ECG	Acc	Feature extraction	FIR LP differ. filter	24h rec	LS-SVM model	Labeling	wrist
[86]	PPG	2018	BP filter	0.5 to 5	N/A	ECG	N/A	N/A	N/A	30 subjects	Threshold function	N/A	wrist
[2]	PPG	2018	BP filter	0.3 to 3.8	8 sec	ECG	Acc	SVD	Kalman filter	23 subjects	Spectrum estimation	Kalman filter	wrist
[87]	PPG	2018	AR	N/A	8 sec	ECG	Acc	Spectral division	Lazy tracker spectral peak	23 subjects	Spectrum estimation	Cumulative spectrum	wrist
[88]	PPG	2018	BP filter	0.4 to 4	8 sec	ECG	Acc Gyro	Spectral normalization	DPDF and FSM	24 subjects	Spectrum estimation	Dominant frequency and FSM	wrist
[17]	PPG	2018	BP filter	0.2 to 5	8 sec	ECG	Acc	Peak comparison	Smoothing filter	12 subjects	Spectrum estimation	Peak detection and comparison	wrist

Bibliography

- [1] Z. Zhang, Z. Pi, and B. Liu, “Troika: A general framework for heart rate monitoring using wrist-type photoplethysmographic signals during intensive physical exercise,” *IEEE Transactions on biomedical engineering*, vol. 62, no. 2, pp. 522–531, 2014.
- [2] A. Galli, C. Narduzzi, and G. Giorgi, “Measuring heart rate during physical exercise by subspace decomposition and kalman smoothing,” *IEEE Transactions on Instrumentation and Measurement*, vol. 67, no. 5, pp. 1102–1110, 2017.
- [3] R. M. Laukkanen and P. K. Virtanen, “Heart rate monitors: state of the art,” *Journal of sports sciences*, vol. 16, no. sup1, pp. 3–7, 1998.
- [4] U. R. Acharya, K. P. Joseph, N. Kannathal, C. M. Lim, and J. S. Suri, “Heart rate variability: a review,” *Medical and biological engineering and computing*, vol. 44, no. 12, pp. 1031–1051, 2006.
- [5] W. H. Organization, “Cardiovascular diseases (cvds), 2017.” <https://www.who.int>. Accessed: 2018-03-11.
- [6] M. AlGhatrif and J. Lindsay, “A brief review: history to understand fundamentals of electrocardiography,” *Journal of community hospital internal medicine perspectives*, p. 14383, 2012.

- [7] D. Castaneda, A. Esparza, M. Ghamari, C. Soltanpur, and H. Nazeran, “A review on wearable photoplethysmography sensors and their potential future applications in health care,” *International journal of biosensors & bioelectronics*, vol. 4, no. 4, p. 195, 2018.
- [8] A. B. Hertzman, “The blood supply of various skin areas as estimated by the photoelectric plethysmograph,” *American Journal of Physiology-Legacy Content*, vol. 124, no. 2, pp. 328–340, 1938.
- [9] T. Tamura and Y. P. Maeda, *Seamless healthcare monitoring*. Springer, 2018.
- [10] P. G. database, “Graph indicating the growth of research on the ppg topic, 2018.” <https://www.pubmed.com>. Accessed: 2018-04-23.
- [11] I. G. database, “Graph indicating the growth of research on the ppg topic, 2019.” <https://ieeexplore.ieee.org/>. Accessed: 2019-09-03.
- [12] A. K. Ahmadi, P. Moradi, M. Malihi, S. Karimi, and M. B. Shamsollahi, “Heart rate monitoring during physical exercise using wrist-type photoplethysmographic (ppg) signals,” in *2015 37th Annual International Conference of the IEEE Engineering in Medicine and Biology Society (EMBC)*, pp. 6166–6169, IEEE, 2015.
- [13] P.-H. Lai and I. Kim, “Lightweight wrist photoplethysmography for heavy exercise: motion robust heart rate monitoring algorithm,” *Healthcare technology letters*, vol. 2, no. 1, pp. 6–11, 2015.
- [14] M. B. Mashhadi, E. Asadi, M. Eskandari, S. Kiani, and F. Marvasti, “Heart rate tracking using wrist-type photoplethysmographic (ppg) signals during physical exercise with simultaneous accelerometry,” *IEEE Signal Processing Letters*, vol. 23, no. 2, pp. 227–231, 2015.

- [15] E. De Giovanni, S. Murali, F. Rincon, and D. Atienza, "Ultra-low power estimation of heart rate under physical activity using a wearable photoplethysmographic system," in *2016 Euromicro Conference on Digital System Design (DSD)*, pp. 553–560, IEEE, 2016.
- [16] D. Zhao, Y. Sun, S. Wan, and F. Wang, "Sfst: A robust framework for heart rate monitoring from photoplethysmography signals during physical activities," *Biomedical Signal Processing and Control*, vol. 33, pp. 316–324, 2017.
- [17] M. A. Motin, C. K. Karmakar, and M. Palaniswami, "Robust heart rate estimation during physical exercise using photoplethysmographic signals," in *2018 40th Annual International Conference of the IEEE Engineering in Medicine and Biology Society (EMBC)*, pp. 494–497, IEEE, 2018.
- [18] H. Han, M.-J. Kim, and J. Kim, "Development of real-time motion artifact reduction algorithm for a wearable photoplethysmography," in *2007 29th Annual international conference of the IEEE engineering in medicine and biology society*, pp. 1538–1541, IEEE, 2007.
- [19] L. Bao and S. S. Intille, "Activity recognition from user-annotated acceleration data," in *International conference on pervasive computing*, pp. 1–17, Springer, 2004.
- [20] R. Kramme, K.-P. Hoffmann, and R. S. Pozos, *Springer handbook of medical technology*. Springer Science & Business Media, 2011.
- [21] C. Glaros and D. I. Fotiadis, "Wearable devices in healthcare," in *Intelligent Paradigms for Healthcare Enterprises*, pp. 237–264, Springer, 2005.
- [22] X.-F. Teng, Y.-T. Zhang, C. C. Poon, and P. Bonato, "Wearable medical systems for p-health," *IEEE reviews in Biomedical engineering*, vol. 1, pp. 62–74, 2008.

- [23] T. W. W., “Speech physiology: Etymology of the word plethysmograph, 1999.” <http://clas.mq.edu.au>. Accessed: 2018-03-11.
- [24] J. W. Chong, D. K. Dao, S. Salehizadeh, D. D. McManus, C. E. Darling, K. H. Chon, and Y. Mendelson, “Photoplethysmograph signal reconstruction based on a novel hybrid motion artifact detection–reduction approach. part i: motion and noise artifact detection,” *Annals of biomedical engineering*, vol. 42, no. 11, pp. 2238–2250, 2014.
- [25] S. Lee, H. Shin, and C. Hahm, “Effective ppg sensor placement for reflected red and green light, and infrared wristband-type photoplethysmography,” in *2016 18th International Conference on Advanced Communication Technology (ICACT)*, pp. 556–558, IEEE, 2016.
- [26] A. Kamal, J. Harness, G. Irving, and A. Mearns, “Skin photoplethysmography—a review,” *Computer methods and programs in biomedicine*, vol. 28, no. 4, pp. 257–269, 1989.
- [27] J. Allen, “Photoplethysmography and its application in clinical physiological measurement,” *Physiological measurement*, vol. 28, no. 3, p. R1, 2007.
- [28] T. Tamura, Y. Maeda, M. Sekine, and M. Yoshida, “Wearable photoplethysmographic sensors—past and present,” *Electronics*, vol. 3, no. 2, pp. 282–302, 2014.
- [29] J. Allen, K. Overbeck, A. F. Nath, A. Murray, and G. Stansby, “A prospective comparison of bilateral photoplethysmography versus the ankle-brachial pressure index for detecting and quantifying lower limb peripheral arterial disease,” *Journal of vascular surgery*, vol. 47, no. 4, pp. 794–802, 2008.

- [30] A. Reisner, P. A. Shaltis, D. McCombie, and H. H. Asada, “Utility of the photoplethysmogram in circulatory monitoring,” *Anesthesiology: The Journal of the American Society of Anesthesiologists*, pp. 950–958, 2008.
- [31] A. A. Kamshilin and N. B. Margaryants, “Origin of photoplethysmographic waveform at green light,” *Physics Procedia*, vol. 86, pp. 72–80, 2017.
- [32] A. R. Kavsaoğlu, K. Polat, and M. Hariharan, “Non-invasive prediction of hemoglobin level using machine learning techniques with the ppg signal’s characteristics features,” *Applied Soft Computing*, vol. 37, pp. 983–991, 2015.
- [33] S.-S. Oak and P. Aroul, “How to design peripheral oxygen saturation (spo2) and optical heart rate monitoring (ohrm) systems using the afe4403,” *Texas Instruments*, 2015.
- [34] J. F. Horton, P. Stergiou, T. S. Fung, and L. Katz, “Comparison of polar m600 optical heart rate and ecg heart rate during exercise.,” *Medicine and science in sports and exercise*, vol. 49, no. 12, pp. 2600–2607, 2017.
- [35] Y. Maeda, M. Sekine, and T. Tamura, “Relationship between measurement site and motion artifacts in wearable reflected photoplethysmography,” *Journal of medical systems*, vol. 35, no. 5, pp. 969–976, 2011.
- [36] L. Kong, Y. Zhao, L. Dong, Y. Jian, X. Jin, B. Li, Y. Feng, M. Liu, X. Liu, and H. Wu, “Non-contact detection of oxygen saturation based on visible light imaging device using ambient light,” *Optics express*, vol. 21, no. 15, pp. 17464–17471, 2013.
- [37] D. K. Spierer, Z. Rosen, L. L. Litman, and K. Fujii, “Validation of photoplethysmography as a method to detect heart rate during rest and exercise,” *Journal of medical engineering & technology*, vol. 39, no. 5, pp. 264–271, 2015.

- [38] S. LeBoeuf, “Optical heart-rate measurement’s top 5 challenges, 2015.” <https://www.edn.com>. Accessed: 2018-03-11.
- [39] E. Khan, F. Al Hossain, S. Z. Uddin, S. K. Alam, and M. K. Hasan, “A robust heart rate monitoring scheme using photoplethysmographic signals corrupted by intense motion artifacts,” *IEEE Transactions on Biomedical engineering*, vol. 63, no. 3, pp. 550–562, 2015.
- [40] A. N. Bashkatov, E. A. Genina, and V. V. Tuchin, “Optical properties of skin, subcutaneous, and muscle tissues: a review,” *Journal of Innovative Optical Health Sciences*, vol. 4, no. 01, pp. 9–38, 2011.
- [41] S. L. Jacques, “Optical properties of biological tissues: a review,” *Physics in Medicine & Biology*, vol. 58, no. 11, p. R37, 2013.
- [42] J. Heikenfeld, A. Jajack, J. Rogers, P. Gutruf, L. Tian, T. Pan, R. Li, M. Khine, J. Kim, and J. Wang, “Wearable sensors: modalities, challenges, and prospects,” *Lab on a Chip*, vol. 18, no. 2, pp. 217–248, 2018.
- [43] R. R. Anderson and J. A. Parrish, “The optics of human skin,” *Journal of investigative dermatology*, vol. 77, no. 1, pp. 13–19, 1981.
- [44] R. Anderson and J. Parrish, “Optical properties of human skin,” in *The science of photomedicine*, pp. 147–194, Springer, 1982.
- [45] V. H. Orellana, “The apple watch series 4 takes heart monitoring to next level, 2018.” <https://www.cnet.com>. Accessed: 2019-01-23.

- [46] Y. Maeda, M. Sekine, and T. Tamura, “Relationship between measurement site and motion artifacts in wearable reflected photoplethysmography,” *Journal of medical systems*, vol. 35, no. 5, pp. 969–976, 2011.
- [47] I. Kim, P.-H. Lai, R. Lobo, and B. J. Gluckman, “Challenges in wearable personal health monitoring systems,” in *2014 36th Annual International Conference of the IEEE Engineering in Medicine and Biology Society*, pp. 5264–5267, IEEE, 2014.
- [48] J. Y. A. Foo and S. J. Wilson, “A computational system to optimise noise rejection in photoplethysmography signals during motion or poor perfusion states,” *Medical and Biological Engineering and Computing*, vol. 44, no. 1-2, pp. 140–145, 2006.
- [49] Y.-L. Zheng, X.-R. Ding, C. C. Y. Poon, B. P. L. Lo, H. Zhang, X.-L. Zhou, G.-Z. Yang, N. Zhao, and Y.-T. Zhang, “Unobtrusive sensing and wearable devices for health informatics,” *IEEE Transactions on Biomedical Engineering*, vol. 61, no. 5, pp. 1538–1554, 2014.
- [50] T. J. Sullivan, S. R. Deiss, and G. Cauwenberghs, “A low-noise, non-contact eeg/ecg sensor,” in *2007 IEEE Biomedical Circuits and Systems Conference*, pp. 154–157, IEEE, 2007.
- [51] V. (Producer), “Building a wearable with accurate biometrics: Lessons learned from 40+ product development cycles. [video webinar,” 2017.
- [52] K. Li and S. Warren, “A wireless reflectance pulse oximeter with digital baseline control for unfiltered photoplethysmograms,” *IEEE transactions on biomedical circuits and systems*, vol. 6, no. 3, pp. 269–278, 2011.
- [53] E. Grisan, G. Cantisani, G. Tarroni, S. K. Yoon, and M. Rossi, “A supervised learning approach for the robust detection of heart beat in plethysmographic data,” in *2015*

37th Annual International Conference of the IEEE Engineering in Medicine and Biology Society (EMBC), pp. 5825–5828, IEEE, 2015.

- [54] V. Jindal, J. Birjandtalab, M. B. Pouyan, and M. Nourani, “An adaptive deep learning approach for ppg-based identification,” in *2016 38th Annual international conference of the IEEE engineering in medicine and biology society (EMBC)*, pp. 6401–6404, IEEE, 2016.
- [55] K. Chan and Y. Zhang, “Adaptive reduction of motion artifact from photoplethysmographic recordings using a variable step-size lms filter,” in *SENSORS, 2002 IEEE*, vol. 2, pp. 1343–1346, IEEE, 2002.
- [56] M. A. Motin, C. K. Karmakar, and M. Palaniswami, “Robust heart rate estimation during physical exercise using photoplethysmographic signals,” in *2018 40th Annual International Conference of the IEEE Engineering in Medicine and Biology Society (EMBC)*, pp. 494–497, IEEE, 2018.
- [57] H. Han, M.-J. Kim, and J. Kim, “Development of real-time motion artifact reduction algorithm for a wearable photoplethysmography,” in *2007 29th Annual international conference of the IEEE engineering in medicine and biology society*, pp. 1538–1541, IEEE, 2007.
- [58] B. S. Kim and S. K. Yoo, “Motion artifact reduction in photoplethysmography using independent component analysis,” *IEEE transactions on biomedical engineering*, vol. 53, no. 3, pp. 566–568, 2006.
- [59] K. A. Reddy and V. J. Kumar, “Motion artifact reduction in photoplethysmographic signals using singular value decomposition,” in *2007 IEEE Instrumentation & Measurement Technology Conference IMTC 2007*, pp. 1–4, IEEE, 2007.

- [60] Y. Fujita, M. Hiromoto, and T. Sato, “Parhelia: Particle filter-based heart rate estimation from photoplethysmographic signals during physical exercise,” *IEEE Transactions on Biomedical Engineering*, vol. 65, no. 1, pp. 189–198, 2017.
- [61] A. Temko, “Accurate heart rate monitoring during physical exercises using ppg,” *IEEE Transactions on Biomedical Engineering*, vol. 64, no. 9, pp. 2016–2024, 2017.
- [62] H. Fukushima, H. Kawanaka, M. S. Bhuiyan, and K. Oguri, “Estimating heart rate using wrist-type photoplethysmography and acceleration sensor while running,” in *2012 Annual International Conference of the IEEE Engineering in Medicine and Biology Society*, pp. 2901–2904, IEEE, 2012.
- [63] Z. Zhang, “Photoplethysmography-based heart rate monitoring in physical activities via joint sparse spectrum reconstruction,” *IEEE transactions on biomedical engineering*, vol. 62, no. 8, pp. 1902–1910, 2015.
- [64] A. Galli, G. Frigo, C. Narduzzi, and G. Giorgi, “Robust estimation and tracking of heart rate by ppg signal analysis,” in *2017 IEEE International Instrumentation and Measurement Technology Conference (I2MTC)*, pp. 1–6, IEEE, 2017.
- [65] G. McLachlan and T. Krishnan, *The EM algorithm and extensions*, vol. 382. John Wiley & Sons, 2007.
- [66] R. H. Shumway and D. S. Stoffer, “Time series regression and exploratory data analysis,” pp. 48–83, Springer, 2006.
- [67] J. A. Bilmes *et al.*, “A gentle tutorial of the em algorithm and its application to parameter estimation for gaussian mixture and hidden markov models,” *International Computer Science Institute*, vol. 4, no. 510, p. 126, 1998.

- [68] T. T. Souza, B. Balasingam, and R. G. Maev, “Autonomous heart rate tracking methodology using kalman filter and the EM algorithm,” in *2019 22nd International Conference on Information Fusion*, 2019.
- [69] R. A. Singer and A. Kanyuck, “Computer control of multiple site track correlation,” *Automatica*, vol. 7, no. 4, pp. 455–463, 1971.
- [70] W. Bath, “Association of multisite radar data in the presence of large navigation and sensor alignment errors,” in *Radar-82*, pp. 169–173, 1982.
- [71] J. Roecker and C. McGillem, “Comparison of two-sensor tracking methods based on state vector fusion and measurement fusion,” *IEEE Transactions on Aerospace and Electronic Systems*, vol. 24, no. 4, pp. 447–449, 1988.
- [72] Y. Bar-Shalom, X. R. Li, and T. Kirubarajan, *Estimation with applications to tracking and navigation: theory algorithms and software*. John Wiley & Sons, 2004.
- [73] Y. Bar-Shalom and L. Campo, “The effect of the common process noise on the two-sensor fused-track covariance,” *IEEE Transactions on Aerospace and Electronic Systems*, no. 6, pp. 803–805, 1986.
- [74] T. M. Cheng, A. V. Savkin, B. G. Celler, S. W. Su, L. Wang, *et al.*, “Nonlinear modeling and control of human heart rate response during exercise with various work load intensities,” *IEEE Transactions on biomedical engineering*, vol. 55, no. 11, pp. 2499–2508, 2008.
- [75] C. R. Cole, E. H. Blackstone, F. J. Pashkow, C. E. Snader, and M. S. Lauer, “Heart-rate recovery immediately after exercise as a predictor of mortality,” *New England journal of medicine*, vol. 341, no. 18, pp. 1351–1357, 1999.

- [76] S. S. Abeysekera, “Photoplethysmographic signal analysis via beat-to-beat periodicity estimation,” in *2016 IEEE Region 10 Conference (TENCON)*, pp. 1733–1736, IEEE, 2016.
- [77] S. Electronics, “A guide to using imu (accelerometer and gyroscope devices) in embedded applications., 2009.” <http://www.starlino.com>. Accessed: 2019-01-17.
- [78] A. Bonfiglio and D. De Rossi, *Wearable monitoring systems*. Springer Science & Business Media, 2010.
- [79] R. W. Wijshoff, M. Mischi, and R. M. Aarts, “Reduction of periodic motion artifacts in photoplethysmography,” *IEEE Transactions on Biomedical Engineering*, vol. 64, no. 1, pp. 196–207, 2016.
- [80] H. Fukushima, H. Kawanaka, M. S. Bhuiyan, and K. Oguri, “Estimating heart rate using wrist-type photoplethysmography and acceleration sensor while running,” in *2012 Annual International Conference of the IEEE Engineering in Medicine and Biology Society*, pp. 2901–2904, IEEE, 2012.
- [81] H. Han and J. Kim, “Artifacts in wearable photoplethysmographs during daily life motions and their reduction with least mean square based active noise cancellation method,” *Computers in biology and medicine*, vol. 42, no. 4, pp. 387–393, 2012.
- [82] A. J. Casson, A. V. Galvez, and D. Jarchi, “Gyroscope vs. accelerometer measurements of motion from wrist ppg during physical exercise,” *ICT Express*, vol. 2, no. 4, pp. 175–179, 2016.
- [83] S. Salehizadeh, D. Dao, J. Bolkhovsky, C. Cho, Y. Mendelson, and K. Chon, “A novel time-varying spectral filtering algorithm for reconstruction of motion artifact corrupted

- heart rate signals during intense physical activities using a wearable photoplethysmogram sensor,” *Sensors*, vol. 16, no. 1, p. 10, 2015.
- [84] M. T. Islam, I. Zabir, S. T. Ahamed, M. T. Yasar, C. Shahnaz, and S. A. Fattah, “A time-frequency domain approach of heart rate estimation from photoplethysmographic (ppg) signal,” *Biomedical Signal Processing and Control*, vol. 36, pp. 146–154, 2017.
- [85] K. Vandecasteele, J. Lázaro, E. Cleeren, K. Claes, W. Van Paesschen, S. Van Huffel, and B. Hunyadi, “Artifact detection of wrist photoplethysmograph signals,” in *BIOSIGNALS*, pp. 182–189, 2018.
- [86] S. Rajala, H. Lindholm, and T. Taipalus, “Comparison of photoplethysmogram measured from wrist and finger and the effect of measurement location on pulse arrival time,” *Physiological measurement*, vol. 39, no. 7, p. 075010, 2018.
- [87] M. B. Mashhadi, M. Farhadi, M. Essalat, and F. Marvasti, “Low complexity heart rate measurement from wearable wrist-type photoplethysmographic sensors robust to motion artifacts,” in *2018 IEEE International Conference on Acoustics, Speech and Signal Processing (ICASSP)*, pp. 921–924, IEEE, 2018.
- [88] H. Lee, H. Chung, and J. Lee, “Motion artifact cancellation in wearable photoplethysmography using gyroscope,” *IEEE Sensors Journal*, vol. 19, no. 3, pp. 1166–1175, 2018.

Vita Auctoris

NAME: Thiago Toledo Souza

PLACE OF BIRTH: Curitiba, Parana, Brazil

YEAR OF BIRTH: 1991

EDUCATION: UTFPR, Curitiba, Brazil
2007-2010, Diploma
Integrated Electronic Technician

UTFPR, Curitiba, Brazil
2011-2013, Bachelor of Science
Control and Automation Engineering

University of Windsor, Windsor, Ontario
2013-2014, Bachelor of Science - Exchange Program
Electrical and Computer Engineering

UTFPR, Curitiba, Brazil
2014-2017, Diploma
Control and Automation Engineering

University of Windsor, Windsor, Ontario
2017-2019, Master of Applied Science
Electrical Engineering